

Annual Research Journal

Electrical Engineering Research Experience for Undergraduates

Vol. VI

August 2008



**National Science Foundation
Grant No. EEC-0755081**

**Principal Investigators:
W. K. Jenkins and Ruyan Guo**

PENNSTATE



**Department of Electrical Engineering
University Park, Pennsylvania**

EEREU Annual Research Journal

John Mitchell (editor)
Ruyan Guo (co-editor)

Volume **VI**

Published in 2008 by
The Department of Electrical Engineering
The Pennsylvania State University
University Park, Pennsylvania, 16802

NSF EE REU Site Program Contact

316 Electrical Engineering East
The Pennsylvania State University
University Park, PA 16802
Telephone (814) 865-0184
Fax (814) 865-7065
E-Mail: eereu@enr.psu.edu
Web Site: <http://www.ee.psu.edu/reu/>



ISBN 0-913260-08-8
978-0-913260-08-1

PREFACE

We are happy to present the 2008 *Annual Research Journal – Electrical Engineering Research Experience for Undergraduates, Vol. VI*. This volume contains highlights of the EE REU program activities for the summer 2008 and thirteen technical papers written by EE REU scholars as primary authors.

Summer 2008 marks our sixth year hosting the National Science Foundation sponsored Research Experience for Undergraduates (REU) Site program, by the Department of Electrical Engineering, Penn State University. Thirteen outstanding young men and women participated in this year's EE REU program at Penn State's University Park Campus. These EE REU scholars, selected from nation-wide applicants, consisted of college freshman, sophomores or juniors with outstanding academic backgrounds and intense interests in exploring research in electrical engineering and related areas.

During the nine-week summer program, EE REU students carried out research projects under the guidance of his or her faculty mentor(s), in laboratories hosted by the Department of Electrical Engineering and Materials Research Institute, Penn State. The students also presented their research experiences and findings at the 2008 Annual *EE REU Symposium*, held at University Park, in July 2008.

Besides research activities, the EE REU program organized an array of group activities including a *Weekly Scientific Seminar Series* that introduces a broad range of research topics to the REU students, a *field trip program* that offers EE REU students opportunities to visit prominent local and regional industrial and research sites, and a *Weekly Workshop on Ethics and Entrepreneurship* through which students were engaged in debate and analysis of issues in ethics and company start-ups in engineering. For more information about Penn State's EE REU program, please visit our website at: < <http://www.ee.psu.edu/reu/> >.

We are confident that readers will find that the series of EE REU journals showcases the achievement of our EE REU students and effective mentorship provided by the faculty and graduate student mentoring teams. We are also hopeful that this publication will not only document original research contributions that are of value for scientific dissemination and publication, but it may also stimulate more college students to consider research careers and to pursue graduate studies in electrical engineering.

W. Kenneth Jenkins and Ruyan Guo
Co-Directors of the NSF EE REU Site Program
Dept. of EE, The Pennsylvania State University

July 2008
University Park, PA

TABLE OF CONTENTS

2008 NSF EEREU Faculty and Staff Members	iii
2008 NSF EEREU Students, Research Topics, and Faculty Mentors	iv
2008 NSF EEREU Summer Program Weekly Scientific Seminar Program	vi
2008 NSF EEREU Summer Program Weekly Workshop on Ethics and Entrepreneurship Development	vii
2008 NSF EEREU Field Trips and Academic/Industrial Sponsors and Tour Hosts	viii
2008 NSF EEREU Annual Symposium Program	x

Research Articles (* indicates REU student author)

TITLE OF THE ARTICLE	<i>Author</i>	Page
SPECTRUM MONITORING ON THE NATIONAL INSTRUMENTS PCI-5640R <i>Philip J. Deets II* and Sven G. Bilén</i>	1
EXPERIMENTAL CHARACTERIZATIONS OF THE IONIC WIND UNDER DC EXCITATION <i>Joseph O’Bruba*, Russell Vela, and Victor P. Pasko</i>	13
IMPLEMENTATION OF AN IONOSONDE USING SOFTWARE- DEFINED RADIO TECHNIQUES <i>Danielle R. Bell*, Ryan L. Seal, and Julio V. Urbina</i>	27
CIRCUIT DESIGN FOR NITTANYSAT SOLAR SENSOR <i>Daniel J. Schuette*, Adam C. Escobar, and Sven G. Bilén</i>	37
INVENTORY AND MODEL BASED METHODS FOR TEXT TO SPEECH SYNTHESIS <i>Alexander Harrison*, Kenneth Jenkins, and Robert Nickel</i>	43
SOLVING THE MYSTERY OF LONG DURATION METEOR TRAILS <i>Kimberly L. Ray*, Akshay Malhotra, and John D. Mathews</i>	51

MODELING OF REALISTIC THUNDER CLOUD CHARGE STRUCTURE AND APPLICATION TO SIMULATION OF LIGHTNING DISCHARGES <i>Samuel T. Poulos*, Jeremy A. Rioussset, and Victor P. Pasko</i>	61
DEVELOPMENT OF DATA PROCESSING VTS IN LABVIEW FOR REAL- TIME QUARTZ CRYSTAL RESONANCE FREQUENCY AND QUALITY FACTOR <i>Nona Ebrahimi*, Ping Kao, Ashish Patwardhan, and Srinivas Tadigadapa</i>	79
SPATIAL AND TEMPORAL SHAPING OF FEMTOSECOND LASER PULSES <i>Jeremy Dwyer*, Haifeng Li, and Zhiwen Liu</i>	87
INVESTIGATION OF DYNAMIC CHARACTERISTICS OF PIEZOELECTRIC T-BEAM ACTUATORS <i>Siddharth Sonti*, Andrew Hirsh, and Srinivas Tadigadapa</i>	101
MEASUREMENT AND SIMULATION OF INTER DIGITAL CAPACITOR STRUCTURES WITH HIGH-PERMITTIVITY THIN FILMS <i>Clinton P. Scarborough*, Steve Perini, and Michael Lanagan</i>	111
EVALUATION OF CIRCUIT-BLOCKS FOR A ROBINSON MARGINAL OSCILLATOR <i>Michael Murphy* and Jeffrey L. Schiano</i>	117
FINITE ELEMENT METHOD SIMULATION OF VOLTAGE DRIVEN SOLID ROTOR SYNCHRONOUS MACHINES WITH LC FILTERS <i>Michael W. Lengel* and Heath Hofmann</i>	133
<i>Author Index</i>		141

2008 NSF EE REU FACULTY & STAFF MEMBERS

Faculty Mentors:

Prof. Sven Bilén
Prof. Heath Hofmann
Prof. Ken Jenkins, Co-Director
Prof. I. C. Khoo
Prof. Mike Lanagan
Prof. Zhiwen Liu
Prof. John Mathews
Prof. Robert Nickel
Prof. Victor Pasko
Prof. Jeff Schiano
Prof. Srinivas Tadigadapa
Prof. Julio Urbina

Ms. Amy Freeman, Adviser, Engineering Diversity
Prof. Ruyan Guo, Co-Director
Mrs. MaryAnn Henderson, Administration
Prof. Elizabeth Kisenwether, Entrepreneurship Chair
Prof. Andy Lau, Ethics Workshop Chair
Prof. Jack Mitchell, Seminar Chair
Mr. Donald Natale, III, Assistant Director
Prof. David Salvia, Activities and Web Chair

**2008 NSF EE REU SCHOLARS, RESEARCH TOPICS, AND
FACULTY MENTORS**

2008 REU Scholars	Research Topics	Faculty Mentors
Miss Danielle Bell Computer Science Grove City College	Implementing a Software-defined Radio Based Ionosonde Using Universal Software Radio Peripherals	Prof. Julio Urbina 315 EE East
Mr. Philip Deets Computer Science and Mathematics Grove City College	Spectrum Monitoring with a Software Defined Radio	Prof. Sven Bilén 313 EE East and Prof. Jack Mitchell 330 EE East
Mr. Jeremy Dwyer Electrical Engineering Grove City College	Simultaneous Time and Spatial Shaping of Femtosecond Laser Pulses Shaping	Prof. I. C. Khoo 217 EE East and Prof. Zhiwen Liu 314 EE East
Miss Nona Ebrahimi Engineering University of Michigan - Ann Arbor	Development of Data Processing VI's in LabView for Real-Time Quartz Crystal Resonance frequency and Phase Monitoring	Prof. Srinivas Tadigadapa 228B EE West
Mr. Alexander Harrison Electrical Engineering Lehigh University	Inventory & Model Based Methods for Text to Speech Synthesis	Prof. Ken Jenkins 129 EE East and Prof. Robert Nickel 6-3 EE West
Mr. Michael Lengel Electrical Engineering Bucknell University	Finite Element Simulation of Voltage Driven Solid Rotor Synchronous Machines with LC Filters	Prof. Heath Hofmann 209K EE West

**2008 NSF EE REU SCHOLARS, RESEARCH TOPICS, AND
FACULTY MENTORS (CONT.)**

2008 REU Scholars	Research Topics	Faculty Mentors
Mr. Michael Murphy Engineering Physics West Virginia Wesleyan College	The Evaluatoin of Circuit-Blocks for a Robinson Marginal Osciallator	Prof. Jeff Schiano 227D EE West
Mr. Joseph O'Bruba Bioengineering Penn State University	Investigation of A Uniform Wind Velocity Generation Using Cold Plasma	Prof. Victor Pasko 211B EE East
Mr. Samuel Poulos Biomedical Engineering The University of Texas at Austin	Modeling of realistic thundercloud charge structure based on Lightning Mapping Array observations and application to three-dimensional stochastic simulation of lightning discharge	Prof. Victor Pasko 211B EE East
Miss Kimberly Ray Physics Texas Lutheran University	Solving the Mystery of Long Duration Echoes	Prof. John Mathews 323A EE East
Mr. Clinton Scarborough Electrical Engineering Grove City College	Measurement and Simulation of Interdigital Capacitor Structures with High-Permittivity Thin Films	Prof. Mike Lanagan 278 Materials Research Lab
Mr. Daniel Schuette Electrical Engineering and Physics Penn State University	Circuit Design for NittanySat Solar Power System	Prof. Sven Bilén 313 EE East and Prof. Jack Mitchell 330 EE East

NSF EE REU 2008 Summer Program Research Seminar Series

Room 101 E E East, 9:40 – 10:30 AM, Tuesdays
(The seminars are open to the public)

Department of Electrical Engineering
Pennsylvania State University, University Park, PA 16802

<i>Date</i>	<i>Topic</i>	<i>Speaker</i>
<i>June 3, 2008</i>	Energy Harvesting	Heath Hofmann
<i>June 10, 2008</i>	The Joy of Quadrupole Resonance	Jeff Schiano
<i>June 17, 2008</i>	Ushering in the “Green” Transistor	Suman Datta
<i>June 24, 2008</i>	What’s Next? Graduate School, of Course!	David Salvia
<i>July 1, 2008</i>	Software Defined Radio Applications	Sven Bilén
<i>July 8, 2008</i>	Integrating Nanowire-based Sensors with CMOS Electronics Using Directed Self Assembly	Theresa Mayer
<i>July 15, 2008</i>	Lightning-related Transient Luminous Events in the Middle Atmosphere	Victor Pasko
<i>July 24, 2008</i> <i>(Thursday)</i>	2008 NSF EEREU Symposium	REU Students

NSF EE REU 2008 Summer Program Ethics & Entrepreneurship Workshop

Room 101 E E East, 10:50 – 11:50 AM, Tuesdays
(The seminars are open to the public.)

Department of Electrical Engineering
Pennsylvania State University, University Park, PA 16802

<i>Date</i>	<i>Topic</i>	<i>Speaker</i>
<i>May 27, 2008</i>	Welcome Meeting and Kick-off Activities	Profs. Andy Lau & Liz Kisenwether
<i>June 3, 2008</i>	Types of Moral Problems and Academic Integrity	Prof. Andy Lau
<i>June 10, 2008</i>	Codes of Ethics and Responsible Conduct of Research	Prof. Andy Lau
<i>June 17, 2008</i>	Global Environmental Issues and Moral Imagination	Prof. Andy Lau
<i>June 24, 2008</i>	Intellectual Property and Smart Materials	Prof. Kenji Uchino
<i>July 1, 2008</i>	Ethics Situations in Research	Prof. Andy Lau
<i>July 8, 2008</i>	Technology Entrepreneurship Basics	Prof. Liz Kisenwether
<i>July 15, 2008</i>	Realities of a Student-based Technology Start-up: Buzby Networks	Prof. Liz Kisenwether & Buzby Founders
<i>July 24, 2008 (Thursday)</i>	2008 NSF EE REU Research Symposium	REU Students

NSF EE REU 2008 Summer Program Field Trip Itinerary

All field trips are from 1:30 – 4:00 PM on Tuesdays except as noted.

Department of Electrical Engineering
Pennsylvania State University, University Park, PA 16802

<i>Date</i>	<i>Field Trip</i>	<i>Contact</i>
<i>June 3, 2008</i>	EE Lab Tour	Don Natale
<i>June 10, 2008</i>	NanoFab Facility and MicroFab Characterization Lab	Leeanna McCool
<i>June 17, 2008</i>	Breazeale Nuclear Reactor	Candace Davison
<i>June 24, 2008</i>	State of the Art, Inc.	Amit Das
<i>July 2, 2008</i> <i>(Wednesday,</i> <i>All-day event)</i>	Pittsburgh Day Trip: TTC, Inc. Seagate, Inc.	Liz Kisenwether
<i>July 8, 2008</i>	Applied Research Laboratory	Janet Jonson
<i>July 15, 2008</i>	Videon Central	Todd Erdley

2008 NSF EE REU Field Trip Program Academic/Industrial Sponsors and Tour Hosts

Department of Electrical Engineering
Penn State University, University Park, Pennsylvania

Materials Research Institute
Penn State University, University Park, Pennsylvania

Applied Research Laboratory
Penn State University, University Park, Pennsylvania

Breazeale Nuclear Reactor
Penn State University, University Park, Pennsylvania

Nanofabrication National Facility
Penn State University, University Park, Pennsylvania

State of The Art, Inc.
State College, Pennsylvania

Videon Central, Inc.
State College, Pennsylvania

Compunetix, Inc.
Monroeville, Pennsylvania

The Technology Collaborative
Pittsburgh, Pennsylvania

Seagate Technology
Pittsburgh, Pennsylvania

2008 NSF EE REU SYMPOSIUM

9:25 AM to 3:45 PM, Thursday, July 24, 2008
 Room 101 Electrical Engineering East Building
 Pennsylvania State University, University Park, PA 16802

Time	Sessions and Topics	Chairs and Speakers
8:45 - 9:25 am	Symposium Registration (Refreshments Provided)	(MaryAnn Henderson Donald Natale)
9:25 – 9:30 am	Welcome	Ken Jenkins
9:30 – 10:30 am	Session I	Session Chairs: Bilén/Urbina/ Mitchell/Pasko
9:30– 9:45	SPECTRUM MONITORING ON THE NATIONAL INSTRUMENTS PCI-5640R	Philip Deets
9:45 – 10:00	EXPERIMENTAL CHARACTERIZATIONS OF THE IONIC WIND UNDER DC EXCITATION	Joseph O'Bruba
10:00 – 10:15	IMPLEMENTATION OF AN IONOSONDE USING SOFTWARE-DEFINED RADIO TECHNIQUES	Danielle Bell
10:15 – 10:30	CIRCUIT DESIGN FOR NITTANYSAT SOLAR SENSOR	Daniel Schuette
10:30 – 10:45	Coffee Break	
10:45 – 11:45	Session II	Session Chairs: Hofmann//Mathews /Nickel/Pasko
10:45 – 11:00	INVENTORY & MODEL BASED METHODS FOR TEXT TO SPEECH SYNTHESIS	Alexander Harrison
11:00 – 11:15	SOLVING THE MYSTERY OF LONG DURATION METEOR TRAILS	Kimberly Ray
11:15 – 11:30	MODELING OF REALISTIC THUNDER CLOUD CHARGE STRUCTURE AND APPLICATION TO SIMULATION OF LIGHTNING DISCHARGES	Samuel Poulos
11:30 – 11:45	(Group Photo at 11:30 – All invited. Please plan to be available.)	(Donald Natale)
12:00 – 1:30	Luncheon (Dining Room, Nittany Lion Inn)	

2008 NSF EE REU SYMPOSIUM (cont.)

9:25 AM to 3:45 PM, Thursday, July 24, 2008
 Room 101 Electrical Engineering East Building
 Pennsylvania State University, University Park, PA 16802

Time	Sessions and Topics	Chairs and Speakers
1:45 – 2:30 pm	Session III	Session Chairs: Tadigadapa/Liu/ Khoo/
1:45 – 2:00	INSTRUMENTATION AND DATA ACQUISITION DEVELOPMENT FOR FAST MULTIPLEXED THERMAL MEASUREMENTS	Nona Ebrahimi
2:00 – 2:15	SPATIAL AND TEMPORAL SHAPING OF FEMTOSECOND LASER PULSES	Jeremy Dwyer
2:15 – 2:30	INVESTIGATION OF STRUCTURAL DYNAMICS OF MESOSCALE PIEZOELECTRIC T-BEAM ACTUATORS	Siddharth Sonti
2:30 – 2:45m		Coffee Break
2:45 – 3:45 pm	Session IV	Session Chairs: Lanagan/ /Schiano/Hofmann
2:45 – 3:00	MEASUREMENT AND SIMULATION OF INTER DIGITAL CAPACITOR STRUCTURES WITH HIGH-PERMITTIVITY THIN FILMS	Clinton Scarborough
3:00 – 3:15	EVALUATION OF CIRCUIT-BLOCKS FOR A ROBINSON MARGINAL OSCILLATOR	Michael Murphy
3:15 – 3:30	FINITE ELEMENT SIMULATION OF VOLTAGE DRIVEN SOLID ROTOR SYNCHRONOUS MACHINES WITH LC FILTERS	Michael Lengel
3:30 – 3:45	CONGRATULATIONS AND CONCLUDING REMARKS	Jenkins/Guo
3:45 pm Adjournment		
Picnic at Sunset Park, 5:00 pm – sunset, ALL ARE INVITED		
Resource:	Donald Natale and MaryAnn Henderson	
Special Notes:	Laser pointer, desktop PC and LCD PC projector are provided. Speakers please upload presentation files to EEREU group web in Angel by July 23 Wed. It is strongly recommended that speakers test-run presentation files for audio, video, or special applications prior to Thursday presentation. Each presentation is 15 min, chair introduction, questions and answers included.	

SPECTRUM MONITORING ON THE NATIONAL INSTRUMENTS PCI-5640R

Philip J. Deets II* and Sven G. Bilén[#]

Department of Electrical Engineering
The Pennsylvania State University, University Park, PA 16802

*Undergraduate student of
Computer Science
Grove City College
Grove City, PA 16127

ABSTRACT

A design and partial implementation of a software-defined spectrum monitor will be presented. This software uses the National Instruments PCI-5640R transceiver to monitor the radio frequency spectrum. This radio system is developed with LabVIEW. The transceiver has an FPGA which does all the real-time processing. The host computer handles the presentation of the data, the interaction with the user, and any other logic that is not suitable for, or does not fit on, the FPGA. The user can then detect which sections of the spectrum are being occupied by signals. The end result is a plan for a spectrum monitoring system which can later be completely implemented to be applied to research in emerging technologies such as cognitive radio.

INTRODUCTION

Spectrum monitoring is becoming a very important component of future radio systems. The Federal Communications Commission is exploring rules that would allow unlicensed devices to transmit in the unused portions of the broadcast television spectrum.¹ To be able to take advantage of this, radio systems are needed that can find the unused portions of the spectrum. Spectrum monitoring is needed to sense the “whitespaces” where transmission will not interfere with the primary user of that spectrum slice.

[#] Faculty Mentor

Cognitive radio is a paradigm which, when sufficiently developed, will enable efficient use of the radio spectrum. Cognitive radio is enabled by software-defined radio, a paradigm in which many of the hardware components of a traditional radio are being replaced with software. As an example, Kognitiv Networking Over White Spaces (KNOWS) is a prototype cognitive-radio system being developed by Microsoft Research.² KNOWS utilizes a spectrum scanner to detect unused portions of the TV spectrum that can be used for its radio transmissions. Spectrum monitoring is a key component necessary for the realization of cognitive radios.

The software presented here is a design for a spectrum monitor on the National Instruments (NI) PCI-5640R transceiver board. The purpose of developing the software was to determine the usefulness of the transceiver for this type of application and to develop a software base for further development with this transceiver. The software could be extended to perform further analysis of the signals it detects to attempt to gather information about each signal.

HARDWARE OVERVIEW

The NI PCI-5640R board can be programmed in two different ways. The first way uses the instrument driver. In this mode, the field-programmable gate array (FPGA) cannot be customized and all custom processing must be placed on the central processing unit (CPU). The other mode allows custom code to be written for the FPGA, but fewer preprogrammed blocks are available, which means that these must be implanted by the programmer. The FPGA model has less documentation, but it is more powerful. This software uses the FPGA programming model to get maximum performance and flexibility from the board.

The software is implemented in LabVIEW 8.5. It is divided into a component that runs on the FPGA and a component that runs on the CPU. The LabVIEW FPGA Module and the Fixed-Point Math Library are used to develop the software for the FPGA.

The NI PCI-5640R board has many components that process signals before the samples are transferred to the FPGA. The RF input is passed first through an 80-MHz low pass filter (LPF). After this, the signal is digitized by a 14-bit, 100-MHz analog-to-digital convertor (ADC). After the sampling, the data passes through a numerically controlled oscillator (NCO), which can mix any part of the sampled spectrum down to baseband. There is also a digital down converter (DDC) that can decimate the signal before the samples are passed to the FPGA.

NI provides several virtual instruments (VIs) to interact with the hardware components from the CPU side. Among other things, these VIs can configure the clock rate on the ADC, the frequency of the NCO, and the decimation factor for the DDC. The DDC VI requires that the decimation factor be at least four, thus the maximum rate of received samples is 25 million samples per second.

THE LABVIEW FPGA PROGRAMMING MODEL

LabVIEW's FPGA module enables writing code for the FPGA with the same graphical programming language that is used for code that runs on the CPU. However, there are many different considerations that must be taken into account for the FPGA.

To facilitate real-time processing, the FPGA module provides what is called a single-cycle timed loop (SCTL), as illustrated in Figure 1. An SCTL is a loop similar to a while loop except that each iteration of the loop runs in one clock cycle. SCTLs are necessary on the FPGA for deterministic timing of operations. For example, to receive samples from the ADC, the input code must be placed within a SCTL timed to an ADC clock. This way there will always be one sample available for each iteration of the loop.

It is useful to put all FPGA code within SCTLs. This allows you to accurately predict the amount of time that it will take any operation to complete. However, the code that needs to be placed into a SCTL often needs more time to run than a clock cycle will provide. In this case, pipelining must be used.

Pipelining is accomplished with feedback nodes. Feedback nodes look like an arrow that is placed on a wire within the SCTL. They are essentially just registers that get read and written once per clock cycle. At the beginning of each clock cycle, each active feedback node releases the value it is storing to the wire in the direction the arrow is pointing. It replaces the stored value with the value that is on the wire at the base of the arrow. Only the computations between the feedback nodes must occur once per clock cycle.

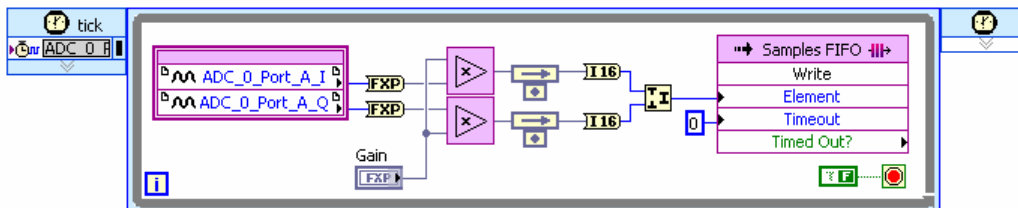


Figure 1. An example of an SCTL with two feedback nodes and a FIFO

Communication between SCTLs occurs through first-in first-out (FIFO) queues. When FIFOs are used in SCTLs, there can only be one block to write to the FIFO and one block to read from the FIFO due to timing restrictions. FIFOs are also used for one-way communication from the FPGA to the host or vice versa. A maximum of four FIFOs may communicate between the FPGA and the host.

It is possible to use blocks of memory in the FPGA. These blocks must have a fixed size. Like FIFOs, when a block of memory is used in an SCTL, it can only have one block to read from memory and one block to write to memory. Multiple blocks require arbitration, which is not supported within an SCTL. Also,

only one value may be read from the memory and one value may be written to the memory per clock cycle. A memory read or write takes an entire clock cycle; so feedback nodes must be used before and after a read or write block.

Arrays and clusters are supposed to work on the FPGA, but they can cause problems with the compiler and thus should be avoided. If arrays are used, they must be fixed size.

Floating point arithmetic is not natively supported on the FPGA; however, fixed point is supported. Fixed point numbers can be set to be either signed or unsigned, and they can have any size from 1 to 64 bits with the radix point placed at any specified location. The LabVIEW Fixed-Point Math Library provides some blocks that make fixed point programming easier for the FPGA. It can either automatically handle the sizing of the result so that no overflow will occur or allow the programmer to specify the details of the fixed-point output.

Since SCTLs run every clock cycle, it is important to make sure the FPGA code works when there is no data available for computation. State machines may be useful for this. These can be implemented with a combination of enumerations and case structures. This technique was used for the fast Fourier transform (FFT) algorithm presented later in this paper.

NI PCI-5640R FPGA SPECIFICS

There are six clocks available to time loops on the FPGA on the PCI-5640R. The configuration clock runs at 20 MHz and is not configurable. There is a separate clock for each of the two ADCs and a separate clock for each of the two DACs. The final clock is called the real-time system integration (RTSI) reference clock which is used for timing on the computer's bus. The RTSI clock is often used for SCTLs that do not need to be timed to an ADC or a DAC. It can be set to 200 MHz divided by any power of two from one to sixteen.

In-phase and quadrature (IQ) samples can be obtained from the ADCs through FPGA input-output (I/O) nodes. They can only be read in a SCTL, which is clocked by the clock for the ADC that is being read.

The compiler for the FPGA has two stages. LabVIEW performs the first stage, which translates the LabVIEW code to an intermediate representation that the next stage understands. The next stage is the Xilinx compile, which converts the intermediate representation to a bitstream that can be downloaded to the FPGA. The whole compilation cycle takes from 40 to 100 minutes (on a 2.4 GHz P4 with 1 GB of RAM.) depending on the complexity of the FPGA code.

Unfortunately, the compile seems to fail often. Often the compile will work just by trying again with the same code. The compiles seem to fail often when arrays and clusters are used. An NI employee advised me to avoid arrays and clusters on the FPGA because of the compiler's weaknesses. Often memory blocks or unit delay nodes with several parallel wires can be used to replace an array. Also, having useless wires and unwired parts may cause errors during the compile.

When a compile finishes successfully, a report is shown that gives several statistics about the FPGA. The device utilization gives an idea of how much of the logic on the FPGA is consumed by your code. After this, there are timing reports about the clocks that are used. A value is given for the requested clock rate and a value for the theoretical clock rate. The theoretical clock rate is the rate at which the SCTLs timed to this clock could run without problems. If the requested rate and the theoretical rate are very close, it may be wise to add more pipelining to give a little more room for margin of error.

SOFTWARE DESIGN

This section presents a design for a spectrum monitoring system, shown in Figure 2. The system inputs a frequency range and a minimum frequency resolution and outputs a graphical display of the spectrum with a graph and a two-dimensional waterfall diagram to give an idea of how the spectrum changes over time. Most of the processing is done on the FPGA. Only a small portion of this system was implemented due to time constraints.

The FPGA takes a large role in the system. It uses a digital mixer to move the spectrum from the frequency of interest down to baseband, applies a multistage decimating low pass filter to spread the spectrum out over the range from DC to the sampling frequency, and then performs an FFT to obtain the spectrum. This process gets repeated for each small section of the spectrum from the start of the frequency range to the end of it. Then the FPGA automatically loops back to the beginning of the spectrum and starts again. As it computes each part of the spectrum, it sends each parts of the spectrum off to the CPU as it is calculated.

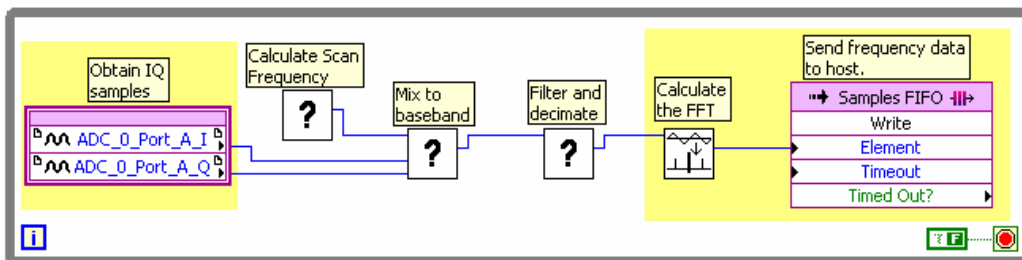


Figure 2. Spectrum monitor design with completed portions highlighted

The host takes the input from the user and computes some parameters for the FPGA operation. It informs the FPGA where to start scanning, how far to step to get to the next frequency to scan, how many steps to make before it loops back to the start, and what decimation factors to use for the stages of the LPF. Adjusting these decimation factors gives some control over the resolution of the final frequency spectrum.

The host is also responsible for presenting the spectrum to the user. As the data comes in from the FPGA, the host needs to clip out the bad parts of the

spectrum that might be attenuated by the filter or overlap with the next spectrum, then it might do some averaging with previous results for that section of the spectrum. When the spectrum is ready, it will present the results to the user in a typical spectrum graph. Also, LabVIEW provides some graphics blocks that could be used to show a waterfall diagram, which can show spectrum usage over time.

Signal sensing can be implemented by testing when the averaged FFT passes above a certain threshold. This could easily be performed on the host side. However, if further functionality gets added to the FPGA to do any analysis of the detected signals, it would be good to add the sensing to the FPGA so there is less communication over the bus.

Only the FFT was actually implemented in this system. A screenshot of the present system is shown in Figure 3. The rest of the system is only planned, and the design may need some modification for it to work correctly. Further details of possible implementations strategies for some of the parts of the system are discussed in the future work section below.

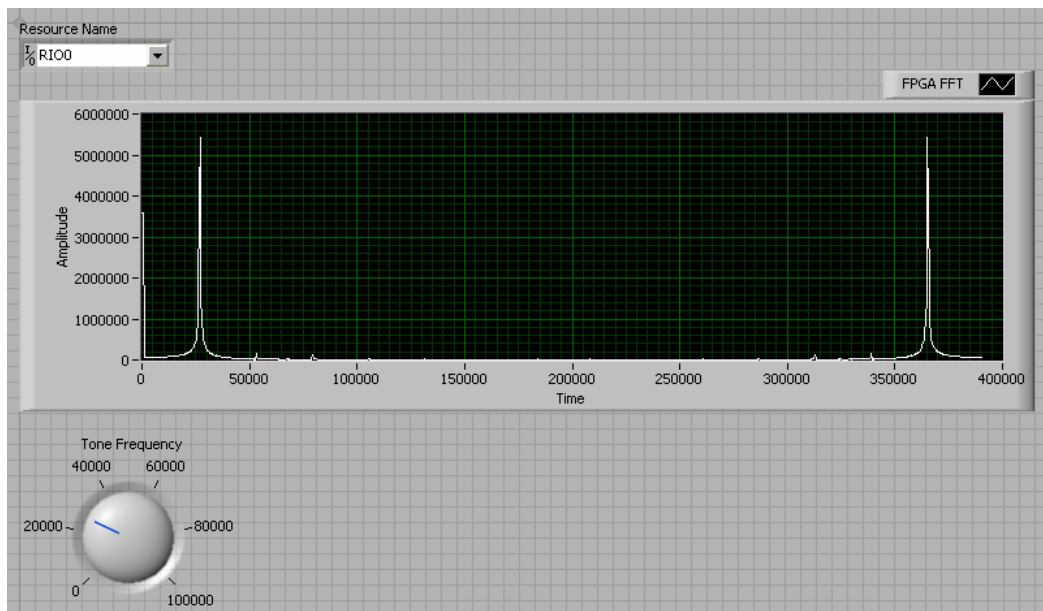


Figure 3. A screenshot of the current system which is displaying the spectrum of a transmitted tone

SYSTEM DETAILS

This section discusses the details of the current system that is actually implemented. The FPGA (Figure 4) has three buttons and one Boolean indicator on its front panel. The “Acquire” button causes samples to be acquired to allow processing to take place. The “FFT” button can be pushed to get one FFT to occur. It must be released and pushed again to get another FFT. The “Get

Samples” button causes the FPGA to send the time domain samples to the host. The “Full” indicator lights when the FIFO for the time domain samples is full.



Figure 4. The FPGA front panel

There are three FIFOs from the FPGA to the host. The first FIFO sends the time domain samples. The I-and-Q samples are signed 16-bit words. The data gets sent to the CPU as a packed unsigned 32-bit double word. The system uses the split numbers and the I16 cast blocks to get the IQ samples back. The other two FIFOs send the real and imaginary parts of the results of the FFT. These values are signed 32-bit double words but are transported as unsigned 32-bit double words. To save on a FIFO, the FFT could be changed to send just the amplitude of the spectrum values.

There are three SCTLs in the FPGA. The configuration loop is a standard loop that all LabVIEW FPGAs should have. The NI VIs that control the FPGA use it to configure the device. It has not been modified. The acquisition loop takes the samples from the ADC and optionally sends them to the host or the FFT loop. The FFT loop continually monitors an internal FIFO for batches of samples. When it obtains enough samples, it will find the spectrum and send it to the host.

When the FFT button is pushed, the acquisition loop sends 1024 samples to the FFT loop. Since the FIFO for the FFT has a depth of only 1028, a new FFT should not be started until the results of the previous FFT have been obtained. This will prevent FIFO overflow.

THE FFT IMPLEMENTATION

The FFT implemented in the FFT loop is a 1024-point, rectangular-windowed, radix-2 FFT. The algorithm works by passing the input through eleven passes. The first pass rearranges the sample values so that they are moved from the n th position of the memory block to a position in the memory block with an index that is n with its ten bits reversed. Then next ten passes form 512 pairs out of the 1024 elements of the array and perform what is called a butterfly on each pair. The different passes of the FFT pair up the values differently.³

The actual FPGA implementation is a bit trickier than the more straightforward textual code representation. There is an enumeration for the different states of the algorithm. These states are “rearranging”, “processing”, “finishing processing”, “transferring result”, and “finishing transferring”. There are also two memory blocks to hold the work in progress. There is one block for the real component of the data and one for the imaginary component of the data.

There are two case structures in the loop with a state wired to their selector nodes. The first case structure keeps a counter that gets incremented when the

algorithm is occurring. This counter is used to detect when a state change is needed. It is also used to determine what operation needs to be done within a certain state. The first case structure should compute the index of the value the algorithm needs to be read from the memory blocks holding the work in progress. Between the two case structures, the value is read from the FFT memory blocks and passed to the second case structure.

In the second case structure, the values read from the memory blocks are processed as needed and an index and a new value is calculated that will be written to the memory blocks. After the second case structure, the new value will be written to the memory blocks.

The “rearranging” state lets the counter go from 0 to 1023. The counter only gets updated when there is a sample obtained from the FIFO. Whenever a sample is obtained, it is moved to the high two bytes of a 32-bit double word and written to the FFT memory blocks at the address that is the counter with its ten lowest bits flipped. The bit flipping is achieved with a subVI that pops bits of the left side of the input value then pushes them onto the right left side of the eventual output value. It uses the rotation blocks from the data manipulation palette to do this since they consume very little FPGA logic.

After the “rearranging” state finishes counter value 1023, the state gets changed to “processing.” This state lets the counter run from 0 to 10239. This allows 1024 clock cycles for each of the ten processing passes. The pass number is one more than the counter divided by 1024. The pair number is stored in bits 1 through 9 of the counter. Each pair requires two clock cycles since it must make two memory reads and two memory writes. Bit zero of counter is used to determine which of the two memory reads to perform for the processing of the pair. Due to pipelining, each pair is processed over a total of six different clock cycles.

The “finishing processing” state is then used to account for the last four clock cycles used in the pipeline for the last pair. This lasts just long enough to allow the processing pipeline to finish its job in the stages to the right of the first case diagram.

After this, the state changes to the “transferring result” state. This state simply reads the result from memory and writes it to the FFT FIFOs.

Like the “finishing processing” state, a “finishing transferring” state follows to allow the pipeline to finish its job in the second case structure. After the “finishing transferring” state, the state gets changed back to the “reordering” state, and the process starts over again.

The rectangular window was chosen because it was the easiest to implement. A better window would improve the frequency resolution of the result. A hanning window would work well. It could be implemented by a convolution manual convolution of the frequency data right before it gets transferred to the host.

FUTURE WORK

This section describes possible implementation strategies for some of the FPGA components that would be needed for the spectrum monitor design presented above. Ideas for a digital mixer and a decimating low pass filter will be discussed.

To scan different sections of the spectrum, the spectrum slices should be mixed down to baseband where they can be filtered and decimated to get better resolution with the FFT. However, a simple cosine mixer has the undesirable property that two parts of the spectrum will overlap, one from positive frequencies and one from negative frequencies. Thus when a spike is detected in the spectrum, it could be from either of two different locations. The Fourier transform of a complex exponential is a single spike. Thus mixing with a complex exponential would cause the whole spectrum to just shift over. This would eliminate the problem of ambiguous signal frequency that a cosine mixer causes.

The phase of the complex exponential could be stored in a fixed point number that ranges from zero to one with several bits of precision. For each frequency, a phase delta could be computed that would be the amount to add to the phase per clock cycle. This would be a constant based on the clock rate of the SCTL that contains it. During each clock cycle, this phase delta could be added to the phase then a lookup table could be used to obtain the values of the real and imaginary parts of the complex exponential. With some modification, the FPGA “Sin-Cos” subVI that is used by the FFT could be reused for this task. Then the complex exponential value could be multiplied with the sample to do the mixing.

After the spectrum slice is at baseband, the mixed data must be filtered to prepare for decimation. LabVIEW provides a few ways to filter on the FPGA. There are blocks for a Butterworth filter, a notch filter, and a finite impulse response (FIR) filter. The FIR filter is fixed to be a LPF with a cutoff frequency at one tenth of the sampling frequency. The Butterworth filter gives more flexibility with the cutoff frequency, but it has a shallow transition band. It may be possible to use the notch filter over the transition band to improve this situation, but this was not tested. Also, the Digital Filter Design Toolkit is supposedly able to generate LabVIEW FPGA code for any filter it designs.

To give a little flexibility over the FFT resolution, the filter could be made two-phase. Both phases would apply a low pass filter and decimate. However, the first decimation value could be changed to vary the final filtered bandwidth.

One limitation of the hardware should be noted here. Although the ADC can run at rates up to 100 MHz, the DDC that comes after the ADC decimates with a minimum value of four. Thus the FPGA can only receive signals at 25 Msp/s. There is an NCO between the ADC and the DDC that can be used to apply a cosine mixer to the signal. Thus, the problem of signal location ambiguity due to cosine mixing will have to be dealt with for scanning frequencies above 12.5 MHz.

CONTROLLING THE NI PCI-5640R

NI provides several VIs for controlling the PCI-5640R from the host side. These are found in the PCI-5640R template project. This template project is among the examples provided with the PCI-5640R Instrument Driver. The template should be used for all new projects targeting the PCI-5640R. This section describes the blocks that have been found to be useful for the host in this system.

The “Configure Timebase” block configures the clocks on the device. Placing this block without wiring any of its inputs except the hardware reference and the error line will cause the clocks to be set to the default state of 100 MHz for the ADCs and 200 MHz for the digital-to-analog convertors (DACs).

The “ADC Default” block configures the ADC with its default configuration. Call this once at the beginning of the host VI to set up the ADC for use.

The “ADC Configure DDC” block configures the decimation value for the DDC. The possible values are 100 and every power of two from 4 to 1024; however, using factors of 512 and 1024 caused errors in testing. With the default ADC clock rate of 100 MHz, the clock rate for the SCTL that acquires samples will be 100 MHz divided by the decimation value.

The “ADC Configure NCO” block configures the frequency that is used in the NCO between the ADC and the DDC. Since the down conversion occurs after the sampler, the maximum practical value is the Nyquist frequency of the sampler.

The “DAC Configure for Single-Tone Mode” block configures the DAC to output a single tone. The frequency and gain of the tone can be passed in to this block. This is useful for wiring the output of the card to the input for testing purposes.

The “DAC Configure for Quadrature Mode” block configures the DAC so that IQ samples can be sent to it from within the FPGA. This is needed for any transmission code.

The “DAC Reset” block resets the DAC so it can be reconfigured. This should be called when the host VI ends if the DAC was used.

The “Check Thermal Shutdown” block is important for continuous operation of the device. It checks the temperature on the board and outputs an error if the temperature is above the maximum that the board allows. The host VI should call this frequently and abort the program if it outputs an error.

DEVELOPMENT AND TESTING

I provide here some advice about the development process when using LabVIEW for this type of application. Also, solutions are provided for some of the problems that I ran into while developing the software.

When developing new features for the software, it may be wise to first write it on the CPU side where there are many more blocks and better debugging

facilities. Also, Mathscript nodes may come in handy for quick prototyping in a text based programming language very similar to MATLAB. Once the software is working on the CPU, then steps can be taken to convert it to code for the FPGA.

Comments are useful to keep the code documented. To add a comment to the block diagram, just double click on empty space to get a text field for writing a comment.

Testing new features on live data from an antenna may not always be the best idea since the data from the antenna is not very predictable. A good alternative is to configure the DAC to use single-tone output, then physically wire the output port on the card to the input port. This way you can predict that there will be a large sinusoidal input coming in to the ADC. Alternatively, samples could be generated on the FPGA instead of reading the samples from the ADC.

Sometimes a broken wire appears that connects the Open FPGA VI Reference block to one of the NI VIs. To fix this situation, try right clicking the Open FPGA VI Reference block and clicking "Select Bitfile..." Then select the compiled version of the FPGA in the "FPGA Bitfiles" folder of the project. If this does not fix it, right click the block and uncheck "Bind to Typedef..." Then, right click the block and click "Bind to Typedef..." again. In the file chooser window, select "ni5640R FPGA VI Reference.ctl" in the "NI-5640R Vis" folder of the project. If this still does not fix it, try double clicking the NI block on the other side of the broken wire. This will open its front panel. If this VI becomes broken by opening it, double click any VIs on its block diagram that are connected to broken wires. When any of these VIs become executable, save them and close them. This should have fixed the wire in the host VI. If other wires are now broken, continue the process on the VIs next the broken wires. Following this process has always fixed the problem for me the few times it has happened.

Another problem that happens occasionally is broken wires appear around FPGA method calls. To fix this, right click the method call block and select another method from the "Methods" submenu. Then switch it back to the method it is supposed to be. If this does not work, try deleting the wires connecting to the node then reconnecting them. The method should be recognized now, and the wires should not be broken anymore.

CONCLUSIONS

The LabVIEW programming environment is found to be good for writing code for an FPGA. However, the set of blocks available for the FPGA is limited. This can lead to longer development times. The hardware seems more than capable for designing a spectrum monitoring system. The main limitations are the long compile times, the occasional compiler failures, and the limited frequency range of the hardware due to the lack of any down converter or configurable filter before the ADC. The LabVIEW graphical programming environment took a while to get used to; but became much more productive within the system once the authors were familiarized with the program.

ACKNOWLEDGEMENT

This material is based upon work supported by the National Science Foundation under Grant No. EEC-0755081.

REFERENCES

1. http://hraunfoss.fcc.gov/edocs_public/attachmatch/FCC-04-113A1.pdf
2. <http://research.microsoft.com/netres/projects/KNOWS/>
3. "The FFT Demystified," <http://www.engineeringproductivitytools.com/stuff/T0001/index.html>

EXPERIMENTAL CHARACTERIZATIONS OF THE IONIC WIND UNDER DC EXCITATION

Joseph O'Bruba*, Russell Vela[†], and Victor P. Pasko[‡]

Department of Electrical Engineering
Pennsylvania State University, University Park, PA 16802

*Undergraduate Student of the BioEngineering Department
Pennsylvania State University
University Park, PA 16802

ABSTRACT

The corona discharge is a type of gas discharge which is commonly found in high voltage engineering. Once formed, the corona discharge maintains a region of ionization and a region which is dominated by momentum transfer collision between drifting ions and ambient gap molecules, typically called the unipolar drift region. The momentum transfer collisions induce flow of neutral gas known as 'ionic wind'. Ionic wind generating electrode configurations most frequently found in literature are the point-to-plane, point-to-ring, and point-to-grid [1-4]. This paper utilizes the point-to-ring geometry as a baseline for comparison to an electrode design which allows for multiple corona initiation sites within a single gap spacing. Wind velocity, voltage, and current are recorded for each configuration and are taken at gap spacings of 6.35 mm intervals. Due to design constraints, voltages are limited to ± 34 kV. A wind vane anemometer is used to record wind velocities at 12.7 mm behind the exhaust stage. Variations in electrode material are also tested and the corresponding changes in parameters are presented.

INTRODUCTION

The first reported discovery of the corona induced ionic wind was by Tiberio Cavallo in 1777 [4]. Since then, many researchers have endeavored to explain the

[†]Graduate Mentor

[‡]Faculty Mentor

phenomenon, but it was not until the 1960s when Stuetzer, building upon the work of Loeb ^[5] and Harney ^[6], formulated an explanation of the ionic wind. Presently, ionic wind generators are being utilized in a variety of applications such as cooling systems ^[7], dielectric barrier discharges (DBDs) ^[8], elimination of bacterial cells ^[9], and surface treatment^[10]. The most common electrode geometries found in literature used to generate ionic wind are the point-to-plane, point-to-ring, and point-to-grid ^[1-4]. Novel electrode geometries are presently being researched and are assisting in strengthening the library of ionic wind generators and their applications ^[7, 11, 12].

The ionic wind designs presented in this paper are based on the corona discharge. The corona discharge is a type of gas discharge which by its default contains both the ability to ionize and accelerate a body of gas. Electrode geometries, such as the plane-to-plane, generate symmetric electric field lines which lack the development of a space charge region. The space charge region develops an area of high ionization. Electrode geometries, such as the point-to-plane, develop asymmetric electric field lines, which lead to a space charge development and thus the corona discharge regime.

This paper presents the experimental data for a metal brush-like electrode, which allows for multiple corona initiation sites within a single gap. Comparisons to a baseline electrode configuration will also be displayed. For the experiment herein, two types of electrode configurations are used: point-to-ring and brush-to-ring. For each electrode configuration positive and negative voltages are applied ($\leq \pm 34$ kV). Varying materials (carbon steel, brass, stainless steel) are tested for the brush electrode and the effects are presented. Gap spacing between electrodes are at intervals of 6.35 mm.

For each experimental test, pressure, humidity, and temperature are recorded. The set-up of the experiment, shown in Figure 1, contains a set of rails which both hold the electrodes in place and allow for easy connection to either the ground or voltage. The housing is made of polycarbonate. The electrodes are connected to the excitation and ground rails by metal screws. Since the stand of the electrodes are metal, Kapton tape is used to cover all possible electrical breakdown points. Prior to each experiment, powder-free Nitrile gloves are worn and each electrode is cleaned with cyclohexane. In addition to the recording of wind velocity via a wind vane anemometer, the amperage is recorded at voltage intervals of 1 kV. Measurements begin at the voltage where the first emission of visible light is observed (i.e. onset streamers, glow discharge regime).

EXPERIMENTAL DESCRIPTION

Experimental Setup

As seen in Figure 1, the electrode stands are fitted into a \sqcup shaped slot 25.4 mm deep. This slot allows for the inner electrode distance to be easily adjusted and for electrode staging in future experiments. Of the two outer rails, one is connected

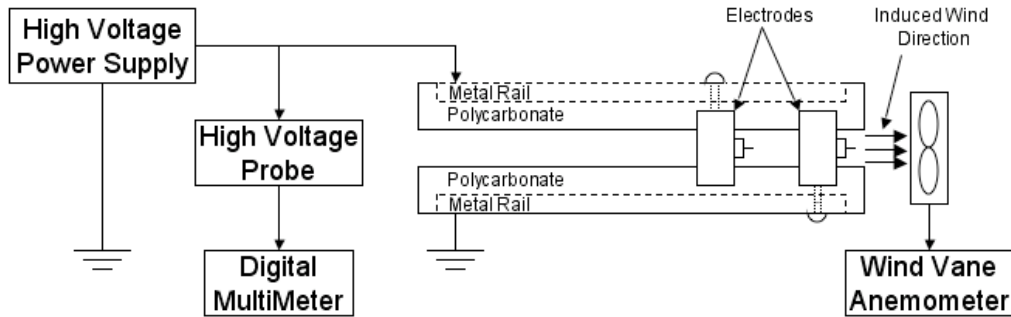


Figure 1: Depiction of the experimental configuration used during testing. The electrodes are shown in the positive point-to-ring configuration.

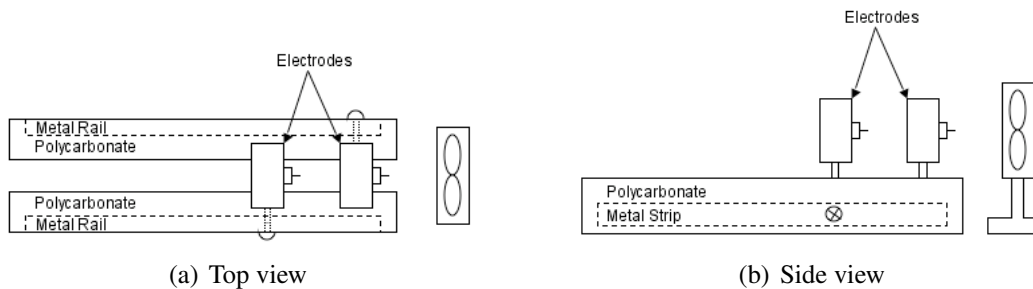


Figure 2: Electrode and wind vane anemometer arrangement generally used in reported experiments. The electrodes are shown in the negative point-to-ring configurations.

to positive voltage and the other to ground. The electrodes are connected to the rails by screws which connect through 38.10 mm of polycarbonate. For a positive voltage electrode configuration, the positive voltage electrode is on the left, and the grounded electrode is on the right, as seen in Figure 1. In the negative voltage arrangement, the grounded electrode is on the left, and the positive electrode on the right, see Figure 2. Prior to every experiment, each electrode is cleaned using cyclohexane.

Electrical Diagnostics

The voltages are measured by the use of a Fluke (model: 80k-40) high voltage probe, which are then monitored on an impedance matched Fluke Digital MultiMeter (DMM). The high voltage generator (Glassman model: EH40P2.5) is capable of producing a maximum of 40 kV. Due to safety concerns with sensitive diagnostic equipment, ± 34 kV is the maximum possible voltage. Amperage is recorded directly from the high voltage power supply. The wind velocity is measured by a wind vane anemometer (Extech model: 407112), which is placed directly behind the electrodes at a distance of 12.7 mm, see Figure 1.

Electrode Geometry

As seen in Figure 3, two types of electrode arrangements are used: point-to-ring and brush-to-ring. The diameter of the ring is 50.80 mm and has a width of 12.70 mm. The corona initiation electrode dimensions include the point with a diameter of 0.52 mm and the brush whose bristles have a diameter of 0.10 mm.

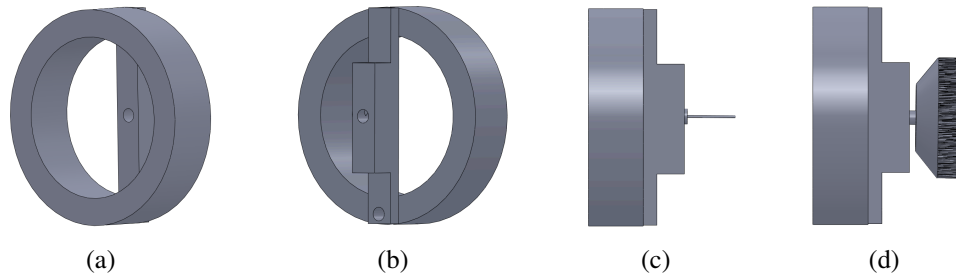


Figure 3: CAD representation of the electrode configurations rendered using Solidworks. (a, b) Ring electrode, (c) point-to-ring configuration, (d) brush-to-ring configuration.

For this paper, there are four types of electrode configurations: the aluminum point-to-ring, the carbon steel brush-to-ring, the brass brush-to-ring, and the stainless steel brush-to-ring. The different types of materials used for the brush-to-ring configurations are important to note due to their varying work functions. Photons incident upon the cathode surface whose energy exceeds the work function may eject electrons from the surface^[13]. Table I gives the material constituents, the element percentages within the material, and their corresponding work function. Since the work needed to remove electrons from the electrode surface is much smaller than the ionization energy of oxygen and nitrogen molecules (12.06 eV for oxygen and 15.6 eV for nitrogen), the number of electrons photo-emitted from the electrode surface is far higher than those generated by electron impact collisions in air^[14]. This process becomes more appreciable in negative corona, where the main method of electron generation is through photoemission^[13].

RESULTS AND DISCUSSION

Electric Field Distributions

Electrostatic simulations of the two types of electrode configurations were performed using Ansoft's Maxwell 2D modeling software^[16]. Figure 4 displays the analysis of the point-to-ring and the brush-to-ring positive voltage setups. The geometry of the models are based on the actual dimensions used in experimentation. However, the model of the brush had to be altered to contain fewer bristles due to computational constraints. Variations in the electric field magnitude for both geometries can be seen in Figure 4. The gap distance for the point-to-ring is 31.75 mm and 19.05 mm for the brush-to-ring.

Table I: Description of the materials used in this study. Component percentages and work functions are shown ^[15].

<i>Material</i>	<i>Components</i>	<i>Work Function ϕ (eV)</i>
Aluminum	Al (99%)	4.20
Carbon Steel	Fe (97%)	4.67
	C (2%)	5.00
Brass	Cu (66%)	4.48
	Zn (33%)	3.63
Stainless Steel	Fe (88%)	4.67
	Cr (11%)	4.50

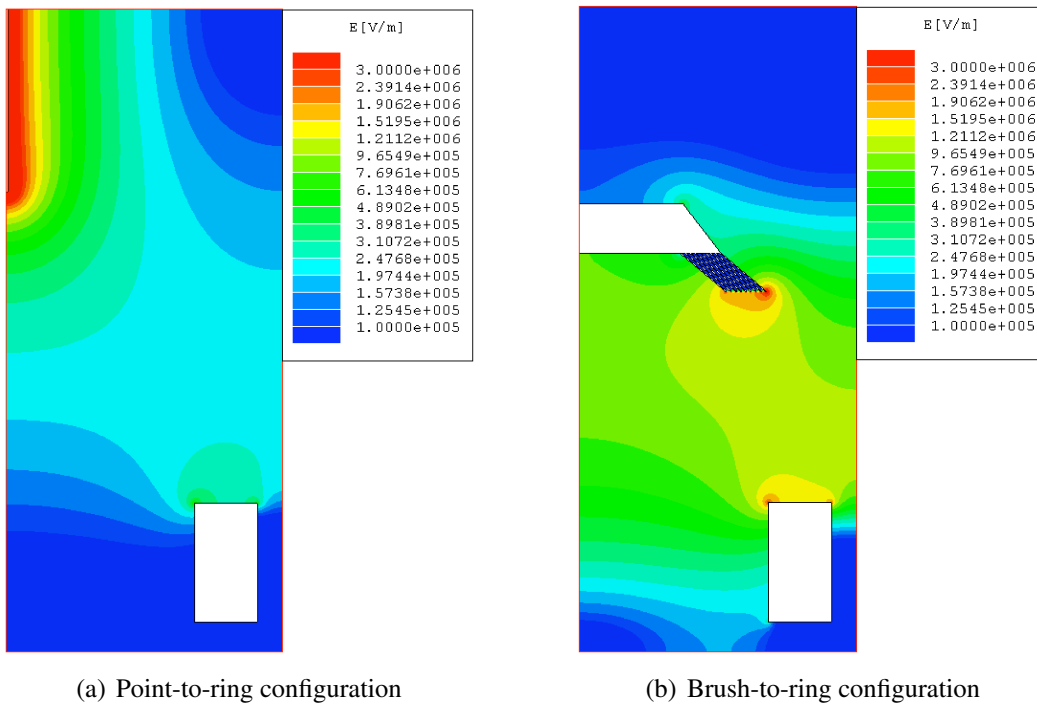


Figure 4: Maxwell 2D electrostatic simulations of the electrode configurations used in testing. The figure shows cross-sectioned views of the distributions of the electric field magnitude for the electrode configuration

Aluminum Point-to-Ring Configuration

The results for the positive and negative voltage aluminum point-to-ring setup shown in Figures 1 and 2 are presented in Figure 5. For the sake of comparison, it is noted that the corona discharge depends not only on the electrode geometry, but the polarity of the field as well ^[17]. In Figure 5a, the amount of amperage used with positive voltage was higher with smaller gap spacing, and steadily decreased

with increasing gap spacing and voltage. Figure 5b shows that when compared to the positive electrode configuration, the negative voltage produces larger amperage values. With increasing gap distance and voltage, the negative voltage amperage values were relatively similar. Again, the amperage values for both the positive and negative voltages followed a parabolic-like trend.

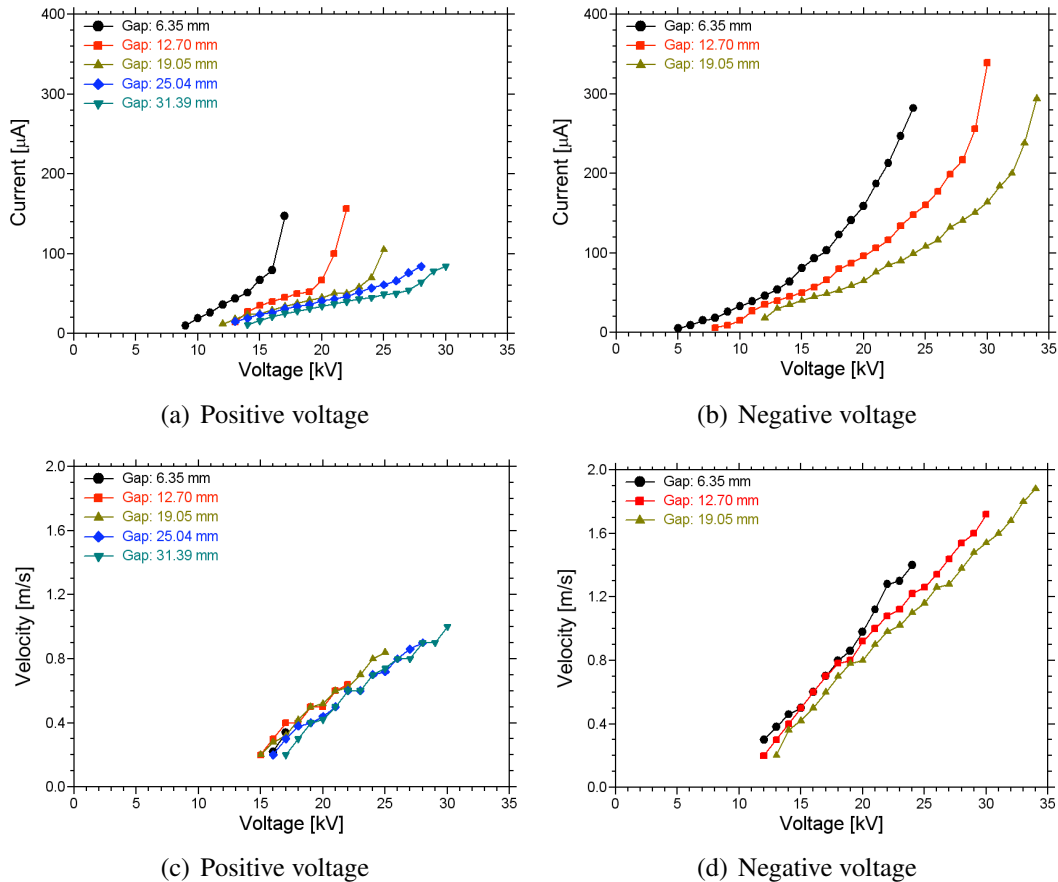


Figure 5: The characterizations for the single stage aluminum point to ring electrode configuration. Panels (a,b) show the voltage and current recorded, while (c,d) show the ionic wind velocities as a function of the corresponding voltages.

Figure 5c displays the recorded wind velocity for the positive voltage. With increasing gap distance, a larger velocity value was produced. This increase in velocity is expected because the force on the ions from the electrical field, which increases as the voltage difference is increased, must balance the force exerted from ions on the gas molecules generating the wind [5]. Figure 5d displays the wind velocities recorded for the negative voltage. An increase in velocity with increasing gap distance is observed, as well as a greater velocity than for the positive voltage,

Figure 5c. The increase in velocity for the negative voltage can be attributed to a larger unipolar charge density for this polarity, which lead to a greater momentum transfer to neutral particles ^[13]. For both voltage arrangements, the velocity appears to increase linearly with respect to both gap distance and voltage.

Carbon Steel Brush-to-Ring Configuration

The carbon steel brush-to-ring configuration produced the results displayed in Figure 6. For the positive voltage in Figure 6a, the level of amperage values were largest at the shortest gap distance (6.35 mm). Figure 6a displays a steady trend of decreasing amperage as the gap distance and voltage increased. With the carbon steel brush-to-ring setup, the positive voltage amperage values are much larger than the point-to-ring setup. In the carbon steel brush-to-ring negative voltage configuration, the amperage values are slightly less than the amperage values for the point-to-ring configuration, see Figure 6d.

Similar to the point-to-ring configuration, Figure 6c displays how the carbon steel brush-to-ring positive voltage setup produced an increasing wind velocity as the gap distance increased. However, the carbon steel brush-to-ring setup led to larger values of velocity in comparison to the point-to-ring setup. Figure 6d also shows that the negative voltage wind velocity was greater with increasing gap distance and produced higher values than the positive voltage, as was the case for the previously discussed point-to-ring setup. Similar to the point-to-ring setup, the amperage values had an increasing parabolic trend for the positive and negative voltages. The velocity increased linearly for both positive and negative voltages.

Brass Brush-to-Ring Configuration

The brass brush-to-ring results are shown in Figure 7. Figure 7a shows that for the positive voltage configuration, the amperage reached a maximum at the 19.05 mm gap spacing. The amperage amplitudes for the negative voltage configuration were very similar to the previous two electrode arrangements. Comparable to the aluminum point-to-ring and carbon steel brush-to-ring, the current amplitudes appear to increase proportionally to voltage squared.

The velocity profiles for the brass brush-to-ring follow a similar trend as for the carbon steel brush-to-ring configuration, as seen in Figures 7c and 7d. A distinguishable difference between the two types of brushes was that the brass brush produced a higher velocity for both the positive and negative voltages. As with the previous setups, the ionic wind velocity values followed a linear trend with increasing gap distance and voltage.

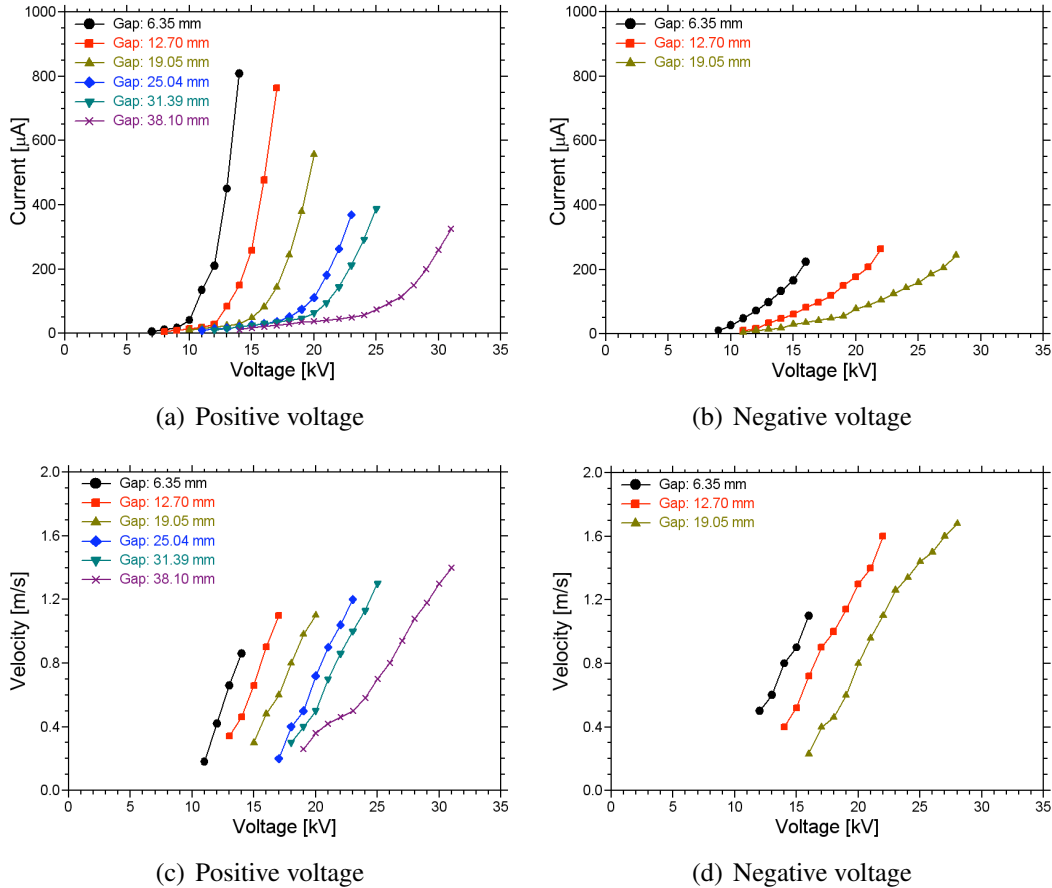


Figure 6: The characterizations for the single stage carbon steel brush to ring electrode configuration. Panels (a,b) show the voltage and current documented, while (c,d) show the ionic wind velocities as a function of the corresponding voltages.

Stainless Steel Brush-to-Ring Configuration

The results for the stainless steel brush-to-ring configuration are presented in Figure 8. For the positive voltage, the amperage was greatest at the smaller gap spacings and steadily decreased after the 12.70 mm gap spacing. Figure 8b displays the amperage utilized during the negative voltage, which follow a similar trend to the levels of amperage for the previously mentioned electrode arrangements using the negative voltage.

The positive voltage for the stainless steel brush-to-ring setup had the velocity increase at a low rate when compared to previous materials, see Figures 8c, 7c, and 6c. The negative voltage had a velocity distribution similar to the carbon steel and brass brush-to-ring setups, see Figure 8d. Once again, the velocity increased linearly for both the positive and negative voltages, which has been the case for each electrode configuration discussed.

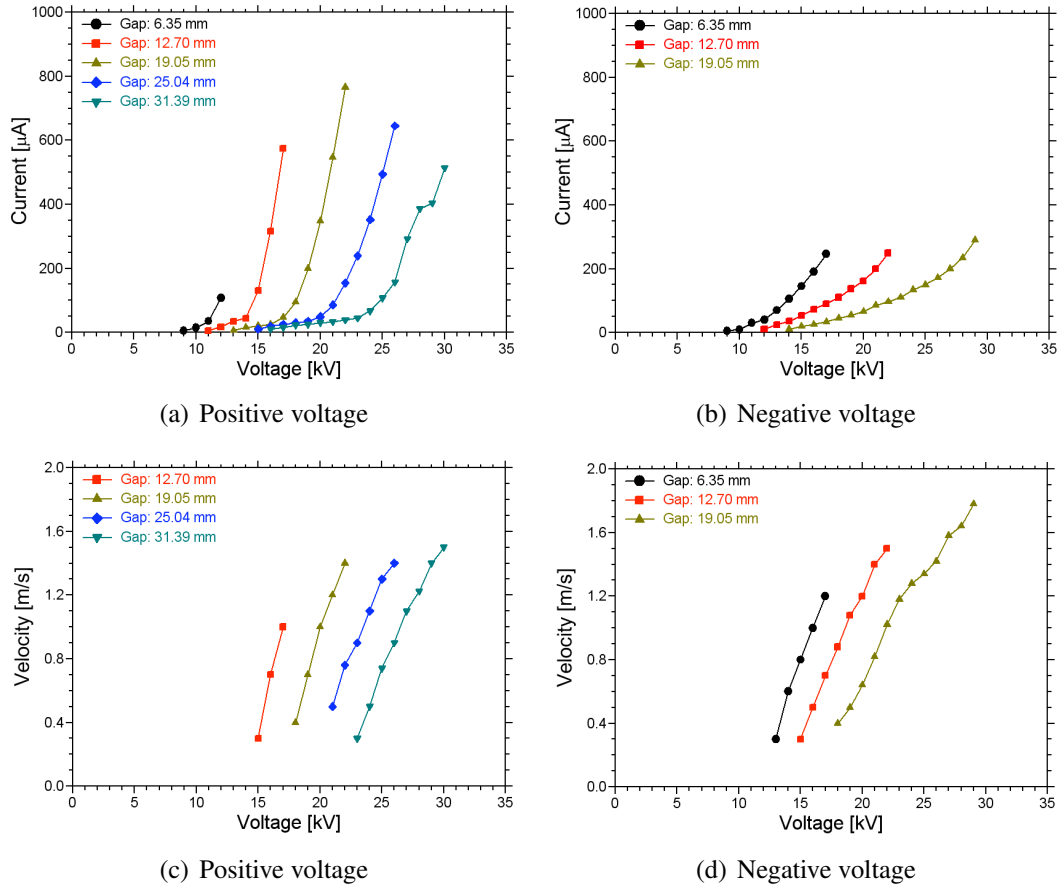


Figure 7: The characterizations for the single stage brass brush to ring electrode configuration. Panels (a,b) show the voltage and current documented, while (c,d) show the ionic wind velocities as a function of the corresponding voltages.

Breakdown Voltage Curves

Figure 9 displays the breakdown voltage curves pertaining to both the positive and negative voltages for the aluminum point-to-ring, carbon steel-brush-to-ring, brass brush-to-ring, and stainless steel brush-to-ring electrode configurations. With respect to the individual gap spacings, the negative voltage was at a higher breakdown voltage than the corresponding positive voltage. For both the positive and negative voltages, the aluminum point-to-ring has a higher breakdown voltage than the varying types of brush-to-ring electrodes see Figure 9a.

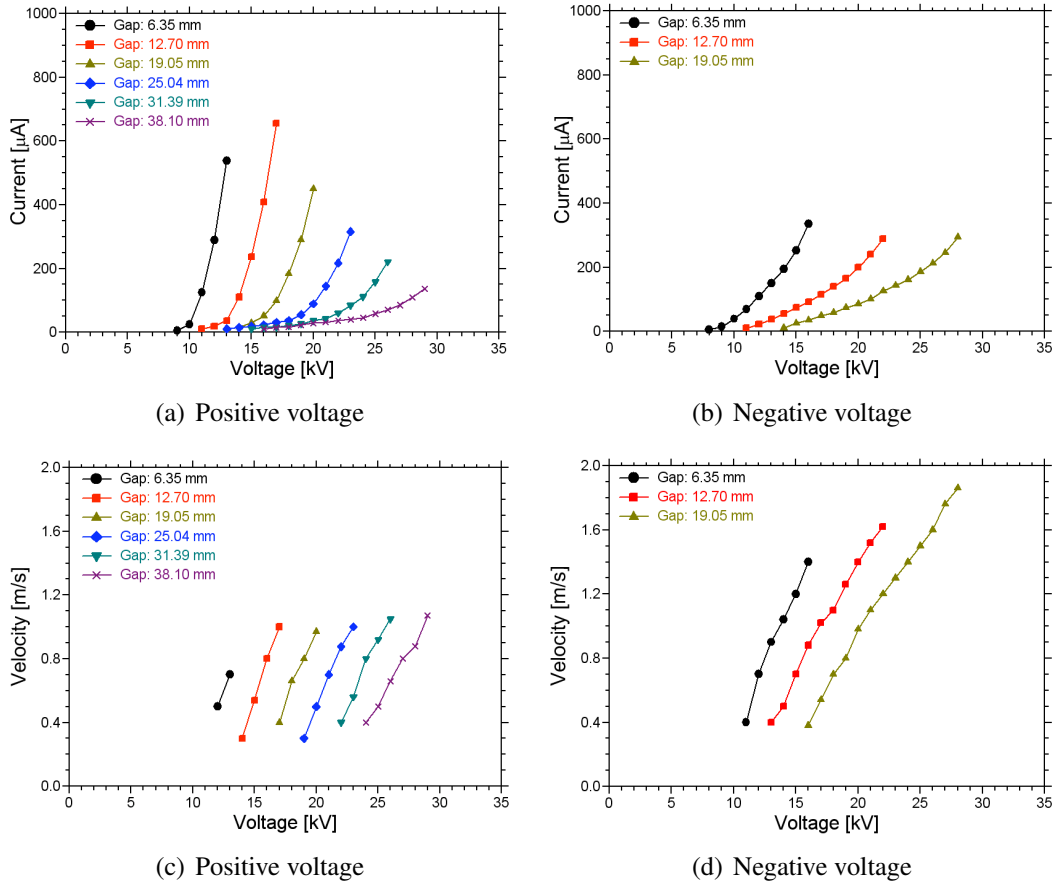
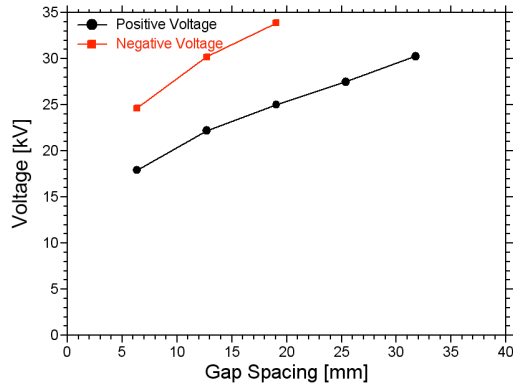


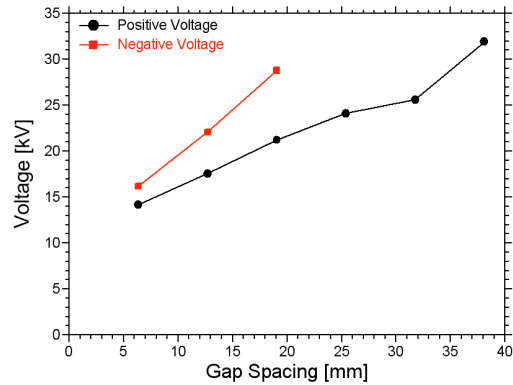
Figure 8: The characterizations for the single stage stainless steel brush to ring electrode configuration. Panels (a,b) show the voltage and current documented, while (c,d) show the ionic wind velocities as a function of the corresponding voltages.

CONCLUSIONS

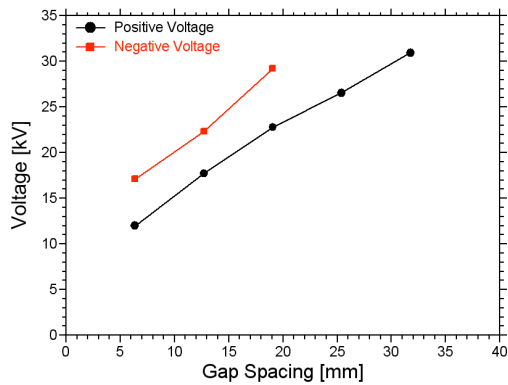
The results presented in this paper document varying current, ionic wind velocities, and breakdown curves as a function of applied voltage for the following electrode configurations: aluminum point-to-ring, carbon steel brush-to-ring, brass brush-to-ring, and stainless steel brush-to-ring. Distinct differences were seen between these geometries when positive and negative voltages were applied. In each electrode geometry, the negative voltage produced a greater ionic wind velocity than the positive voltage, as summarized in Figure 10. The greatest velocity produced for the positive voltage configuration was by the brass brush-to-ring setup. The greatest velocities produced for the negative voltage configuration was obtained for the stainless steel brush-to-ring and the aluminum point-to-ring electrode setups.



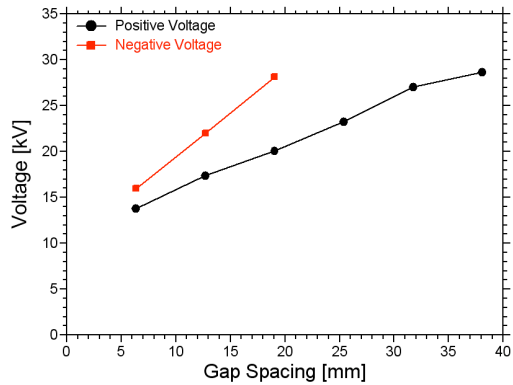
(a) Aluminum point-to-ring



(b) Carbon steel brush-to-ring



(c) Brass brush-to-ring



(d) Stainless steel brush-to-ring

Figure 9: Breakdown voltages for different electrode configurations.

For both voltage polarities, the trends found in each electrode setup were that the current increased in a parabolic-like fashion and the velocity increased linearly with respect to voltage for different gap spacings.

As one of the goals of this paper was to determine the experimental differences between the point-to-ring and brush-to-ring geometries, the results show that the aluminum point-to-ring positive voltage configuration produced the smallest ionic wind velocity when compared to the varying types of brush-to-ring at the positive voltage configuration (see Figure 10a). However, the aluminum point-to-ring negative voltage configuration generated the largest ionic wind velocity when compared to the brush-to-ring negative voltage configurations (see Figure 10b). Experimental data for the previously mentioned configurations can be found in Figures 5 through 9. Another objective of this paper was to see if varying the electrode material for corona initiation sites would produce different results. As seen in Figures 6 through 8, the levels of current and ionic wind velocity were directly affected by the variations in material types. Figures 9b, 9c, and 9d show breakdown curves for each

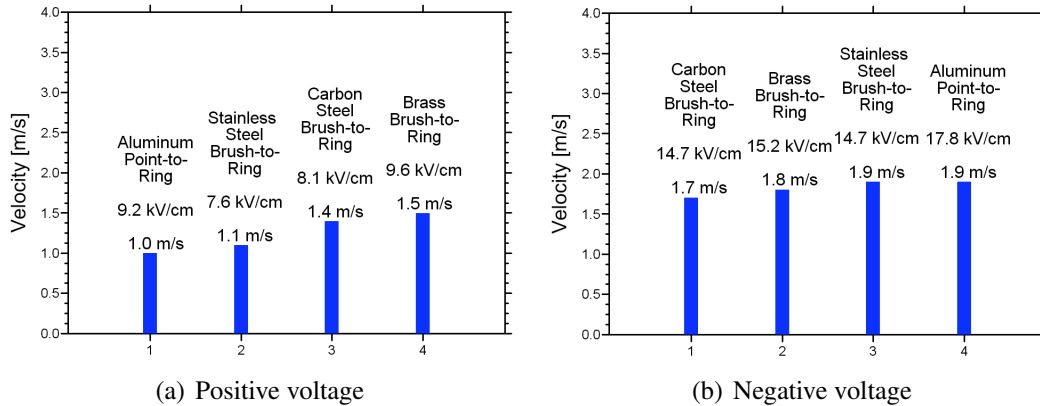


Figure 10: Comparison between all single stages tested for both the (a) positive and (b) negative polarities. Results recorded in a 1 atmosphere environment, with a relative humidity of approximately 65% and a temperature of $\sim 25^\circ\text{C}$.

type in brush-to-ring configuration, demonstrating significant dependence on material properties.

Future experimentation will consist of going beyond single staging of the electrodes and documentation relating current and ionic wind velocity trends. By using the results presented here, optimal gap lengths, materials, and voltage polarities can be utilized so to obtain greater ionic wind velocities in future multi-stage configurations. Carbon steel, brass and stainless steel point-to-ring configurations will also be developed to compare with the brush-to-ring results presented here.

ACKNOWLEDGEMENT

The author would like to thank Russell Vela, Jérémy Riouset, Victor P. Pasko, and the Pennsylvania State University Electrical Engineering Department for their support. This material is based upon work supported by the National Science Foundation under Grant No. EEC-

REFERENCES

- ¹ P. Giubbilini, "Mobility measurement of large ions in air from a point-to-ring corona source," *American Institute of Physics* (1997).
- ² Y. Teisseyre, R. Haug and P. Ballereau, "Movement of atmospheric dust in a point-to-grid corona discharge," *Phys. D: Appl. Phys.*, **15** 1231–1242 (1982).
- ³ G. W. Trichel, "The mechanism of the negative point to plane corona near onset," *Physical Review*, **54** 1078–1084 (1938).
- ⁴ Z. Kucerovsky, W. D. Greason and A. Weigl, "Corona wind in a system with

- the pin-to-plane discharge geometry,” in: “Industry Applications Conference,” 1999.
- ⁵ L. B. Loeb, *Electrical Coronas*, University of California Press, 1965.
 - ⁶ D. J. Harney, An aerodynamic study of the “electric wind”, Master’s thesis, California Institute of Technology, Pasadena, California (1957).
 - ⁷ C. Hsu, N. Jewell-Larsen, I. Krichtafovitch, S. W. Montgomery, J. T. Dibene and A. V. Mamishev, “Miniaturization of electrostatic fluid accelerators,” *Microelectromechanical Systems*, **16** (4) (2007).
 - ⁸ L. Leger, E. Moreau and G. Touchard, “Effect of a DC corona electrical discharge on the airflow along a flat plate,” *IEEE Transactions on Industry Applications*, **38** (6) 1478–1485 (2002).
 - ⁹ J. Ouellette, “Cold plasmas enter the biomedical arena,” *Physics Today*, pp. 23–25 (2007).
 - ¹⁰ M. Goldman, A. Goldman and R. S. Sigmond, “The corona discharge, its properties and specific uses,” *Pure and Appl. Chem*, **57** (9) 1353–1362 (1985).
 - ¹¹ F. Weinberg, F. Carleton, D. Kara, A. Xavier, D. Dunn-Rankin and M. Rickard, “Inducing gas flow and swirl in tubed using ionic wind corona discharges,” *Experiments in Fluids*, **40** 231–237 (2006).
 - ¹² J. L. Brisset, “Air corona removal of phenols,” *UFR des Sciences*, pp. 179–183 (1996).
 - ¹³ E. Kuffel, W. Zaengl and J. Kuffel, *High Voltage Engineering: Fundamentals*, Butterworth-Heinemann, 2000.
 - ¹⁴ J. Chen and J. H. Davidson, “Model of the negative DC corona plasma: comparison to the positive DC corona plasma,” *Plasma Chemistry and Plasma Processing*, **23** (1) 83–102 (2003).
 - ¹⁵ D. R. Lide, *Handbook of Chemistry and Physics*, 81st ed., CRC Press, 2000.
 - ¹⁶ A. Corporation, “Maxwell 2D,” (2008), URL <http://www.ansoft.com/>.
 - ¹⁷ J.-S. Chang, P. A. Lawless and T. Yamamoto, “Corona discharge processes,” *IEEE Transactions on Plasma Science*, **19** (6) 1152–1166 (1991).

IMPLEMENTATION OF AN IONOSONDE USING SOFTWARE-DEFINED RADIO TECHNIQUES

Danielle R. Bell*, Ryan L. Seal⁺, and Julio V. Urbina[#]

Department of Electrical Engineering
The Pennsylvania State University,
University Park, PA 16801

*Undergraduate student of
Department of Computer Science
Grove City College
Grove City, PA 16127

ABSTRACT

With the rapid emergence of new standards and protocols in wireless communication, many functions of traditional radio receivers are being implemented in software [6, 9]. These new radio receivers are called software radios since their implementation relies heavily on digital signal processing techniques and require fewer radio frequency components than classic analog radios. Consequently, by utilizing software radio algorithms, it is possible to implement various types of radar receivers at a very low cost and simultaneously exploit the benefits a digital system offers, such as high dynamic range, perfect coherent quadrature detection, and programmable filters. This project attempts to implement low-cost receiver and transmitter sections of an ionosonde system based on software-defined radio (SDR) techniques in conjunction with universal software radio peripheral (USRP) boards and related open source software available from the GNU Radio project. In General, an ionosonde is special-purpose radar that can transmit and receive a range of radiowaves with frequencies from about 1 to 20 MHz. These radiowaves scatter back echoes from the ionosphere, which in turn are sampled to infer useful information about the density composition of the ionosphere.

⁺ Graduate Mentor

[#] Faculty Mentor

INTRODUCTION

The concept of an ionosonde was first introduced in 1925 by Gregory Breit and Merle Tuve. To date, ionosondes are one of the most basic, yet useful instruments that are used to gather data about the ionosphere [4]. The ionosphere is not static but is constantly changing due to solar flux variability, which is primarily a result of both the ultraviolet radiation from the sun and magnetic activity [12]. With the help of ionosondes, much has been learned about the ionosphere, and its influence on the earth.

Ionosondes transmit a radiowave signal to the ionosphere; a portion of this radiowave is scattered back and measured at the receiver after a delay in time [1]. The echo delay scattered back from the ionosphere, is recorded as a function of frequency [5], and this record is called an ionogram. Essentially, ionosondes take basic measurements that lead to the determination of the electron density of the ionosphere at a given height. They have played a large role in many research areas, including but not limited to radio science, plasma physics, telecommunications, and environmental studies [7]. In addition to their effectiveness in research, ionosondes have also supplied invaluable information for radio communications in military operations during both times of war and peace [5].

Currently, traditional ionosondes are relatively expensive instruments, but they also continue to remain to be extremely beneficial tools. The purpose of this project is to implement both software-defined radio transmitter and receiver sections of an ionosonde using the Universal Software Radio Peripheral (USRP) system combined with the open source GNU Radio project software. Success of this project would produce a more reasonably priced alternative to conventional ionosondes and provide excellent hands-on training for aspiring engineers. In addition to economic benefits, this system, due to its software-based architecture, would simplify the maintenance, manufacturing, and distribution practices as well as simplify the process of gathering and analyzing data.

EXPERIMENTAL DESCRIPTION

GNU Radio Project Software

The GNU Radio project software provided a simple way to interface with the USRP board, and an overview of this is displayed in a flowgraph in Figure 1. The GNU Radio library is a collection of primitives useful for signal processing and provides a straight-forward way to hold everything together [2]. The programmer

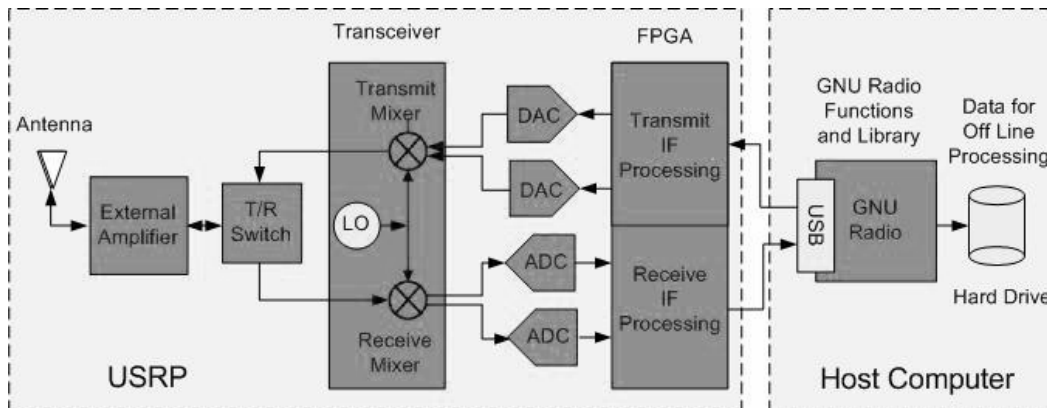


Figure 1: The USRP board forms the RF front end to the ionosonde and utilizes the computer's resources through the USB bus and the GNU Radio software package [8].

begins by producing a graph, which consists of signal processing blocks called nodes and data flow connections called edges, which exist between nodes. The underlying signal processing blocks are written in C++ to provide faster performance on time-critical calculations, and these blocks are connected using Python, an interpreted language which provides a less complicated interface for manipulating the blocks. Simplified Wrapper and Interface Generator (SWIG), an interface compiler, integrates the C++ and Python code to enhance computational performance while abstracting away unnecessary complexity from the programmer.

USRP Board

The complete system was built around a USRP motherboard, which is shown Figure 2. The USRP board was selected for this project for the following reasons: has a relatively low cost, is open source software, can produce the range of frequencies needed, can sample echoes return at a very high rate, is portable—due to USB base. Originally developed by Matt Ettus, this board is currently distributed by Ettus Research LLC [5] and was designed to increase flexibility of communications systems and devices via simple, inexpensive hardware to facilitate the development of cognitive radios [11]. The USRP can control up to four 12-bit 64 MSPS Analog-to-Digital Converters (ADC) as well as four 14-bit 64 MSPS Digital-to-Analog Converters (DAC).

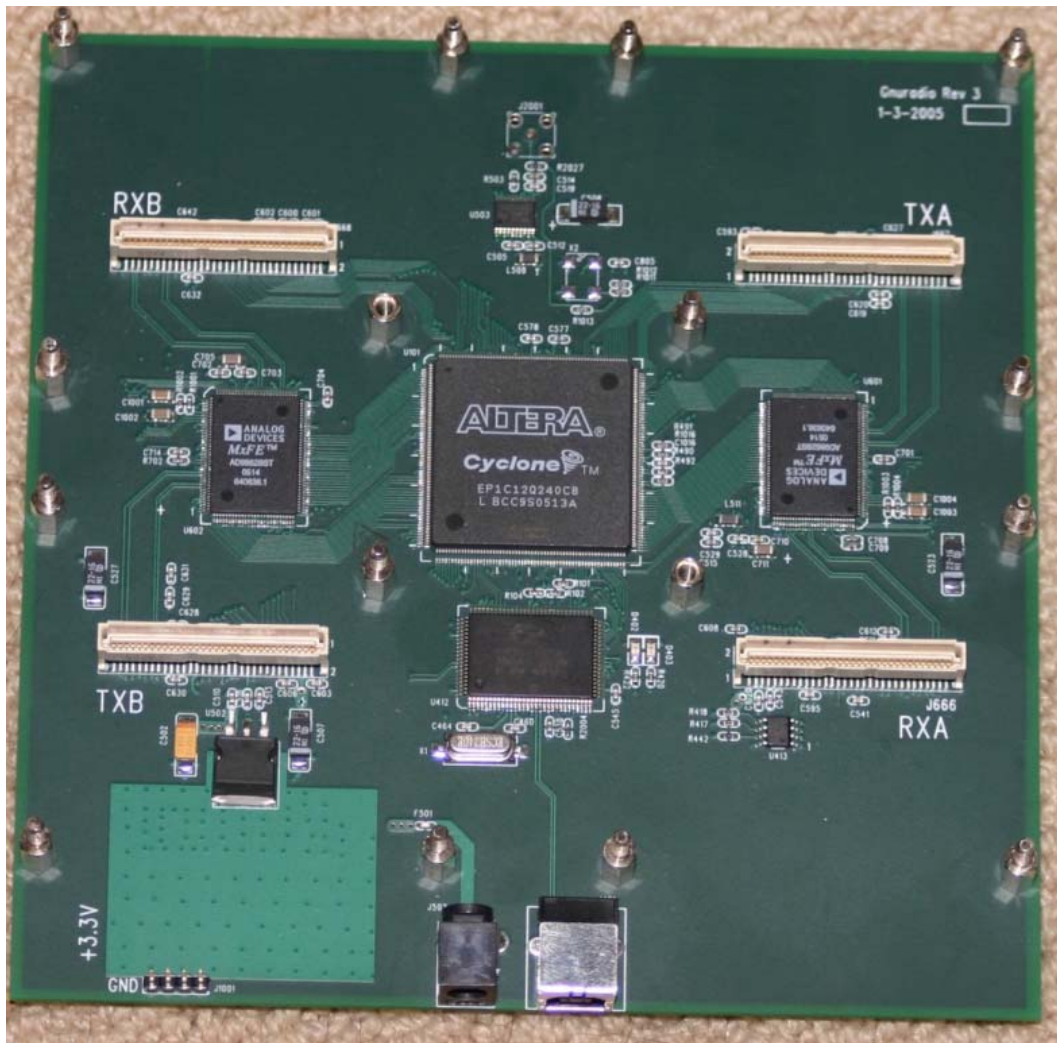


Figure 2: USRP motherboard that formed the base for this project [14]

A block diagram of the board is illustrated in Figure 3 [10]. The motherboard also provides both a field programmable gate array (FPGA) and a programmable Cypress FX2 USB 2.0 controller [2].

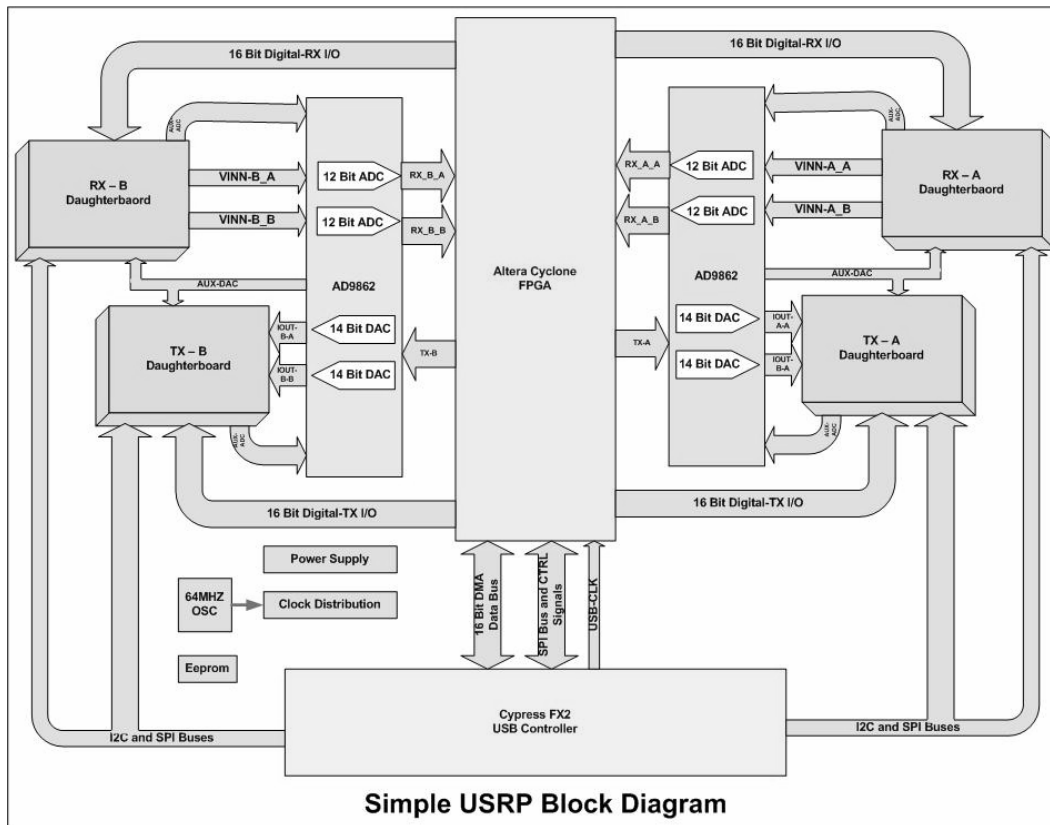


Figure 3: Layout of a USRP motherboard [3]

For this project, two daughterboards, also manufactured by Ettus LLC., were attached to the motherboard, providing the system's RF front-end. Both the Basic TX daughterboard and a LFRX daughterboard, which are depicted in Figure 4 a and b, respectively, were utilized for this project. However, due to frequencies defined by the project, any combination of Basic TX/LFTX and Basic RX/LFRX daughterboards would serve as acceptable replacements. The Basic TX daughterboard is capable of transmitting signals between 1 and 250 MHz while the LFRX daughterboard is able to receive signals with frequencies from 30 MHz all the way down to the DC range [14]. Since the transmit and receive signals for this project range from 1 up to 20 MHz, both boards span the necessary frequencies.

(a)



(b)

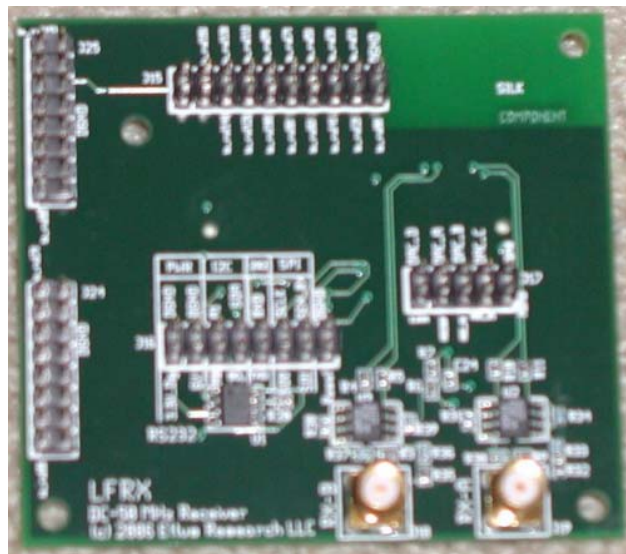


Figure 4: The Basic TX daughterboard that provided RF front end for transmitting signals in the range of one to 250 MHz is shown in (a), and the LFRX daughterboard that provided the RF front end for receiving signals with a frequency between the DC range and 30 MHz is shown in (b) [14].

The assembled boards were connected to a computer running the Ubuntu operating system (distribution 8.04, Hardy Heron), and it was determined, through the use of a benchmarking program provided by the GNU Radio package, that the USB controller could manage up to 32 MBS of continuous throughput; thus leading to the conclusion that, at most, 8 MSPS of complex samples may be transferred over the USB bus [13], limiting the system's bandwidth to 8 MHz.

RESULTS

Due to project time constraints, only the transmitter software portion of the system was implemented. The methods used to accomplish this task will be expounded in the following sections.

After analysis, the motherboard's configuration did not appear to support both transmitter and receiver modules on the same board. According to Dhar et al [10], the TX daughterboards continued to transmit even after emptying their buffers, resulting in signal corruption when both transmitter and receiver modules resided on the same motherboard. Due to inherent software design limitations (non real-time task scheduling) present in the current implementation of the GNU Radio software library, consistent execution times between blocks was not achievable. Due to these limitations, the original design requirements, which required a single motherboard containing both transmit and receiver modules, could not be achieved.

Given the previously mentioned time constraints, an effort was focused on completing the transmitting section, and a detailed summary of this work is given in the following section.

DISCUSSION

The base class for the transmission segment of the program was derived from GNU Radio's `top_block` class, which provided the basic framework required for a signal processing block. Utilizing several functions, the transmitted wave was generated by the computer connected to the USRP board. Since the USRP device transmits the signal, it was set up as a signal sink and connected to the computer-generated source. All of this work was encapsulated within the initialization section of the parent class, enabling the program to follow the format of the flowgraph shown in Figure 5.

At the conclusion of this project, the timing section of the transmitter still required more debugging, but the remainder of the algorithm was completely translated into working code.

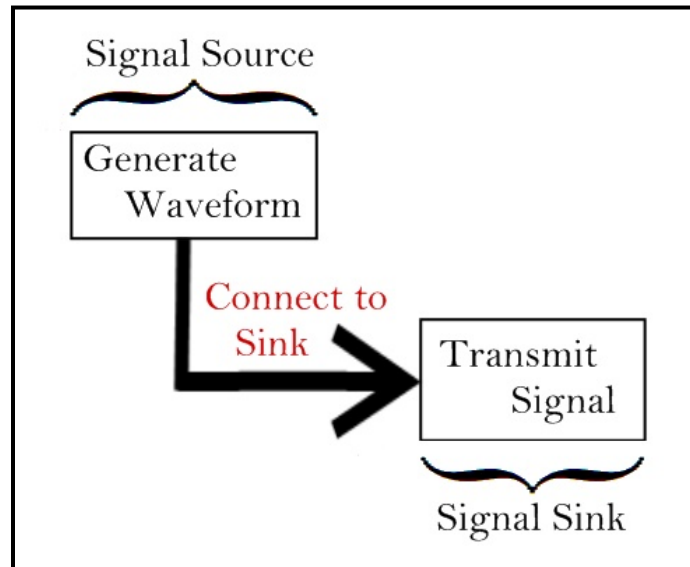


Figure 5: The flowgraph that shows the format of the program meant to transmit the desired range of frequencies is shown above. These details are encapsulated within the initialization section of the parent class, which rests on the above framework.

SUMMARY

The GNU Radio project was designed to process signals in the digital domain, and a solid, capable software structure exists to implement the ionosonde's receiver section. Due to limitations discovered during the course of this project, it does not appear practical—and quite probably not possible—to implement both transmit and receive modules on the same motherboard. However, the use of a second motherboard to isolate transmit and receive modules is justified due to a negligible increase in cost, which would remain a small fraction of a conventional ionosonde's cost. Additional risks in design, such as synchronization of the independent motherboards, could be mitigated through the use of additional hardware.

ACKNOWLEDGEMENTS

This material is based upon work supported by the National Science Foundation under Grant No. EEC-0755081.

REFERENCES:

- ¹ B.W. Reinisch, "Tenth International Digisonde Training Seminar at UMass Lowell Reviews State of Real-Time Mapping of the Ionosphere," *IEEE Antennas and Propagation Magazine*, **46** (5), 110-7 (2004).
- ² E. Blossom, "GNU radio: tools for exploring the radio frequency spectrum," *Linux Journal*, **2004** (122), 4 (2004).
- ³ "FPGA." GNU Radio: the gnu software radio [Online]. Available: <http://gnuradio.org/trac/wiki/UsrpFAQ/Intro/FPGA>.
- ⁴ G.H. Bary, "A Low-Power Vertical-Incidence Ionosonde," *IEEE Transactions on Geoscience Electronics*, **9** (2), 86-9 (1971).
- ⁵ H. Rishbeth and C.J. Davis, "The 70th anniversary of ionospheric sounding," *Engineering Science and Education Journal*, **10** (4), 139-44 (2001).
- ⁶ J.H. Reed, *Software Radio A Modern Approach to Radio Engineering*, Prentice Hall Communications Engineering and Emerging Technologies Series, 2002.
- ⁷ J.W. Wright, "Some Current Developments in Radio Systems for Sounding Ionospheric Structure and Motions" *Proceedings of the IEEE*, **57** (4), 481-6 (1969).
- ⁸ M.D. Silvius, F. Ge, A. Young, A.B. MacKenzie, and C.W. Bostian, "Smart Radio: Spectrum Access for First Responders," *Proc. of SPIE*, **6980**, 1-12 (2008).
- ⁹ Mitola J. III *Software Radio Architecture: Object Oriented Approaches to Wireless Systems Engineering*, John Wiley and Sons Inc., 2000.
- ¹⁰ R. Dhar, G. George, A. Malani, and P. Steenkiste, "Supporting Integrated MAC and PHY Software Development for the USRP SDR," *Networking Technologies for Software Defined Radio Networks*, 68-77 (2004).
- ¹¹ R. Miller, W. Xu, P. Kamat, and W. Trappe, "Service Discovery and Device Identification in Cognitive Radio Networks," *Networking Technologies for Software Defined Radio Networks, 2007 2nd IEEE Workshop*, 40-47 (2007).
- ¹² S. Zhang and J.M. Holt, "Climatology and Variability of the Ionosphere: Incoherent Scatter Radar Observations," *Radio Sounding and Plasma Physics*, 71-80 (2008).
- ¹³ T. Schmid, O. Sekkat, and M.B. Srivastava, "An Experimental Study of Network Performance Impact of Increased Latency in Software Defined Radios," *International Conference on Mobile Computing and Networking: Proceedings of the Second ACM International workshop on wireless testbeds, experimental evaluation and characterization*, 59-66 (2007).
- ¹⁴ "TX and RX Daughterboards For the USRP Software Radio System." Ettus Research LLC [Online]. Available: <http://www.ettus.com/custom.html>.

CIRCUIT DESIGN FOR NITTANYSAT SOLAR SENSOR

Daniel J. Schuette^{*}, Adam C. Escobar⁺, and Sven G. Bilén[#]

Department of Electrical Engineering
The Pennsylvania State University, University Park, PA 16802

^{*}Daniel J. Schuette student of
Department of Electrical Engineering
The Pennsylvania State University
University Park, PA 16802

ABSTRACT

This paper discusses the design of a solar sensor subsystem for NittanySat, a small satellite being designed by the Student Space Programs Laboratory. The solar sensor system will provide for the orientation of the satellite, in conjunction with other measurements. The Cadence software package will be used to design the circuit and make corresponding board layouts of the system.

INTRODUCTION

The purpose of my experiment was to design a solar sensor subsystem for the NittanySat satellite project run by the Student Space Programs Laboratory. The NittanySat project plans to launch a fully operational satellite into orbit. The satellite will measure amplitude and variability of radio wave absorption at very high frequencies, as well as the amplitude and locations of radio wave scintillations. Also, a correlation will be made to these scintillations to the amount of local plasma and plasma flux. Finally, the satellite will allow for the calibration of high latitude ground-based imaging riometers, devices that measure the amount of ionospheric absorption in the atmosphere.

⁺ Graduate mentor

[#] Faculty mentor

In order to facilitate an operational GNC (guidance, navigation, and control) system, a solar sensor must be in place to determine the attitude, or angle of the satellite with respect to a reference point, in this case the Sun. The principal component used is the Hamamatsu S3932 solar sensor, shown in figure 1.



Figure 1: Solar Sensor

The device is a 1-by-12 mm 1-dimensional device that detects the location of incident sunlight on itself, and then outputs 2 currents. These 2 currents, i_1 and i_2 , have a property that the value $(i_1 - i_2)/(i_1 + i_2)$ is proportional to the displacement of the incident light on the sensor. This value is actually proportional to the tangent of θ , the perpendicular distance from the sensor to the top of the orthogonal slit, over the displacement of the incident light from the endpoint of the sensor's active area. In this way, a vector can be determined that represents the direction of the sun from the satellite's reference plane.

In this implementation, the sensor's output currents will be scaled to a 0 – 5-V range, which is compatible with the satellite's sensor board system. These voltages are then sent to C&DH (command and data handling) to determine the orientation of the satellite in conjunction with other measurements, such as the magnetometer and GPS (global positioning system) receiver. NittanySat will have 2 orthogonal solar sensors on each face of the satellite, meaning that there will be 12 sensors total to determine the satellite's attitude, no matter which side of the satellite is facing the sun at any given instance. The solar sensors will provide the second vector needed for the TRIAD attitude determination method.

EXPERIMENTAL DESCRIPTION

Several different programs were used in the design of the solar sensor subsystem. Allegro Design Entry CIS version 16.01 was used to design the initial schematic for the circuit. Here, all components were placed, and the connections were wired. OrCAD Layout Plus version 15.7.0 was used to perform the layout and routing of the signal conditioning board.

The design began by placing the appropriate components needed to for the system. The output currents from the S3932 sensor need to be converted into voltages and then scaled to fit in the 0 – 5-V range compatible with the data processing components. The V_{cc} voltage of 5V was first sent through a voltage divider to obtain a 2.5-V value. This is then inputted into an LTC1047 op-amp to scale the input current to the appropriate range. The design depicts a single sensor’s conditioning circuit, and 12 of these identical designs are to be incorporated into the satellite altogether. For one sensor, the list of materials is provided in table 1.

Table 1: Materials Used

Components	Quantity
1.35"-by-1.35" routing board	1
Hamamatsu S3932 solar sensor	1
LTC1047 operational amplifier	1
4×1 header	1
24.9-kΩ resistors 0.1 %	2
1.0-μF Kemet T491A105M020AT capacitor	1
0.1-μF ceramic capacitors	2

Once the design was finished in Design Entry CIS, the layout was then made. All components were to fit on a 1.35"-by-1.35" routing board, with the size defined by a provided structural layout of the board, and several constraints regarding the placement of parts had to be adhered to. The sensor had to be centered on one side of the board, and all other components were placed on the other side. Routing was then performed to place the connections between all components on the board.

RESULTS AND DISCUSSION

The solar sensor’s board was successfully completed in capture and layout. The schematic in capture, shown below as figure 1, was modified several times in order to improve the operation of the circuit.

Unnecessary components originally included were removed in order to provide for a simple circuit that would fit on a PCB 1.35" by 1.35" in size. The layout for the board is also shown below as figure 2. It has been routed and finished, and is ready for machining.

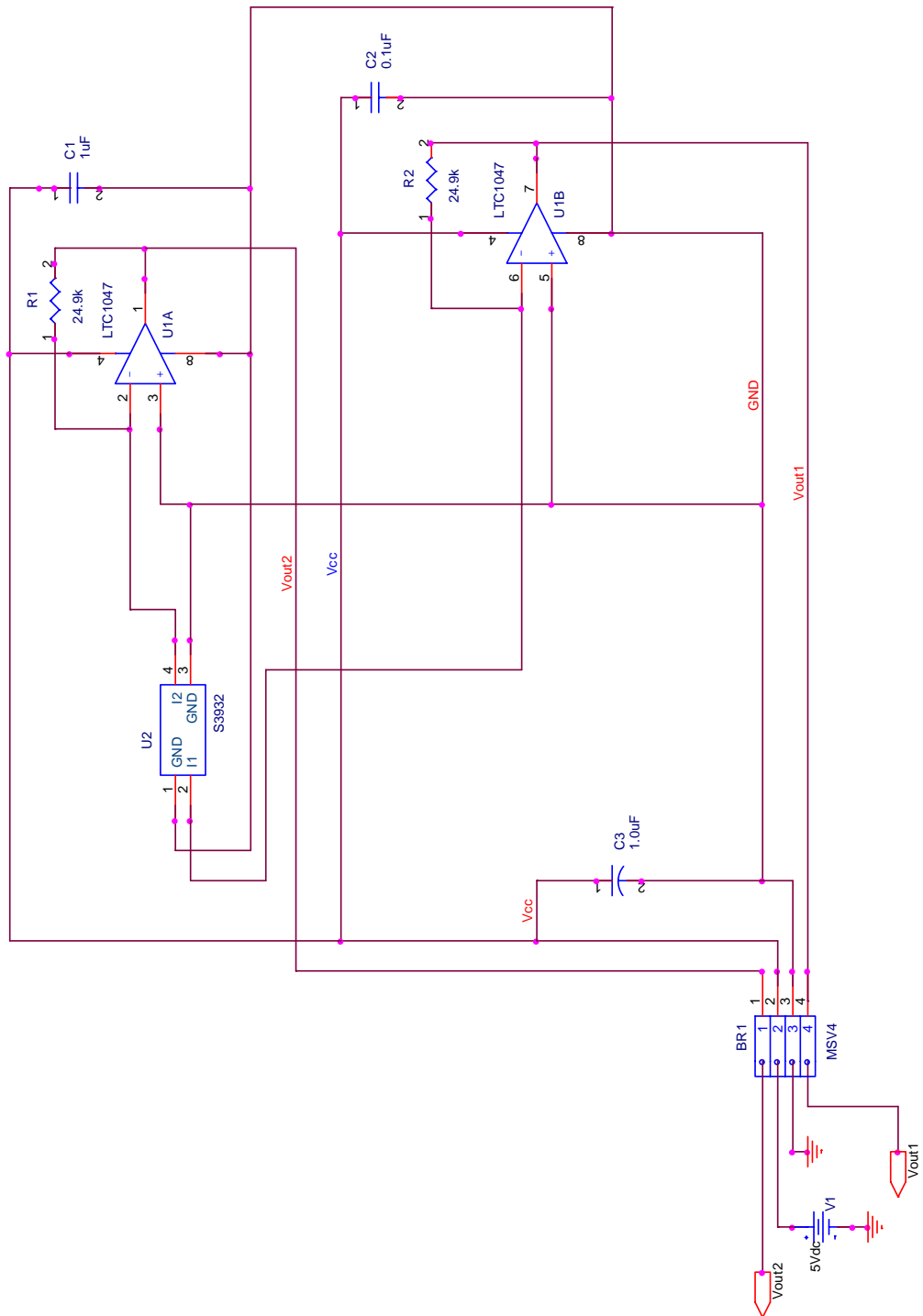


Figure 1: Schematic

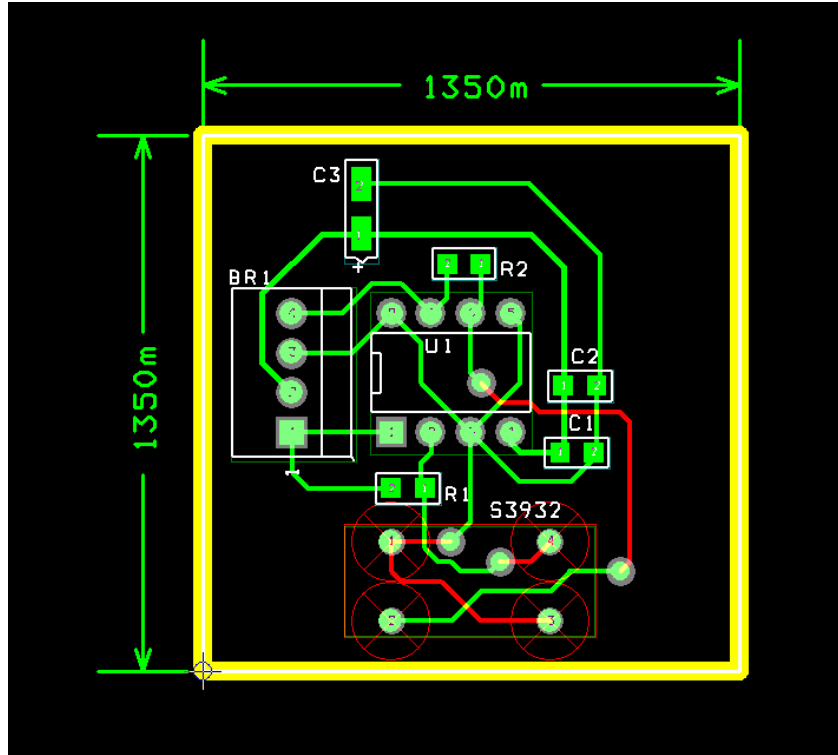


Figure 2: Layout

Many factors had to be taken into consideration before and during the designing process. Bypass capacitors were added to the schematic in order to decouple the effects the high power parts of the board would have on the rest of the circuit. When the layout was performed, the placement of the parts had to be looked at in order to maximize the performance of the board. The wires carrying the high current, which were those with the input 5 V, had to be kept short by ensuring that components that needed power were kept close together. Also, the wiring for these high current lines was made thicker than the rest to ensure that the current density (current/area) was kept small. The board layout also had the constraint that it had to fit specifications already determined, such as placement of the parts on the board, and what side the components would be on. It was these constraints that stipulated that the solar sensor had to be on the bottom of the board, while other components were to be paced along the top. Also, the sensor and the 8-pin operational amplifier were to be centered on the board in one orientation. The tantalum capacitor was to be left aligned with the sensor. Here, the “left” side is defined as the side containing the 4 pin Winchester connector. The rest of the surface mount pieces, including the resistors and other 2

capacitors, were free to be placed where they would work best. Other techniques were used that are standard for good routing practice. Corners made while routing connections were mitered, and not left at 90°. This was to ensure that there will not be a noticeable electromagnetic interference effect on the board.

Several improvements could be made to this design in the future. The layout could be optimized to allow for less routing, and the components could be relocated if more parameters become realized, such as clearance heights becoming defined for specific sections of the board. The design is simple enough that it can be modified easily.

SUMMARY

The design was successful in that it satisfied the original expectations for the system in delivering a very specific signal to the data processor. While similar systems have been made in the past, this circuit will help in the operation of the NittanySat satellite's solar sensors. This design has an impact in both the Navigation and Science subsystems, in determining orientation, which is needed to process data received by the plasma probe.

ACKNOWLEDGEMENT

One of the authors (DJS) would like to thank the Penn State EE REU program for the opportunity to conduct this research. Thanks are due to Dr. Sven Bilén for allowing DJS to work in his lab for the summer, and to Adam Escobar for his help and guidance.

This material is based upon work supported by the National Science Foundation under Grant No. EEC-0755081.

REFERENCES

- ¹ K. L. Kaiser, "Circuit Board Layout for EMC"; pp. 29-1–29-37 in *Electromagnetic Compatibility Handbook*. CRC Press, Boca Raton, 2005.
- ² J. L. Junkins, "Laser scanning graphic input system," U.S. Pat. No. 5 525 764, Jun. 11, 1996.
- ³ Sven Bilén, Adam Escobar, and Matt Sunderland, "Critical Design Review University NanoSat-5 Program," April 10, 2008.

INVENTORY AND MODEL BASED METHODS FOR TEXT TO SPEECH SYNTHESIS

Alexander Harrison*, Kenneth Jenkins[#], and Robert Nickel[#]

Department of Electrical Engineering
The Pennsylvania State University, University Park, PA 16802

*Undergraduate student of
Department of Electrical Engineering
Lehigh University
Bethlehem, PA 18015

ABSTRACT

This project involved working on different methods to create a text to speech voice synthesizer. There are multiple ways to approach making a speech synthesizer. This project looks at the two main methods used today to synthesize text to speech. The first method is the inventory based model where you have an archive of prerecorded sounds and assemble the word by stitching together these small snippets of recorded speech. The second method is called the model based approach which is much more math heavy and processor intensive but results in much higher compression and still results in a satisfactory sounding output speech. In this project the pros and cons of each method are compared while trying to achieve the most natural sounding voice synthesis.

INTRODUCTION

The topic of speech synthesis is very important to certain industries and fields of science. Speech synthesis has been studied for decades but is still intensively researched to continue making it sound more lifelike. The ultimate goal would be where a person could talk on the phone with a computer using speech synthesis and they would not be able to tell the person on the other line isn't real. We are not at this stage but we are working to get closer. The best way to reproduce nature is to fully understand what is happening when we speak and accurately reproduce it.

[#] Faculty co-mentors

Simplified Model

Speech occurs when our vocal chords create a series of excitation pulses that are heard as sound. The initial pulses are then modified by the vocal tract. The air is moved through our mouth and lips, causing turbulence in the airflow which filters the initial uniform pulses into the different sounds we can make from our mouths. Due to this, speech can be modeled by the response of a linear time varying system. The output waveform is just the convolution of an impulse train with the period T caused by the vocal chord and the vocal tract filter as shown in figure 1^[1].

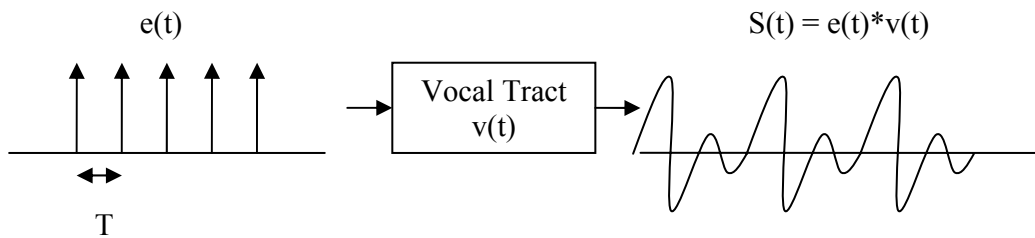


Figure 1. Simple model of vocal tract filter

In this manner, speech is expressed as a z transform that is generally passed through three linear filters. These are the excitation filter ($E(z)$), the vocal tract filter ($V(z)$) and the radiation filter ($R(z)$). The excitation filter determines whether the process starts with an impulse train or a white noise sequence. The vocal tract filter represents the spectral shaping that is made with throat and mouths. The radiation filter is meant to represent the shape the lips make when a word is spoken. So the output waveform can be represented by the equation below^[2].

$$S(z) = E(z)V(z)R(z) \quad (1)$$

For this experiment the vocal tract filter and the radiation filter will be combined.

Phonemes

When a person speaks, they are speaking a large amount of basic sounds combined together to make full words. These basic building blocks of each language are called phonemes. In the English language, there are 41 of these phonemes. Different languages possess different phonemes due to the way they pronounce different words. These can be either voiced or unvoiced. A voiced phoneme is a phoneme where the original sound is caused by vibrations of the vocal chords which are then manipulated by the vocal tract. An unvoiced phoneme is a phoneme where the sound is caused only by the turbulence of air

through the vocal tract without vibrations from the vocal chords. In this case the $E(z)$ would be represented by white noise instead of a clean impulse train.

Linear Predictive Coding

The linear predictive model is a method of using samples of past inputs and outputs and the current input to predict the current output^[3]. The LP model is a recursive method of estimating values until the estimates are within the minimal margin of error. The all-pole model using block processing was used in this project. This method creates a vector of variables a_k . These variables can be used as a filter when applied to previous inputs and the current input to determine the output.

$$y_n = x_n + \sum_{k=1}^K a_k y_{n-k} \quad (2)$$

The equation above shows the basic formula of a linear predictive function. In this equation, y is the output, x is the input, \mathbf{a} is a vector of linear predictive coefficients a_k , and K is the number of the predictive coefficients. The signal y represents the actual series of sound impulses generated from each phoneme. This will be elaborated upon in the model based approach below. Two new matrices \mathbf{y} and \mathbf{Y} are created from this input vector defined as

$$\mathbf{y} = \begin{bmatrix} y_1 \\ y_2 \\ \vdots \\ y_{N-1} \\ y_N \\ 0 \\ \vdots \\ 0 \end{bmatrix} \quad \mathbf{Y} = \begin{bmatrix} 0 & 0 & \cdots & 0 \\ y_1 & 0 & \ddots & \vdots \\ y_2 & y_1 & \ddots & 0 \\ \vdots & y_2 & \ddots & 0 \\ y_N & \ddots & \ddots & y_1 \\ 0 & y_N & \ddots & y_2 \\ \vdots & \ddots & \ddots & \vdots \\ 0 & \cdots & 0 & y_N \end{bmatrix}$$

Once these parameters are defined the next step is to substitute them back into the original LP equation (2). Since we are minimizing error and maximizing input excitation, we set the input x to zero. If \mathbf{Y} was a square matrix in our example, it can be assumed that equation (3) would be true.

$$\mathbf{x} = \begin{bmatrix} x_1 \\ x_2 \\ x_3 \\ \vdots \\ x_N \end{bmatrix} \quad \mathbf{a} = \begin{bmatrix} a_1 \\ a_2 \\ a_3 \\ \vdots \\ a_K \end{bmatrix}$$

$$\mathbf{x} = \mathbf{y} - \mathbf{a}^T \mathbf{Y}$$

$$0 \approx \mathbf{y} - \mathbf{a}^T \mathbf{Y}$$

$$\mathbf{y} \approx \mathbf{a}^T \mathbf{Y}$$

$$\mathbf{a} \approx \mathbf{Y}^{-1} \mathbf{y} \tag{3}$$

$$\mathbf{a} \approx (\mathbf{Y}^T \mathbf{Y})^{-1} \mathbf{Y}^T \mathbf{y} \tag{4}$$

Since the inverse of \mathbf{Y} is not defined, the pseudoinverse of \mathbf{Y} is used equation (3), resulting in equation (4)^[4]. Now in order to reconstruct the voice signal the original excitation signal must be run through the filter with these coefficients.

METHODS

There are two main methods in this project used to reconstruct speech. These are the inventory based approach to speech synthesis and the model based approach. First we will be looking at the inventory based approach.

Inventory Based Approach

This approach deals with stitching together sound files to make natural sounding words. The source audio files come from other projects. The arctic database was used in this project using only one of the speakers in the database. This database consists of around 1000 audio files. Each file contains a speaker reading one sentence. The wave files had been segmented with markers denoting the beginning and end of each phoneme said in each wave file. Since wave files are already sampled, we can think of each wave file as a list of impulses T length apart with differing amplitudes. The database used for this project was the arctic database sampled at 16000 Hz making the T between each impulse response equal to $6.25 * 10^{-5}$ seconds.

The first thing needed for the project to move forward was a database of each spoken phoneme to be pulled out when needed. To accomplish this a program was created that scans through each wave file. When it finds a phoneme not in the database, it adds it after looking at the starting and ending location of the phoneme in the file. This program scans through all the files providing a small snippet of sound for every phoneme in the English language. Next, a program was written where a string of sounds is entered into Matlab, and the

program fetches the sound snippets and puts them into a new array of impulse excitations representing the reconstructed word. Figure 2 shows the result of concatenating the phonemes.

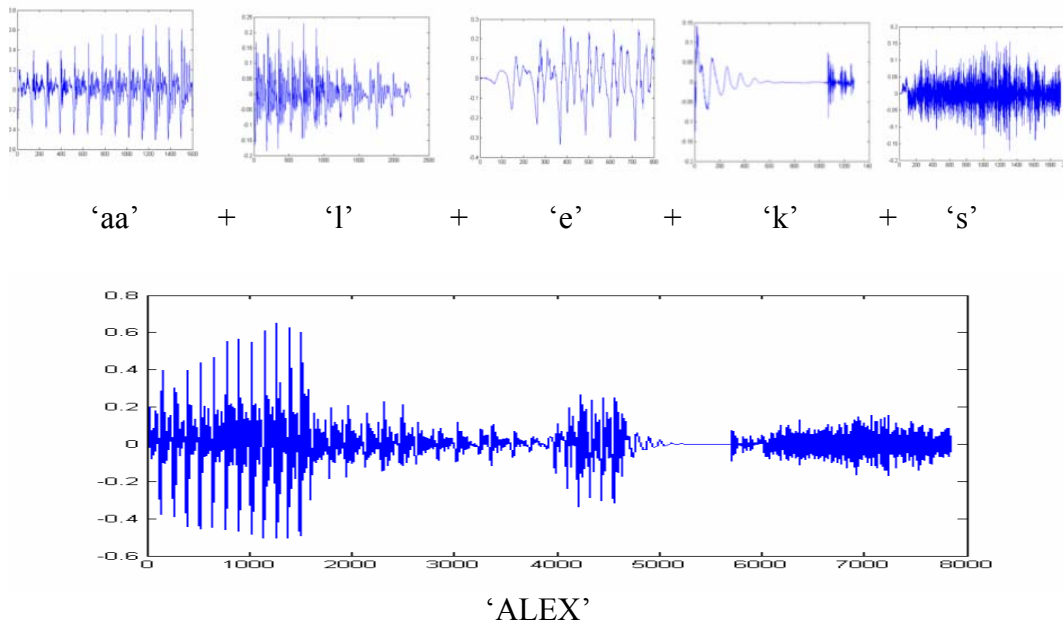


Figure 2. Concatenation of phonemes to construct a word

Boundary Smoothing

This method works very well but it creates discontinuities between each sound in the word that sounds like a pop and decreases the smoothness of the generated waveform. What is needed to smooth these boundaries and prevent discontinuities is to locate these boundaries and average them out for a certain specified amount of time. This is done by applying the following equations.

$$\text{Left Boundary } y_{1av} = (-(1/T)*x + 1) * y_1 \quad (5)$$

$$\text{Right Boundary } y_{2av} = x/T * y_2 \quad (6)$$

$$\text{Smoothed Boundary} = y_{1av} + y_{2av} \quad (7)$$

Here, T is the overlap time, x is each point in the array, and y_1 and y_2 are the original functions. The left boundary gradually decreases as it goes to the right and the right boundary gradually decreases as it goes to the left until they meet at the center. At the center, the amplitude is the sum of 50% from each.

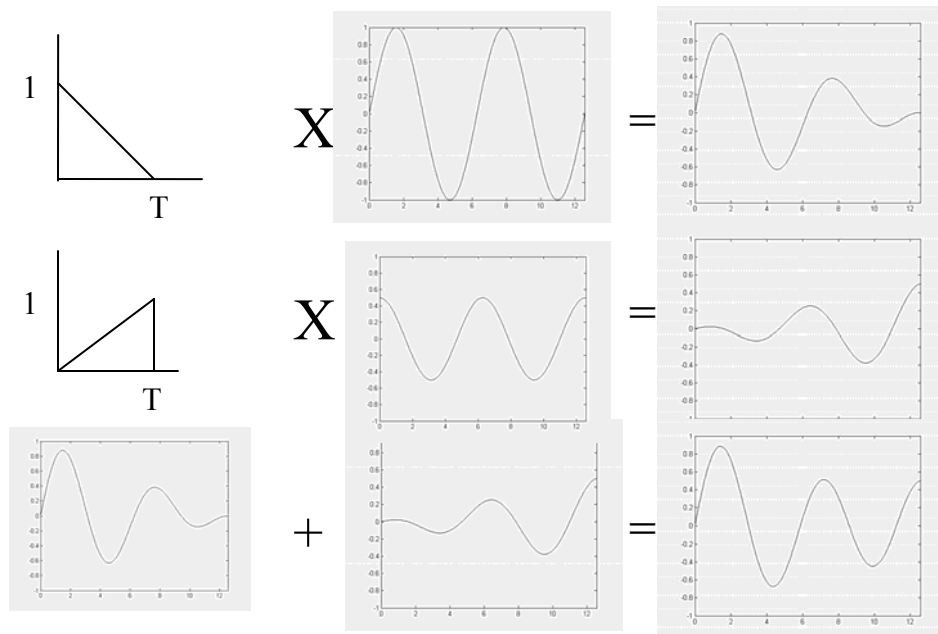


Figure 3. Example of border selection being smoothed out

Model Based Approach

The model based approach to voice synthesis is different from the inventory based approach in that the process does not store the actual sound files from the phoneme list but rather stores a compressed form of the data, and decompresses it later. The first step in synthesizing speech using this method is to take the table of phonemes that were acquired earlier in this project and discovering which of them are voiced and which of them are unvoiced, meaning which are created when the vocal chord is vibrating. Once these are separated into two groups, the linear predictive coding can be run on each of the phonemes and the coefficients a_k are stored. Now there are only k data values stored in order to reproduce each phoneme as opposed to the inventory approach which requires anywhere from six hundred to over two-thousand pieces of data to accurately reproduce the original sound.

Voiced Vs. Unvoiced

Once the values of the LP coefficients are stored in the computer, reproducing them requires knowledge of whether they are voiced or unvoiced. For voiced phonemes, the input signal is a uniform impulse train each of value 1. To generate an unvoiced signal, the input must be an impulse train but each having Gaussian random amplitudes in order to retrieve an accurate representation of the original signal. After the original phoneme is regenerated using this method, it is run through the program used earlier that can concatenate the phonemes into words which it would then speak. This process is illustrated in figure (4).

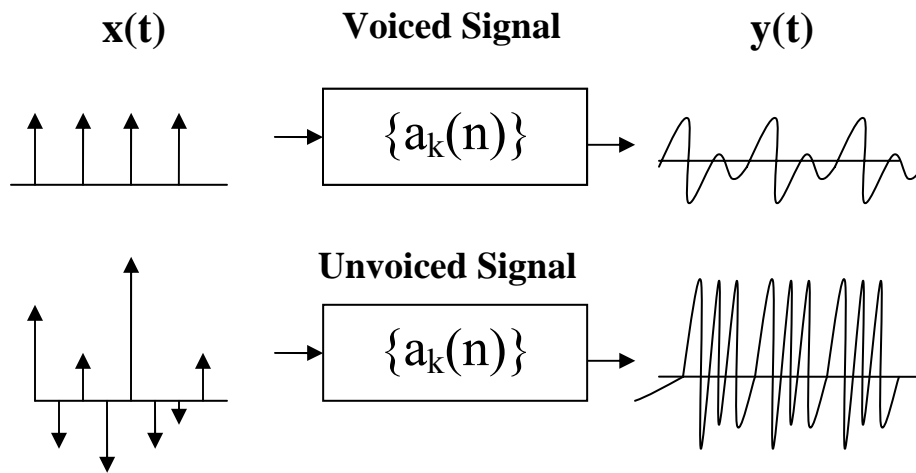


Figure 4. Illustration of model based speech

RESULTS

This project was created to test the feasibility and accuracy of different text to speech techniques. Using only the inventory method, there were major discontinuities while concatenating the words. This was solved by the border technique that smoothed those discontinuities. At a sampling rate of 16 KHz, an 80 sample overlap would be 5ms, 160 samples would be 10ms, and a 240 sample overlap would take 15 ms. Through trial and error, the best overlap time seemed to be around 10 ms but it is subjective and depends on the word being produced. The inventory method was fast but not very efficient. It required a large amount of stored data. Another method would be using only phonemes that had matched up in the original recordings, further smoothing out the transitions between the sounds generated. If this method were to be used on this project, the amount of stored data would have been enormous if the catalog had a version of every phoneme that had been attached to every other phoneme.

The model based approach fixes the file size problem raised by the inventory approach, though it does have its limitations as well. It takes a relatively large amount of time and processing power to encode and decode every phoneme each time you need to use it. It would be unfeasible to use them in any kind of real time application.

The difference in file size of the stored phonemes is very different between the two methods. The inventory approach has 68640 samples stored in the database. The model based method is only $41 * k$ stored samples where $k = 15$.

Even with a relatively high number of LP coefficients, the model approach only has 615 samples stored. This is an impressive 99.1% compression.

ACKNOWLEDGEMENT

One of the authors (AH) would like to thank Dr. Kenneth Jenkins, Dr. Ruyan Guo, and Mrs. Mary Ann Henderson for accepting him into this program. AH would also like to thank Dr. Kenneth Jenkins and Dr. Robert Nickel for personally helping him through the research of this project.

This material is based upon work supported by the National Science Foundation under Grant No. EEC-0755081.

REFERENCES

- [1] A. Oppenheim, Ch.3 Digital Processing of Speech,117-128, *Applications of Digital Signal Processing*, A. Oppenheim, Prentice-Hall Inc., Englewood Cliffs, NJ, 1978.
- [2] D. O'Shaughnessy, "Modern methods of speech synthesis," *IEEE Circuits and Systems Magazine*, **10**(1109), 6-23 (2007).
- [3] J. Makhoul, "Linear Prediction: A Tutorial Review," *Proceedings of the IEEE*, **63**(4), 561-580, (1975).
- [4] M. Steiner, "Pitch Shifting of a Speech Signal By Source-Filter Processing," *NSF EE REU PENN STATE Annual Research Journal*, **5**, 161-169, (2007).

SOLVING THE MYSTERY OF LONG DURATION METEOR TRAILS

Kimberly L. Ray*, Akshay Malhotra⁺, and John D. Mathews[#]

Department of Electrical Engineering
The Pennsylvania State University
University Park, PA 16801

*Undergraduate student of
Department of Physics
Texas Lutheran University
Seguin, TX 78155

ABSTRACT

The Jicamarca Radio Observatory (JRO) in Lima, Peru has one of the most useful radars in the world for the study of the equatorial ionosphere. This is because the JRO lies at the geomagnetic equator.

As meteors travel across geomagnetic field lines, electrons given off by the meteors align along the field lines resulting in strong radar returns recognized as Range Spread Trail Echoes (RSTE) [Malhotra *et al.*, 2007a]. RSTEs can last from less than a second to over 15 minutes. A modern explanation of these long-duration meteor echoes has remained elusive and thus remains a subject of much speculation [Malhotra *et al.*, 2007a]. When observing RSTEs, it is important to consider viewing geometry. That is to say, two identical, closely spaced radars would observe the same RSTE event differently; one may see a short-duration-event only while the other radar may see a long-duration event depending on the viewing geometry [Malhotra *et al.*, 2007a]. Further analysis of these long-duration meteor echoes must be conducted to reveal the mystery behind long-lasting RSTEs.

Using data collected in August 2007 on long-duration meteor trails (trails greater than 15s) from the JRO, we examine RSTEs involving the use of interferometric analysis. Other areas of interest include examining meteoroid mass and energy of long-lasting RSTEs.

⁺ Graduate Mentor

[#] Faculty Mentor

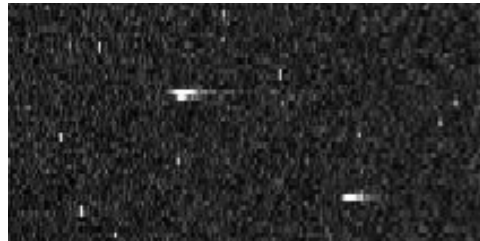
INTRODUCTION

A meteoroid, more commonly referred to as “shooting stars”, is defined as small mass of debris in the solar system. The Earth is constantly being bombarded with these meteors that can be observed by sensitive radars. Once a meteoroid enters the Earth’s atmosphere, it comes to be known as a meteor.

As a meteoroid enters the Earth’s atmosphere, a trail of ionization is formed. The incoming meteoroid ionizes molecules in the upper atmosphere (80km-120km) leaving a plasma trail, referred to as a meteor echo, when viewed by radar. Meteor echoes can be classified into three categories (Figure 1): head echo, specular or classical trail, and Range Spread Trail Echoes (RSTE) or non-specular trail. A head echo is the scattering from the plasma surrounding the meteoroid. A classical/specular trail echo is observed when the trail lies perpendicular to the radar beam. And a RSTE is observed in areas where the radar points perpendicular to the geomagnetic field.



(a) Head Echo



(b) Specular/Classical
trail echo



(c) Range Spread
Trail Echo

Figure 1. Images from MU radar located in Japan

As meteoroids travel across geomagnetic field lines, electrons given off by the meteors align along the field lines due to high conductivity along the field lines resulting in strong radar returns distributed in range, hence known as RSTE. A comprehensive explanation of the formation and evolution of these RSTEs has remained elusive and thus remains a matter of much speculation [Bourdillon *et al.*, 2005; Chapin and Kudeki, 1994; Dyrud *et al.*, 2005; Kelly 2004; Mathews, 2004; Malhotra *et al.*, 2007a,b].

Mostly RSTEs last for less than a second to 5 seconds in duration. But a few are observed to last for well over 15 seconds, even up to 15 minutes. RSTEs lasting greater than 15 seconds are classified as long duration RSTEs [Malhotra *et al.*, 2007a]. These long duration meteor echoes are still not well explained and remain a subject of study for the past 60 years.

When observing RSTEs, it is important to consider the viewing geometry. Trails become highly aspect sensitive as they align along \mathbf{B} and after a while can only be observed if the radar points perpendicular to the magnetic field. It is hypothesized that full understanding of RSTEs must involve knowledge of the trail-viewing angle relative to $\mathbf{k}\perp\mathbf{B}$ [Malhotra *et al.*, 2007a]. That is to say, two identical, closely spaced radars would observe the same RSTE event differently as shown in Figure 2. The first radar (Radar 1) will observe a long duration event as the event lies in the $\mathbf{k}\perp\mathbf{B}$ region of the first radar while the second radar (Radar 2) will observe the same meteor event as a short duration as it lies away from the $\mathbf{k}\perp\mathbf{B}$ region of the second radar [Malhotra *et al.*, 2007b]. It has also been observed that most head echoes viewed in the $\mathbf{k}\perp\mathbf{B}$ region are followed by RSTEs. Other observations include that almost all long duration RSTEs originate from the $\mathbf{k}\perp\mathbf{B}$ region.

Radar interferometry is used in this analysis of RSTEs. Interferometric analysis is a technique used at Jicamarca when analyzing meteor trails. This method allows us to ascertain the exact position of meteors in the ionosphere.

Interferometric methods use the entire Jicamarca radar array (Figure 3). A pulsed signal is transmitted from the north and south quarters of the array (Figure 4). Three antenna modules, 36 meters apart, receive the signals in the East quarter of the Jicamarca radar array for data collection (Figure 4). These received signals are then Fourier-transformed and their relative phase shifts to each other allow the exact location of the RSTE to be determined.

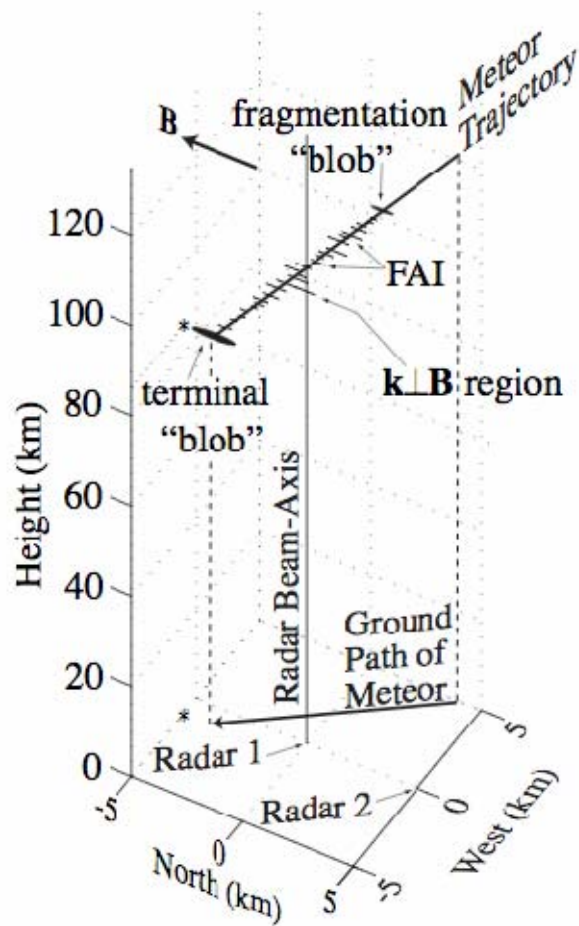


Figure 2. An RSTE occurring at the $k_{\perp}B$ region of Radar 1 can be seen as a long duration event from Radar 1 as it lies in the $k_{\perp}B$ region of this radar and a short duration event from Radar 2 as it lies away from the $k_{\perp}B$ region of Radar 2 [Malhotra *et al.*, 2007b]



Figure 3. An image of the Jicamarca Radio Observatory in Lima, Peru

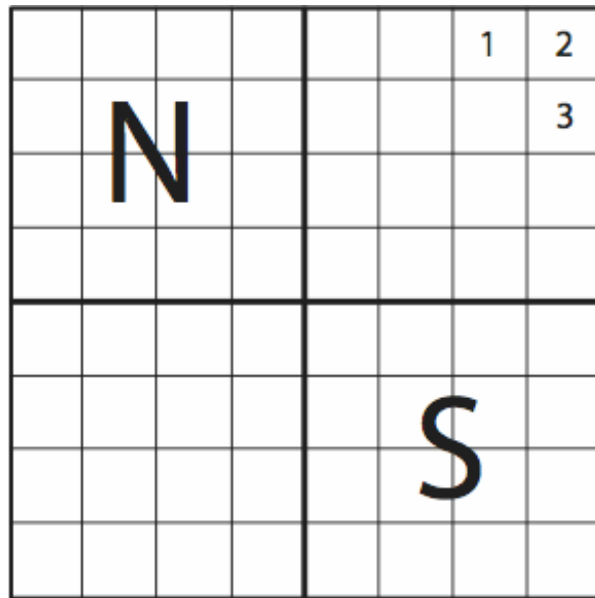


Figure 4. A sketch of the Jicamarca array where N represents the North quarter, S represents the South quarter, and 1, 2, and 3 represent the three modules used to receive signal.

OBSERVATIONAL SETUP

The Jicamarca Radio Observatory (JRO) in Lima, Peru has one of the most useful radars in the world for the study of the equatorial ionosphere. This is because the JRO lies at the geomagnetic equator thus enabling the radar's line of sight to be perpendicular to the Earth's magnetic field when pointing vertical to the Earth's surface.

The data used in the analysis was collected from the JRO on August 10, 2007 using the 50MHz radar. Both north and south quarters of the Jicamarca array were used for transmission. A 39 μ s 13 Baud Barker coded pulse was transmitted with an IPP (Inter Pulse Period) of 900 μ s (Table I). A more detailed description for the set up and data acquisition on August 10, 2007 is supplied in [Malhotra *et al.*, 2008].

Table I. Jicamarca 50 MHz Radar Parameters for the Meteor Observations of August 10, 2007

Parameter	Value	Units
Frequency	50	MHz
Interpulse Period	900	μ s
Pulse Width	5.85	Km
Barker Code	13	Baud
Sampling Rate	3	μ s
Initial Range	90	Km
Number of Samples	88	
Number of Channels used	3	
Transmitted Peak Power	2	MW

Using IDL, a programming language used for analyzing atmospheric and space physics data, each meteor event was examined separately and its location was determined to find out whether its path was along the **k \perp B** region of the radar. These meteor events were collected into a database for further investigation. It was the unique presence of the Equatorial Electrojet (EEJ) scattering that allowed the **k \perp B** region of the radar to be easily identified [Kudeki and Farley, 1989]. Other information collected about these meteors included their beginning time, time duration, and whether they had a head echo or not.

RESULTS AND DISCUSSION

Long duration RSTEs can be explained to a considerable degree from a radio science perspective, without the involvement of detailed plasma physics. It has already been established that all long duration meteor echoes come exactly

from the **kLB** region of the radar [Malhotra et al., 2007a]. Malhotra et al. [2007b] showed that two different, closely spaced radars observing a common volume would observe the same meteor event differently. The same meteor would be observed as a long duration event from one of the radars if it lies in the **kLB** region of this radar and as a short duration event from another radar for which it lies away from its **kLB** region. This underlines the importance of viewing geometry while performing any analysis which involves the duration of RSTEs. Thus, this study focuses only on meteor echoes in the **kLB** region of the radar. All meteors outside of the **kLB** region of the radar were not considered for analysis because we could not be certain of their exact time duration as a result of “incorrect” viewing geometry.

An interferometric analysis of all RSTEs in the **kLB** region was conducted on approximately 8 hrs of data taken on August 10, 2007. In this 8 hr data set, 1452 events were observed to be in the **kLB** region. Figure 5 shows the meteor trail duration with respect to the time the meteor occurred in the **kLB** region of the radar for all events recorded. As stated earlier, only meteor events occurring in the **kLB** region of the radar were considered. From Figure 5, we learn that more meteor events occur during the evening hours compared to the morning. We notice the longest lasting echoes occur earlier in the night.

A single, long-duration RSTE, representative of all long duration RSTE observed occurring in the 8 hr data set can be seen in Figure 6. In the RTI (Range-Time-Intensity) plot in Figure 6 we can see the intensity of the long duration RSTE at a certain time and range (altitude in this case since our radar is perpendicular to the magnetic field lines). We can see that the trail beginning at 7:17:05 is located at a~100 km altitude and is approximately 16 seconds long.

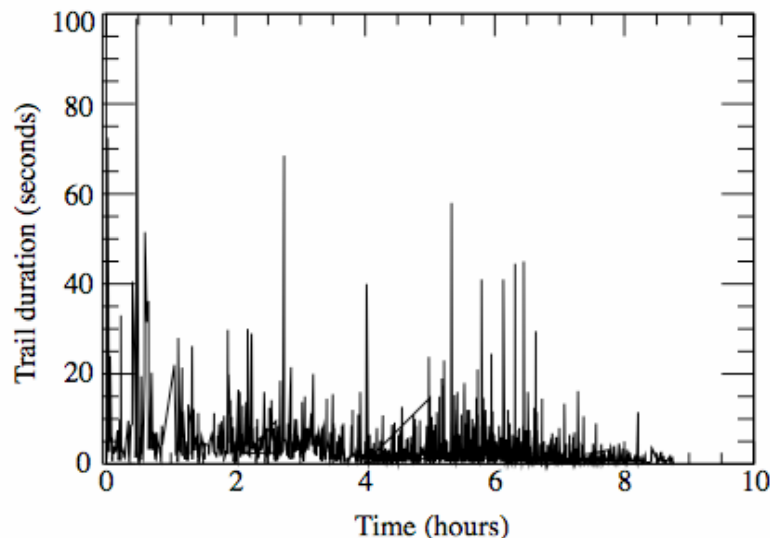


Figure 5. Plot showing the time of all the 1452 meteor trail events in the **kLB** region in approximately 8 hr data set at the JRO

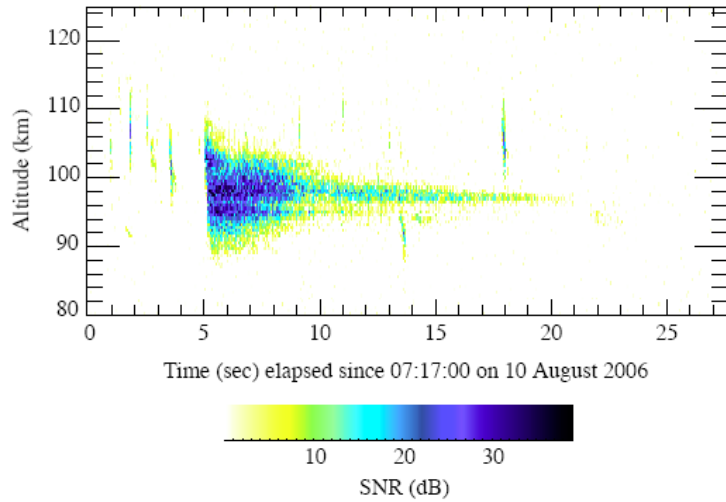


Figure 6. RTI (Range-Time-Intensity) plot of a long duration RSTE amongst multiple short duration meteor trail events at Jicamarca Radio Observatory. The meteor trail lasts for approximately 16 seconds

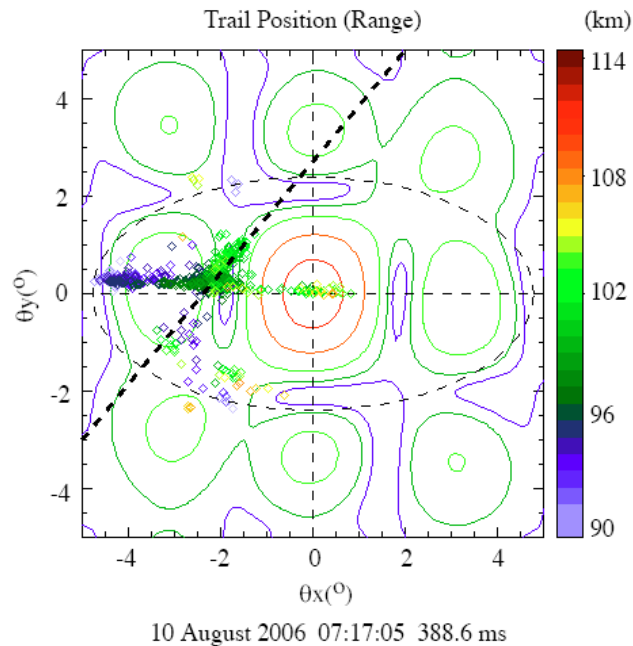


Figure 7. The trail position of a 16 seconds long-duration RSTE as it aligns along the magnetic field line

As previously stated, as meteoroids travel across geomagnetic field lines, electrons given off by the meteors align along the field lines due to high conductivity along the field lines. Figure 7 displays an interferometric plot of the same long duration meteor trail as in Figure 6 as it aligns along **B**. The straight dashed line in Figure 7 represents the location of the **k_LB** region for the Jicamarca radar. The dotted circle indicates the region in which unambiguous meteor position can be calculated, and has an approximate radius of 8.36 km at an altitude of ~100 km. In Figure 7, we are able to see the long duration meteor trail, seen previously in Figure 6, align along the **k_LB** region of the Jicamarca radar as it travels across the magnetic fields lines. The beginning of the RSTE (shown in blue) is seen to occur away from the **k_LB** region of the Jicamarca radar, and as the meteoroid travels across the magnetic field line, we can see the RSTE begin to align along the **k_LB** region of the Jicamarca radar.

CONCLUSION

Using data collected in August 2007 from the JRO, we have examined RSTEs using interferometric analysis. Only meteor trail events occurring in the **k_LB** region of the Jicamarca radar were considered to remove any ambiguity regarding the trail duration.

It has been confirmed that as meteoroids travel across geomagnetic field lines, electrons given off by the meteors align along the field lines as a result of high conductivity along the field lines. This increases the aspect sensitivity of the trail and after a while, the trail can be observed only along the **k_LB** region of the radar.

More investigations need to be carried out on the effect of RSTEs in the upper ionosphere. The exact role that meteors play in the ionosphere is still unknown to us and this could be used to interpret many yet unexplained phenomena. Future studies include the investigation of the effect of meteoroid mass and energy on the duration of RSTEs using the data collect during the course of this work.

ACKNOWLEDGEMENT

Thank you to Dr. Ruyan Guo and Dr. Kenneth Jenkins for organizing the 2008 Penn State Electrical Engineering Research Experience for Undergraduates program. One of the authors (KLR) would also like to thank Dorey Livneh for helping her understand the concept of “head echoes”.

This material is based upon work supported by the National Science Foundation under Grant No. EEC-0755081.

REFERENCES

Bourdillon, A., et al. (2005), Long duration meteor echoes characterized by Doppler spectrum bifurcation, *Geophys. Res. Lett.*, 32, L05805, doi:10.1029/2004GL021685

- Chapin, E., and E. Kudeki (1994a), Radar interferometric imaging studies of long-duration meteor echoes observed at Jicamarca, *J. Geophys. Res.*, 99(A5), 8937-8949
- Dyrud, L., et al. (2005), Modeling high-power large aperture radar meteor trails, *J. Atmos. Sol. Terr. Phys.*, 67, 1171-1177
- Kelley, M. C. (2004), A new explanation for long-duration meteor radar echoes: Persistent charged dust trails, *Radio Sci.*, 39, RS2015, doi:10.1029/2003RS002988
- Kudeki, E., and D. T. Farley (1989) , Aspect sensitivity of equatorial electrojet irregularities and theoretical implications, *J. Geophys. Res.*,94(A1), 426-434
- Malhotra, A., J.D.Mathews, and J. Urbina (2007a), A radio science perspective on long-duration meteor trails, *J. Geophys. Res.*, 112, A12303, doi:10.1029/2007JA012576
- Malhotra, A., J.D.Mathews, and J. Urbina (2007b), Multi-static, common volume radar observations of meteor at Jicamarca, *Geophys. Res. Lett.*, 34, L24103, doi:10.1029/2007GL032104
- Malhotra, A., J. D. Mathews, and J. Urbina (2008), Effect of meteor ionization on sporadic-E observed at Jicamarca, *Geophys. Res. Lett.*, doi:10.1029/2008GL034661, in press.
- Mathews, J. D. (2004), Radio Science issues surrounding HF/VHF/UHF radar meteor studies, *J. Atmos. Sol. Terr. Phys.*, 66, 285-299

MODELING OF REALISTIC THUNDER CLOUD CHARGE STRUCTURE AND APPLICATION TO SIMULATION OF LIGHTNING DISCHARGES

Samuel T. Poulos*, Jeremy A. Rioussel⁺, and Victor P. Pasko[#]

CSSL, Department of Electrical Engineering
The Pennsylvania State University, University Park, PA 16802

*Undergraduate student of
Department of Biomedical Engineering
The University of Texas at Austin, Austin, TX 78752

ABSTRACT

Numerical modeling of lightning discharge by various authors^[1-3] has established how fractal geometry can be successfully used to model the lightning channel. Rioussel *et al.*^[3]'s model combined the hypotheses of equipotentiality and over all neutrality of the discharge first proposed by Kasemir^[4] with the fractal approaches used in previous models^[1,2,5,6]. In Rioussel *et al.*^[3]'s work, charge regions in a thunder cloud were modeled as three distinct axisymmetric cylinders, each possessing a uniform charge throughout. The charge was then discretized onto a three dimensional Cartesian grid of points before the actual lightning discharge was simulated. The simulated lightning discharges were compared to lightning mapping observations made by the New Mexico Tech Lightning Mapping Array (LMA) during a thunderstorm on July 31, 1999. The objective of this research is to develop an algorithm assigning more realistic charge distributions to the grid points. In this paper we report modeling results in which charge is assigned to the grid points based on the frequency and location of observed source points in the LMA data. After assigning charges based on the data, the simulated lightning discharges are compared to actual events observed by the LMA. The presented modeling results on cloud-to-ground, intra cloud and upward (jettype) discharges allow more realistic studies of lightning propagation through pockets of charge inside of a thunder cloud and demonstrate a clear advantage of the developed modeling approach in comparison with previously employed uniform charge models^[3,7,8].

⁺ Graduate Mentor; [#] Faculty Mentor

INTRODUCTION

The earliest scientific studies about lightning were performed by Benjamin Franklin in the latter half of the eighteenth century^[9]. It was not until the invention of the streak camera by Boys in 1926 that subsequent advances in the field of lightning research were made possible^[10]. Using this camera to observe thunderstorms in South Africa, Schonland, Malan and co-workers determined that a plasma process, so called leader breakdown, was responsible for the initiation and propagation of discharge channels in cloud-to-ground lightning^[10]. The leader process was subsequently shown to be valid for intracloud discharges as well^[11], however the physics of the process itself is still poorly understood^[12].

The development of theoretical models of lightning discharges began around 1950^[4, 13, 14]. In 1960 Kasemir^[4] proposed that lightning discharges are both equipotential and overall neutral. These hypotheses were derived from photographic evidence that lightning discharges were plasma waves of predominantly leader nature^[15], i.e., highly conductive plasma channels.

The concern of lightning damage to aircraft^[16], spacecraft^[17], and electronic equipment^[10], as well as the increase in computational power over the past three decades all contributed and continue to drive lightning discharge research. However, due to the lack of a complete theory of lightning channel propagation, researchers have sometimes considered only the bulk effects of the discharge rather than the channel itself^[7, 18]. Benoit Mandelbrot suggested that many complex physical phenomena could be modeled with fractal geometry^[19, 20]. Niemeyer *et al.*^[5] then applied fractal approaches to the modeling of electrical breakdown and proposed their dielectric breakdown model, which could reproduce the gross characteristics of Lichtenberg figures produced by a streamer discharge in pressurized SF₆ gas. Although many variations of the dielectric breakdown model were employed for both streamer discharges^[6, 21, 22] and lightning leader channels^[1, 2], none of the proposed models ensured that Kasemir^[4]'s hypotheses were consistently satisfied. Therefore, Riousset *et al.*^[3] introduced a new three dimensional formulation of a stochastic lightning model which self-consistently accounted for the hypotheses of equipotentiality and neutrality.

Riousset *et al.*^[3] compared the results of their model to lightning mapping observations obtained from the Lightning Mapping Array (LMA) operating over Langmuir Laboratory, New Mexico, and data in the available refereed literature. In this work, Riousset *et al.*^[3] were able to both qualitatively and quantitatively validate the accuracy of their model. This model was further applied to the study of various discharges^[8] including bolt-from-the-blue^[23, 24], blue jets^[25, 26], and gigantic jets^[27, 28]. This work applies Riousset *et al.*^[3]'s model to cloud charge configurations that are based on the data collected by the LMA. After assigning charges based on the data, the simulated lightning discharges are compared to actual events observed by the LMA.

MODEL FORMULATION

The cloud and lightning discharge are modeled in a 3-D Cartesian domain, which is discretized in the three spatial dimensions using equidistant grid points. Charge is assigned to the grid points based on the location and frequency of events recorded by the LMA during a storm on July 31, 1999 (Figure 1). This method of charge assignment differs from other thundercloud models which employed the classical tripole model of thundercloud charge distribution^[29] using axisymmetric cylinders to model the charge layers^[7]. The

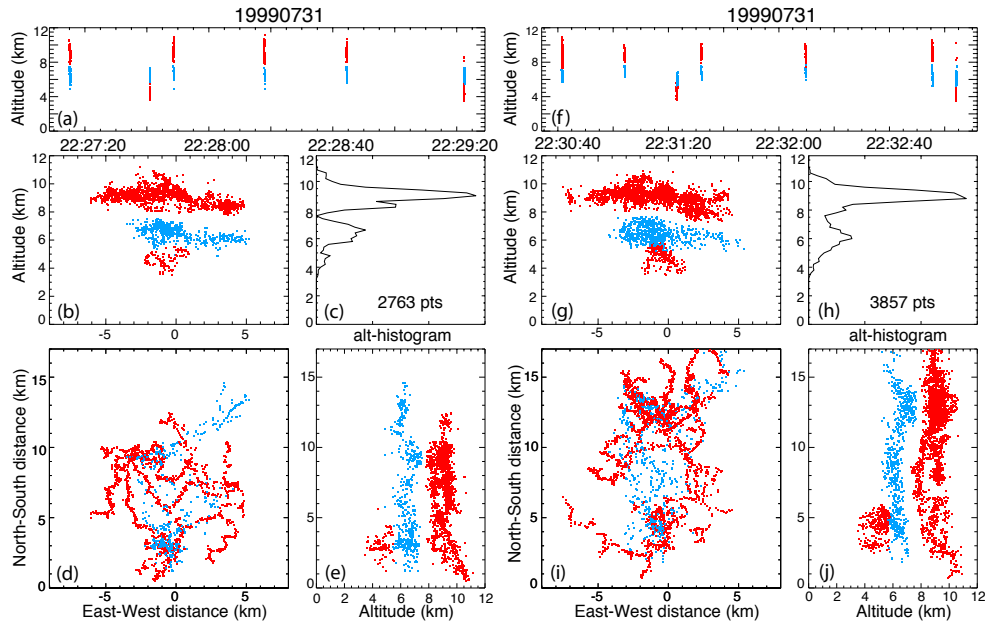


Figure 1: Lightning inferred storm charge structure for a six minute time interval of LMA data collected during a storm on July 31, 1999^[30]. Dark grey regions represent positive charge; the light grey regions represent negative charge. Panel (a) is a plot of the altitude of each source point versus time. Panel (c) is a histogram showing the number of source points present at each altitude. Panels (b), (d) and (e) show the source points in space as seen in the East-West ($x-z$), North-South ($y-z$) and horizontal ($x-y$) projection planes, respectively. Panels (f–j) are the same as panels (a–e).

events originated from 13 recorded lightning discharges, all of which were composed of well-defined channels.

Lightning channels are known to propagate preferentially in regions of intense charge density^[3, 8, 31, 32]. Hence, an image of the electrical structure of the thundercloud can be obtained by integrating in time the lightning events detected for a storm^[7]. Marshall *et al.*^[30] applied this method to the thunderstorm of July 31, 1999 considered in this paper and established its tripolar structure, showing a positive region between altitudes 8 and 11 km, a central negative charge region between 5.5 and 7.5 km and a lower positive region between 3.5 and 5.5 km (Figure 1).

Consequently, in this work, source points from a section of the storm are examined and labeled as either positive or negative depending on their location within the cloud. The source points are then discretized in the spatial domain, with each possible position corresponding to a point on the grid (Figure 2). Each charge layer is assumed to possess a predefined total net charge, which is divided evenly among the source points that belong to that layer. The central negative charge layer is assumed to possess a total net charge of -75 C, while the upper and lower positive charge layers are assumed to possess a total net

charge of 67.5 C and 7.5 C, respectively. Finally, the charge of each grid point is calculated by summing up the charges assigned to those source points which belong to the volume occupied by that grid point and its 26 immediate neighbors, and dividing the sum by 27. This method of averaging was implemented to limit the overall maximum charge density assigned to a single grid point.

Once charges are assigned to the grid points, the lightning discharge is simulated^[3]. The ground is modeled as a perfectly electrically conducting (PEC) flat plane, while the potential on the side and upper boundaries is calculated so that all charges inside the domain as well as their ground images are taken into account. The potential of the ground plane is set to $\phi_{gnd} = 0$. It follows that the potential at the boundaries before a discharge can be obtained from the following expression^[27]:

$$\phi(\vec{r}) = \phi_{amb}(\vec{r}) = \frac{1}{4\pi\epsilon_0} \left(\iiint_{V'} \frac{\rho_{amb}(\vec{r}')}{|\vec{r} - \vec{r}'|} dV' + \iiint_{V'} \frac{\rho_{amb}^i(\vec{r}'_i)}{|\vec{r} - \vec{r}'_i|} dV' \right) \quad (1)$$

where \vec{r} represents the coordinate vector of a boundary point and $\phi(\vec{r})$ represents the total potential at that point, $\rho_{amb}(\vec{r}')$ represents the ambient charge density at point \vec{r}' , while $\rho_{amb}^i(\vec{r}'_i)$ represents the ground image of the ambient charge density at point \vec{r}'_i . Once the potential $\phi(\vec{r})$ is calculated for every boundary point \vec{r} , Poisson's equation $\nabla^2\phi_{amb} = -\rho_{amb}/\epsilon_0$ is solved via a SOR algorithm^[33] to calculate ϕ_{amb} and $\vec{E}_{amb} = -\nabla\phi_{amb}$ at all other grid points.

The initiation and propagation thresholds of all lightning channels is assumed to be $E_{init} = E_{th}^{\pm} = \pm 2.16$ kV/cm at sea level^[34]. Effects of altitude on initiation and propagation are taken into account by scaling these thresholds with neutral density as follows^[35]:

$$E_{init} = E_{th}^{\pm} = \pm 2.16 \frac{N(z + z_{gnd})}{N_0} [kV/cm] \quad (2)$$

where z is the vertical distance above the ground, z_{gnd} is the altitude of the ground plane above sea level, and N is the value of the neutral charge density which takes on the value N_0 at sea level^[3, 8, 36].

The initiation point is chosen at random from the grid points which possess an electric field whose magnitude is greater than the initiation threshold. The lightning channel then begins to propagate from the initiation point, via the addition of a single link during each step. The candidates for the link to be added are composed of all sets of two points such that one point is part of the previously established discharge channel and the other is not part of the channel but is within one grid step of the previously mentioned point. Furthermore, the two points must possess a potential difference such that the propagation threshold E_{th}^{\pm} between them is exceeded. The electric field of a candidate i is computed as $E_i = (\phi^{start} - \phi^{end})/l$, where ϕ^{start} and ϕ^{end} are the potentials at the starting and ending grid points of the candidate link, respectively, and l is its length.

The probability that a given candidate i is chosen as the next propagation step is calculated from the formula^[6]: $p_i = |E_i - E_{th}|^{\eta} / \sum_i |E_i - E_{th}|$ where η is the sensitivity of the probability to field strength. Following the work of Niemeyer and Wiesmann^[37] and Popov^[38] on streamers and Mansell *et al.*^[2] on lightning discharge, η is set equal to 1. The total potential ϕ_0 of the channel is recalculated after every step to ensure the overall neutrality of the discharge. The process is repeated until there are no more candidates or the

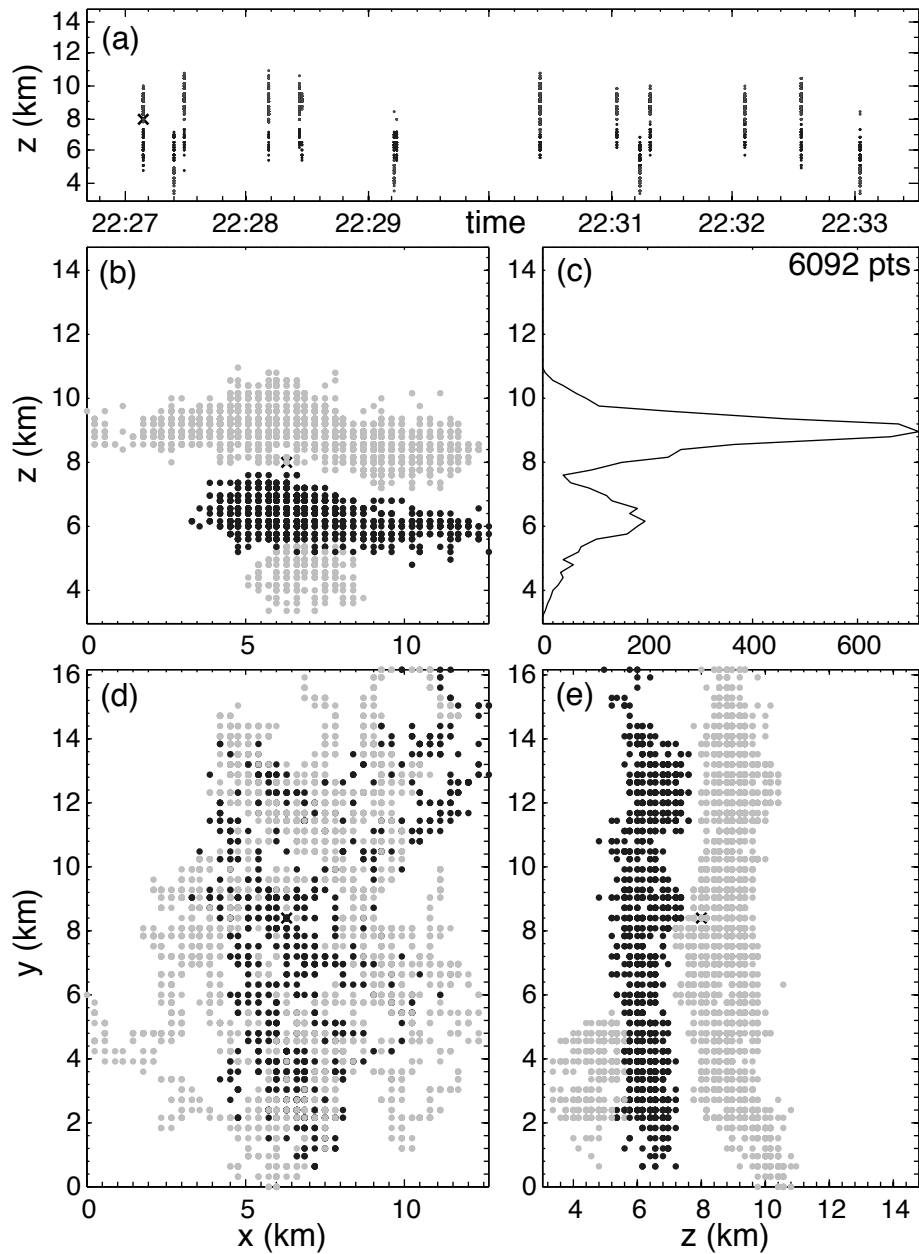


Figure 2: Discretized data points corresponding to the LMA data presented in Figure 1. Gray points correspond to regions of positive charge density and black points correspond to regions of negative charge density. The 'x' marks the earliest recorded point. Panels (a-e) are the same as in Figure 1.

channel reaches any boundary. Return strokes are not modeled for the set of simulations presented in this paper.

RESULTS

A total of 137 simulation runs were carried out over approximately 18 hours on a dual quad-core Mac Pro workstation. All simulation runs used a simulation domain of size $12.9 \text{ km} \times 16.5 \text{ km} \times 12.0 \text{ km}$ divided into rectangular volume elements of size $300 \text{ m} \times 300 \text{ m} \times 200 \text{ m}$ and used the discretized source points shown in Figure 2. Equivalently, the domain was divided into $4 \times 55 \times 60$ grid points along the x-, y- and z-directions, respectively.

The maximum number of links established during a simulated discharge was 432. 14 simulation runs produced no discharge channels because the respective initiation points had no neighboring grid points that allowed propagation of the channel. Of the 123 simulation runs that produced discharge channels, 103 produced intracloud discharges between the upper positive and central negative charge layers and 20 produced negative cloud-to-ground lightning. One discharge contained a single vertical channel that extended approximately three kilometers above the upper charge layer. We now present three representative simulation runs. The first produced a negative cloud-to-ground discharge and the second produced an intracloud discharge between the upper positive and central negative charge layers. The third run produced the discharge containing a subchannel extending three kilometers above the upper positive charge layer.

Figure 3 shows a negative cloud-to-ground stroke. Panel (a) represents the altitude of the initiation point and the endpoint of each new link at each step of the simulation. Panel (c) is a histogram showing the number of these model source points present as a function of altitude. Panels (b), (d) and (e) show the discharge as seen in the East-West (x-z), North-South (y-z) and horizontal (x-y) projection planes, respectively. The 'x' marks the initiation point, and the color scale ranging from black to light gray indicates the chronology of link addition. The discharge was initiated between the central negative and lower positive charge layers. Two branches then developed, with one propagating upward toward the central negative charge layer and the other downward toward the lower positive charge layer. After reaching the lower positive charge layer, the lower branch then propagated horizontally before continuing to descend and striking the ground. This discharge transferred a total charge of -42 C to the ground.

Figure 4 shows an intracloud discharge developing between the upper positive and central negative charge layers. As can be seen from Figure 4a, the discharge was initiated at an altitude of 8.8 km midway between the upper positive and central negative charge layers. The channel then branched and propagated vertically downward to the central negative charge layer and vertically upward to the upper positive charge layer, and then horizontally through both the upper positive and central negative charge layers for the remainder of the simulation run. The gross physical evolution of the channels is consistent with observations presented in this work and results previously obtained by Rioussset *et al.*^[3] (Figure 8). The charge carried by the positive leaders was -32 C . Since the discharge is overall neutral, the negative leaders carried 32 C . This can be interpreted as the charge transferred by the intracloud discharge^[3].

Figure 5 shows the anomalous intracloud discharge which contains a branch extending

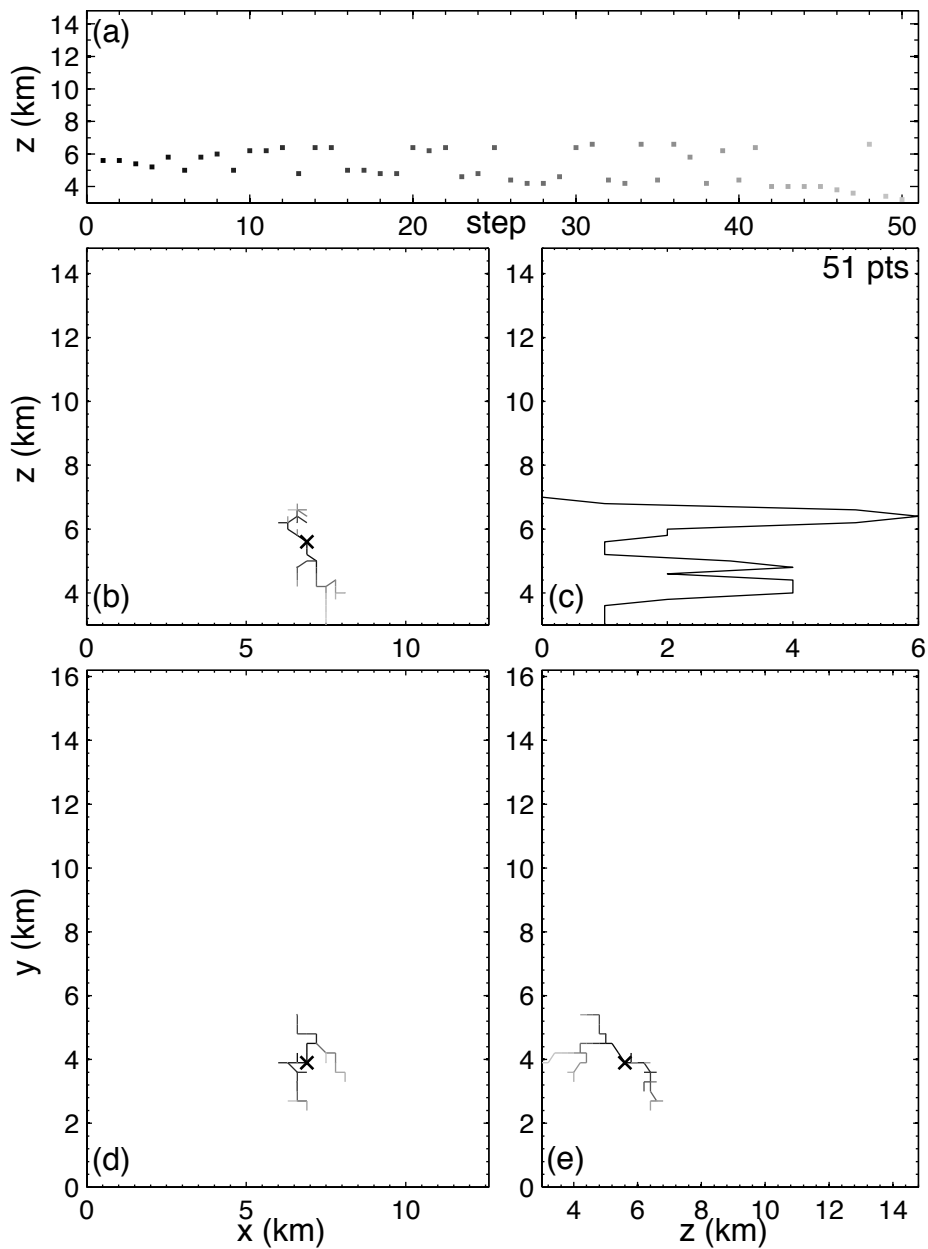


Figure 3: Representation in LMA data form of the representative cloud-to-ground discharge. Panels (a–e) are the same as in Figure 1.

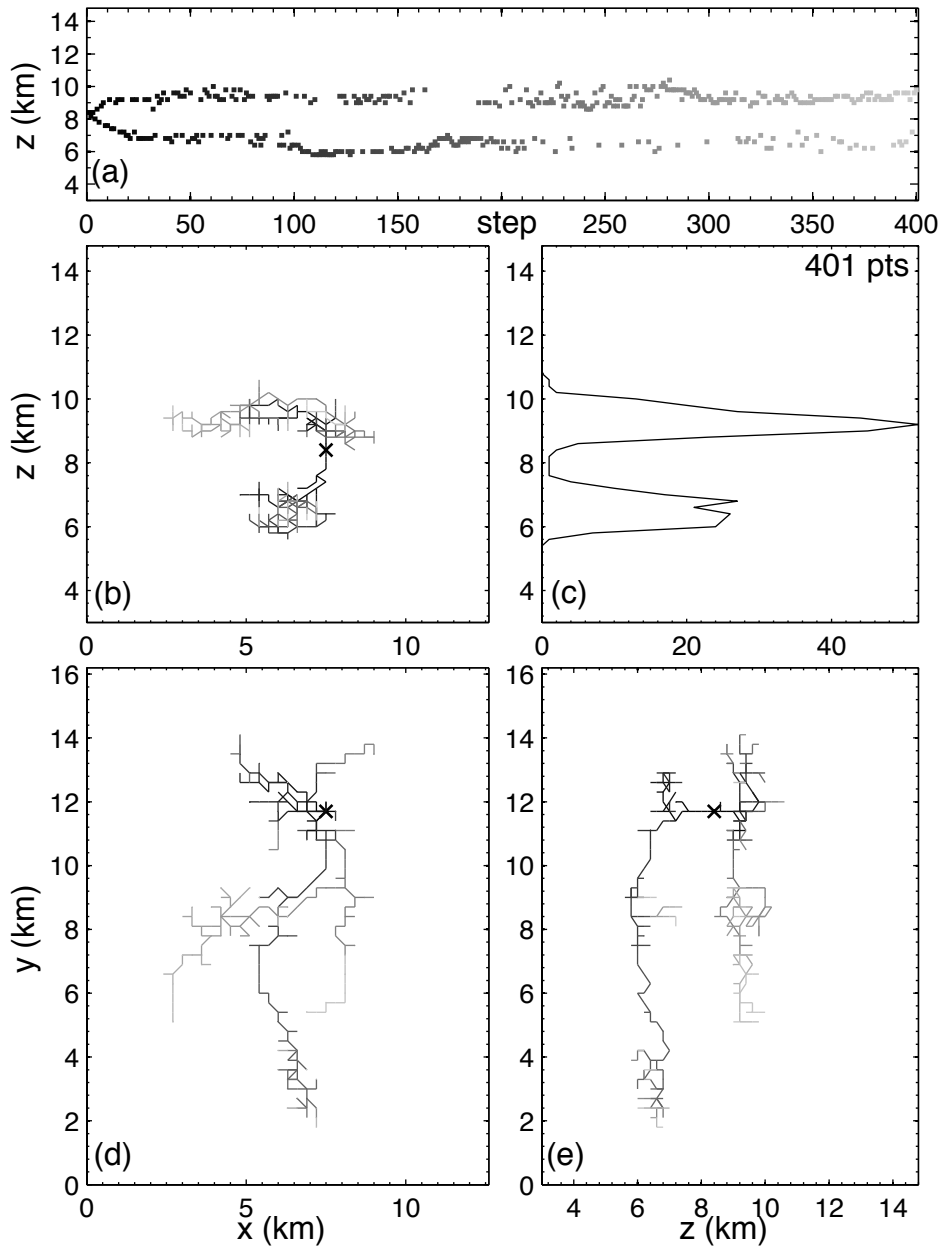


Figure 4: Representation in LMA data form of the representative intracloud discharge. Panels (a–e) are the same as in Figure 1.

approximately three kilometers above the top of the upper positive charge layer. This simulated discharge developed similarly to the intracloud discharge presented in Figure 4 and transferred an estimated 31 C. The upward channel comprised the final links added during the simulation. This channel was perfectly vertical, with no variation in either the x- or y-directions.

Also of interest are the number of candidates and the greatest amount by which a candidate exceeds the propagation threshold (or threshold overreach) for each link added during a simulation run. For the negative cloud-to-ground discharge (Figure 6a), the threshold overreach climbed quickly in the beginning of the simulation, followed more slowly by the number of candidates. Both values decreased after peaking, with the threshold overreach peaking before the number of candidates. Before the channel struck the ground, both values rose sharply due to the overall electric field enhancement between the lightning channel and its ground image. Both the ordinary (Figure 6b) and anomalous (Figure 6c) intracloud discharges contained four such cycles of increasing threshold overreach followed by increasing numbers of candidates. For the ordinary discharge, both quantities reached their highest values on the second-to-last crest. In contrast, the anomalous intracloud discharge produced overreach and numbers of candidates that attained their highest values on the final crest before flattening out for approximately 15 steps before the discharge terminated.

DISCUSSION

Based on the 123 simulation runs which produced lightning discharges, the ratio of occurrence of intracloud to cloud-to-ground lightning was ~ 5.15 , and all cloud-to-ground discharges were negative. The ratio of the types of discharges simulated slightly overestimates the values given by Krehbiel *et al.*^[7] for this particular thunderstorm (~ 3.46) and Rakov and Uman^[10] for other storms (2.5 to 3). However, the fact that the simulated charge structure did not change between simulation runs and thus could not be affected by previous simulated discharges and regeneration of charge can explain this discrepancy.

Rakov and Uman^[10] report that the total charge transferred by the stepped leader of a negative cloud-to-ground lightning is approximately 5 C, but that five percent of negative cloud-to-ground stepped leaders transfer more than 24 C. The model cloud to ground discharge (Figure 3) transferred -42 C, i.e., in the upper part of the range cited by Rakov and Uman^[10]. The amount of charge transferred by an intracloud discharge has been cited within the range of 3 C to 50 C^[10, 39-41], and previous fractal modeling performed by Mansell *et al.*^[2] estimated charge transfer to be between 36.3 and 52.4 C. Both the ordinary intracloud discharge as well as the anomalous intracloud discharge transferred an amount of charge (32 C and 31 C, respectively) in very good agreement with the aforementioned values.

Additionally, the cycles of crests and troughs of the number of candidates and maximum candidate overreach (Figure 6) suggests that discharge channels repeatedly approached pockets of high charge density, expanded within those pockets, and then sought out other pockets. This explanation is consistent with results previously established by Williams *et al.*^[32] for laboratory discharges, Coleman *et al.*^[31] for LMA observed lightning flashes, and Mansell *et al.*^[2] and Riousset *et al.*^[3] for simulated leader channels. Furthermore, the cycles could imply that growth of the discharge channel switches periodically between the upper and lower branches as they alternatively enter regions of intense charge. This is es-

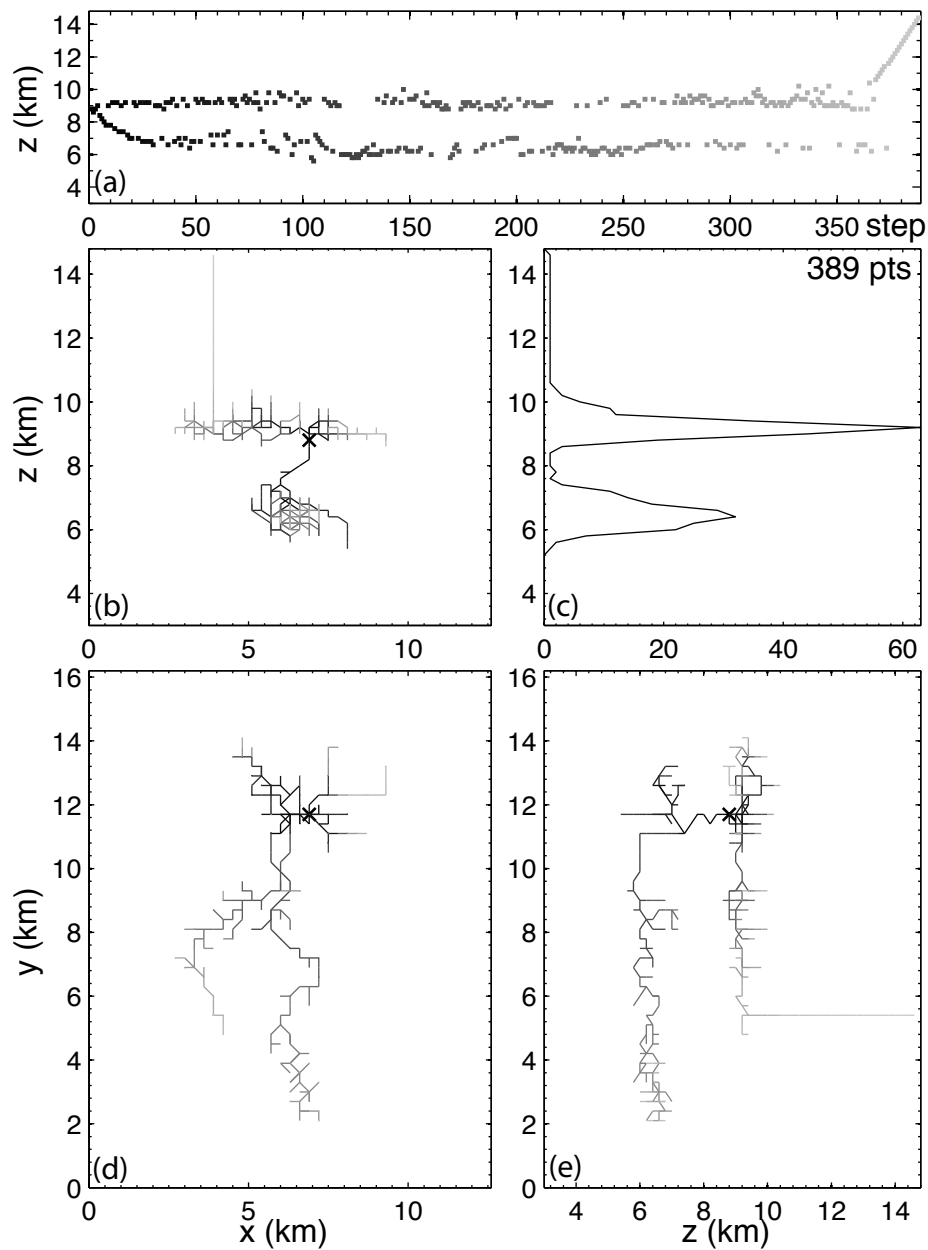


Figure 5: Representation in LMA data form of the anomalous intracloud discharge. This discharge is unusual in that a branch of the channel extended approximately three kilometers above the top of the upper positive charge layer. Panels (a–e) are the same as in Figure 1.

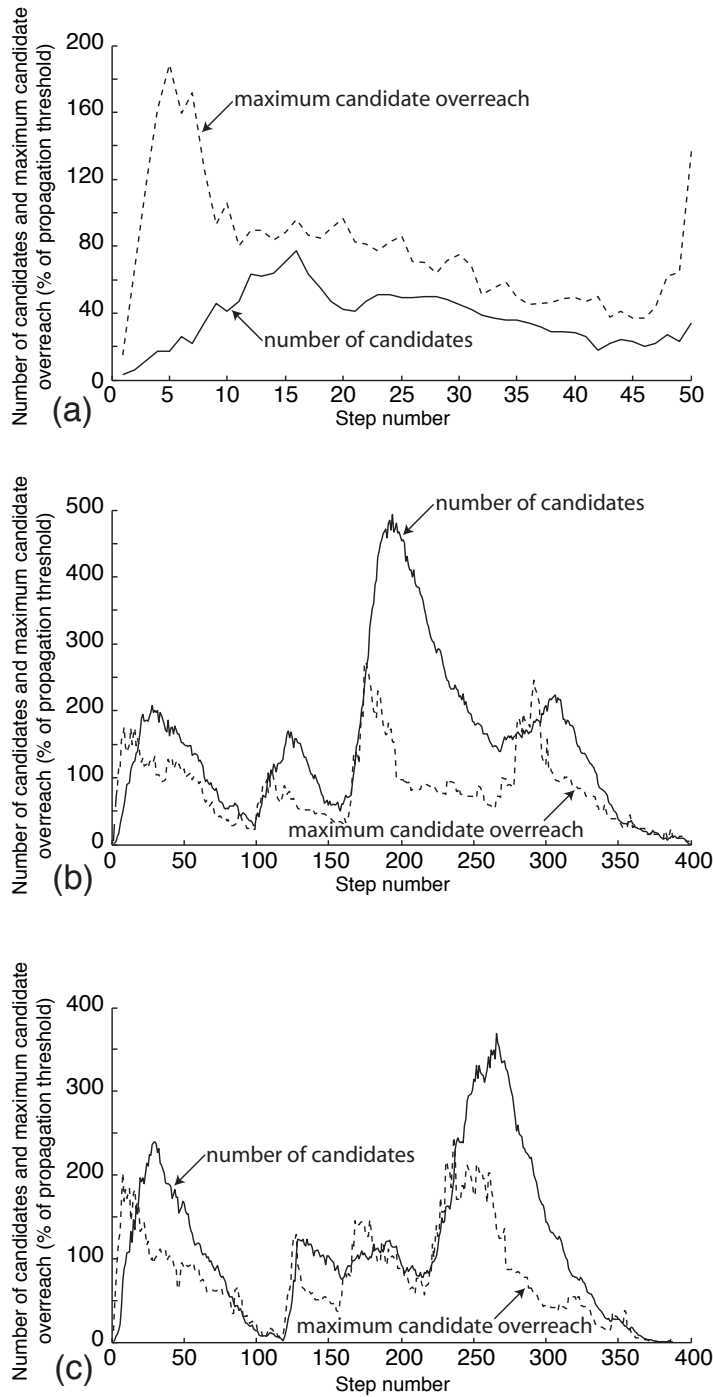


Figure 6: Number of candidates and maximum threshold overreach for (a) the cloud-to-ground discharge, (b) the ordinary intracloud discharge, and (c) the anomalous intracloud discharge.

pecially visible as the crests shown for the intracloud discharge (Figure 6b) occur at steps ~ 35 , ~ 125 , ~ 200 , and ~ 310 , corresponding to preferred development of channels of one polarity over the opposite one (Figures 4a).

The charge model developed in the present study was able to produce simulated discharges with well defined branches, with an appearance closer to typical discharges observed by the LMA (Figure 7) than the highly branched, space-filling simulated discharges observed by Riousset *et al.*^[3] (Figure 8). This improved similarity suggests a limitation of the uniformly charged axisymmetric tripole model used by Riousset *et al.*^[3] and others, and signifies an advantage of the modeling approach developed in the present work. Additionally, most discharges simulated in this work and containing more than 30 links exhibited a customary bilevel structure, in good agreement with observed LMA discharges.

CONCLUSIONS

This paper makes several contributions to the fields of atmospheric electricity and gas discharge modeling, which can be summarized as follows:

- The difference between the horizontal projection of the LMA event presented by Riousset *et al.*^[3] and its numerical modeling has been explained through the limitation of the uniformly charged axisymmetric tripole model as compared to the actual LMA inferred charge structure.
- The ability of the lightning model described in Riousset *et al.*^[3] to simulate both negative cloud-to-ground and intracloud discharges based on charges assigned from LMA data has been demonstrated by comparisons with relevant data available in the refereed literature and actual observed LMA events.
- Unusual discharge patterns, possibly related to jets^[8], have been observed during simulations based on the assigned charge structure.
- The pattern of greater candidate threshold overreach followed by greater numbers of candidates is consistent with the idea that discharges propagate through regions of intense charge or pockets of high charge density^[2, 3, 31, 32].

ACKNOWLEDGMENTS

This material is based upon work supported by the National Science Foundation under Grant No. EEC-0755081. The authors would like to thank Dr. Ronald Thomas at New Mexico Tech for his assistance with the XLMA visualization program.

REFERENCES

- ¹ N. I. Petrov and G. N. Petrova, "Physical mechanisms for intracloud lightning discharges," *Techn. Phys.*, **38** (4) 287–290 (1993).
- ² E. R. Mansell, D. R. MacGorman, C. L. Ziegler and J. M. Straka, "Simulated three-dimensional branched lightning in a numerical thunderstorm model," *J. Geophys. Res.*, **107** (D9) 4075, doi:10.1029/2000JD000244 (2002).

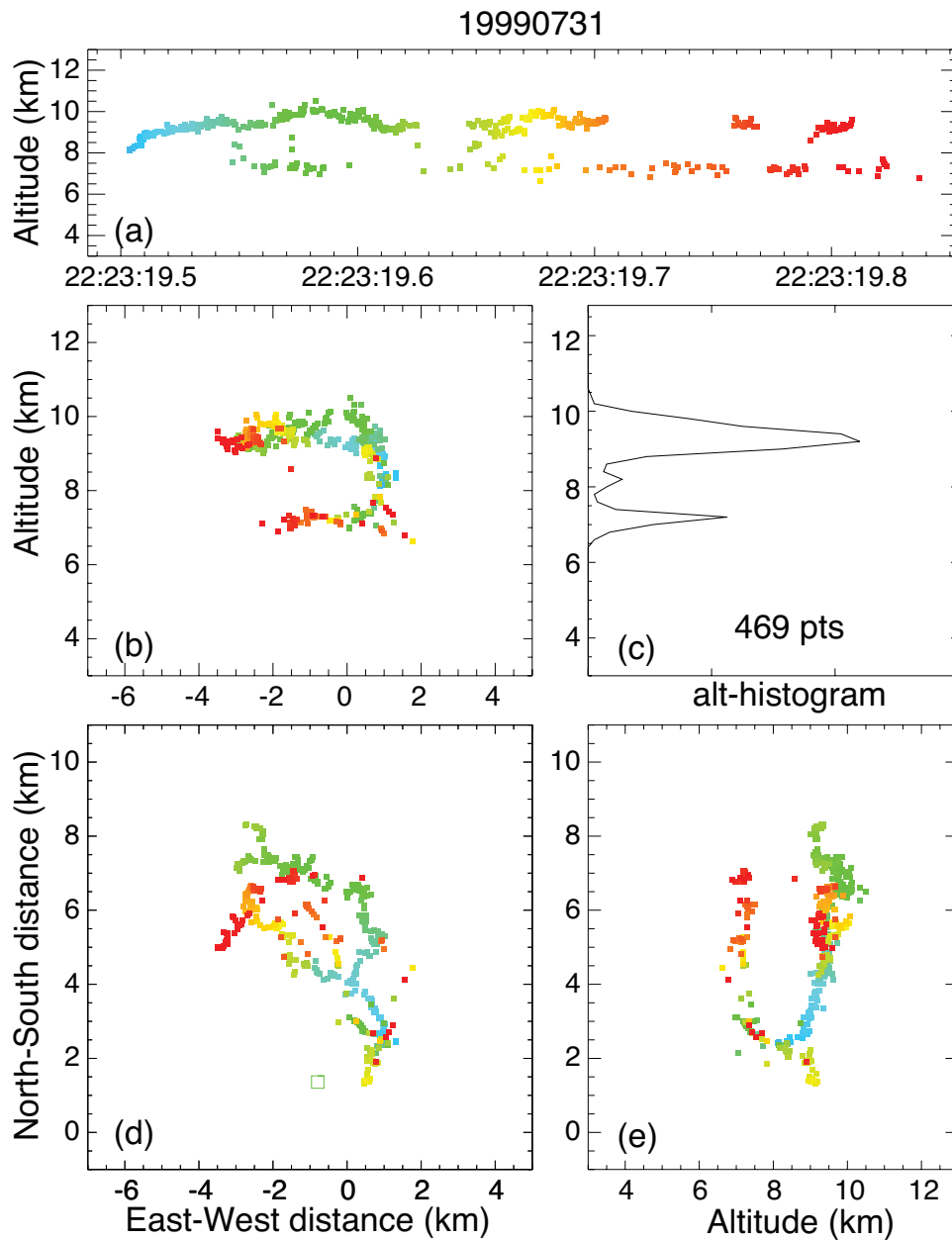


Figure 7: Actual intracloud lightning discharge observed by the LMA^[3]. Panels (a–e) are the same as in Figure 1.

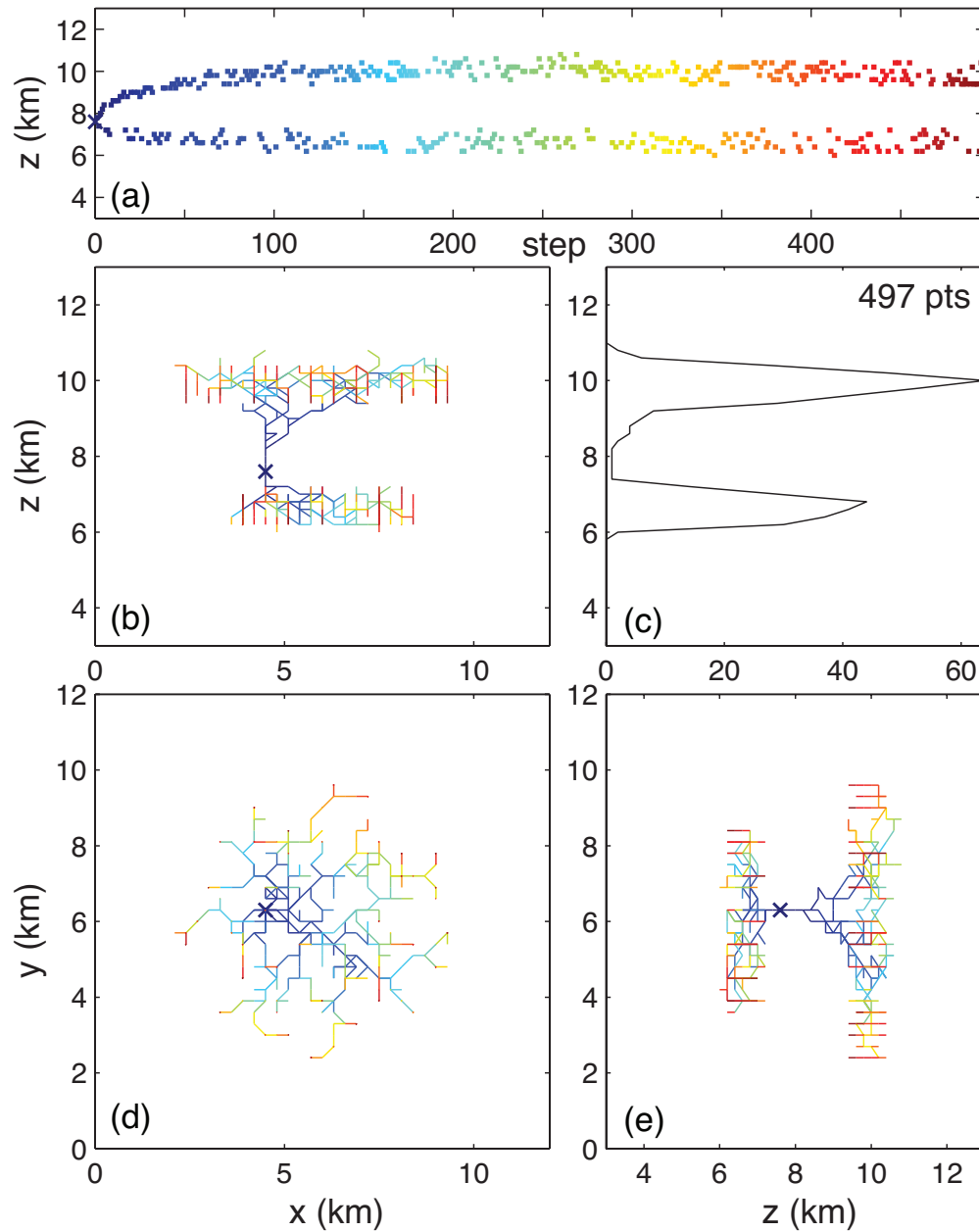


Figure 8: Intracloud lightning discharge simulated by Rioussset *et al.*^[3]. Panels (a–e) are the same as in Figure 1.

- ³ J. A. Rioussset, V. P. Pasko, P. R. Krehbiel, R. J. Thomas and W. Rison, “Three-dimensional fractal modeling of intracloud lightning discharge in a New Mexico thunderstorm and comparison with lightning mapping observations,” *J. Geophys. Res.*, **112** (D15203), doi:10.1029/2006JD007621 (2007).
- ⁴ H. W. Kasemir, “A contribution to the electrostatic theory of a lightning discharge,” *J. Geophys. Res.*, **65** (7) 1873–1878 (1960).
- ⁵ L. Niemeyer, L. Pietrono and H. J. Wiesmann, “Fractal dimension of dielectric breakdown,” *Phys. Rev. Lett.*, **52** (12) 1033–1036, doi:10.1103/PhysRevLett.52.1033 (1984).
- ⁶ N. Femia, L. Niemeyer and V. Tucci, “Fractal characteristics of electrical discharges: experiments and simulation,” *J. Phys D: Appl. Phys.*, **26** (4) 619–627, doi:10.1088/0022-3727/26/4/014 (1993).
- ⁷ P. Krehbiel, W. Rison, R. Thomas, T. Marshall, M. Stolzenburg, W. Winn and S. Hunyady, “Thunderstorm charge studies using a simple cylindrical charge model, electric field measurements, and lightning mapping observations,” *Eos Trans. AGU*, **85** (47), Fall Meet. Suppl., Abstract AE23A-0843 (2004).
- ⁸ P. R. Krehbiel, J. A. Rioussset, V. P. Pasko, R. J. Thomas, W. Rison, M. A. Stanley and H. E. Edens, “Upward electrical discharges from thunderstorms,” *Nature Geoscience*, **1** (4) 233–237, doi:10.1038/ngeo162 (2008).
- ⁹ B. Franklin, *Experiments and Observations on Electricity, made at Philadelphia in America*, E. Cave, London, UK, 1751.
- ¹⁰ V. A. Rakov and M. A. Uman, *Lightning: Physics and Effects*, Cambridge Univ. Press, Cambridge, U.K.; New York, 2003.
- ¹¹ T. Ogawa and M. Brook, “Mechanism of intracloud lightning discharge,” *J. Geophys. Res.*, **69** (24) 5141 (1964).
- ¹² I. Gallimberti, G. Bacchiega, A. Bondiou-Clergerie and P. Lalande, “Fundamental processes in long air gap discharges,” *C. R. Physique*, **3** (10) 1335–1359, doi:10.1016/S1631-0705(02)01414-7 (2002).
- ¹³ C. E. R. Bruce and R. H. Golde, “The Lightning Discharge,” *J. Inst. Elec. Engrs.*, **88** 487–505 (1941).
- ¹⁴ E. L. Hill, “Electromagnetic radiation from lightning strokes,” *J. Franklin Inst.*, **263** 107–119 (1957).
- ¹⁵ M. A. Uman, *Lightning*, reprint ed., Dover, Mineola, NY, 1984, originally published: New York: McGraw-Hill, 1969.
- ¹⁶ M. J. Kofoed, “Lightning discharge heating of aircraft skins,” *J. Aircraft*, **7** 21–26 (1970).
- ¹⁷ R. Godfrey, E. R. Mathews and J. A. McDivitt, “Analysis of Apollo 12 lightning incident,” *NASA Report MSC-01540* (1970).

- ¹⁸ S. A. Behnke, R. J. Thomas, P. R. Krehbiel and W. Rison, "Initial leader velocities during intracloud lightning: Possible evidence for a runaway breakdown effect," *J. Geophys. Res.*, **110** (D12) D10207, doi:10.1029/2004JD005312 (2005).
- ¹⁹ B. B. Mandelbrot, *The Fractal Geometry of Nature*, updated and augmented ed., W. H. Freeman, New York, NY, 1983, rev. ed. of: *Fractals*. 1977.
- ²⁰ B. B. Mandelbrot, D. E. Passoja and A. J. Paullay, "Fractal character of fracture surfaces of metals," *Nature*, **308** 721–722 (1984).
- ²¹ S. Satpathy, "Fractal dimension of dielectric breakdown—Comment," *Phys. Rev. Lett.*, **57** (5) 649, doi:10.1103/PhysRevLett.57.649 (1986).
- ²² L. Niemeyer, L. Pietrono and H. J. Wiesmann, "Fractal dimension of dielectric breakdown—Response," *Phys. Rev. Lett.*, **57** (5) 650, doi:10.1103/PhysRevLett.57.650 (1986).
- ²³ W. Rison, R. J. Thomas, P. R. Krehbiel, T. Hamlin and J. Harlin, "A GPS-based three-dimensional lightning mapping system: Initial observations in central New Mexico," *Geophys. Res. Lett.*, **26** (23) 3573–3576, doi:10.1029/1999GL010856 (1999).
- ²⁴ R. J. Thomas, P. R. Krehbiel, W. Rison, T. Hamlin, J. Harlin and D. Shown, "Observations of VHF source powers radiated by lightning," *Geophys. Res. Lett.*, **28** (1) 143–146 (2001).
- ²⁵ E. M. Wescott, D. Sentman, D. Osborne, D. Hampton and M. Heavner, "Preliminary results from the Sprites94 aircraft campaign: 2. Blue jets," *Geophys. Res. Lett.*, **22** (10) 1209–1212 (1995).
- ²⁶ W. L. Boeck, O. H. Vaughan, R. J. Blakeslee, B. Vonnegut, M. Brook and J. McKune, "Observations of lightning in the stratosphere," *J. Geophys. Res.*, **100** 1465 (1995).
- ²⁷ V. P. Pasko, M. A. Stanley, J. D. Matthews, U. S. Inan and T. G. Wood, "Electrical discharge from a thundercloud top to the lower ionosphere," *Nature*, **416** 152–154, doi: 10.1038/416152a (2002).
- ²⁸ H. T. Su, R. R. Hsu, A. B. Chen, Y. C. Wang, W. S. Hsiao, W. C. Lai, L. C. Lee, M. Sato and H. Fukunishi, "Gigantic jets between a thundercloud and the ionosphere," *Nature*, **423** 974–976, doi:10.1038/nature01759 (2003).
- ²⁹ E. R. Williams, "The tripolar structure of thunderstorms," *J. Geophys. Res.*, **94** (D11) 13151–13167 (1989).
- ³⁰ T. C. Marshall, M. Stolzenburg, C. R. Maggio, L. M. Coleman, P. R. Krehbiel, T. Hamlin, R. J. Thomas and W. Rison, "Observed electric fields associated with lightning initiation," *Geophys. Res. Lett.*, **32** (3) L03813, doi:10.1029/2004GL021802 (2005).
- ³¹ L. M. Coleman, T. C. Marshall, M. Stolzenburg, T. Hamlin, P. R. Krehbiel, W. Rison and R. J. Thomas, "Effects of charge and electrostatic potential on lightning propagation," *J. Geophys. Res.*, **108** (D9) 4298, doi:10.1029/2002JD002718 (2003).

- ³² E. R. Williams, C. M. Cooke and K. A. Wright, “Electrical discharge propagation in and around space charge clouds,” *J. Geophys. Res.*, **90** (D4) 6059–6070 (1985).
- ³³ R. Hockney and J. Eastwood, *Computer Simulation Using Particles*, McGraw-Hill, New York, NY, 1981.
- ³⁴ V. P. Pasko and J. J. George, “Three-dimensional modeling of blue jets and blue starters,” *J. Geophys. Res.*, **107** (A12) 1458, doi:10.1029/2002JA009473 (2002).
- ³⁵ V. P. Pasko, “Theoretical modeling of sprites and jets,” in: M. Füllekrug, E. A. Mareev and M. J. Rycroft, ed., “Sprites, Elves and Intense Lightning Discharges,” vol. 225 of *NATO Science Series II: Mathematics, Physics and Chemistry*, pp. 253–311, Springer, Heidelberg, Germany, 2006.
- ³⁶ J. A. Riousset, *Fractal modeling of lightning discharges*, Master’s thesis, The Pennsylvania State University, University Park, PA (2006).
- ³⁷ L. Niemeyer and H. J. Wiesmann, “Modeling of leader branching in electronegative gases,” pp. 134–139, *Gaseous Dielectrics V: Proceedings of the Fifth International Symposium on Gaseous Dielectrics: Knoxville, TN, 3-7 May (1987)*.
- ³⁸ N. A. Popov, “Spatial structure of the branching streamer channel in a corona discharge,” *Plasma Phys. Rep.*, **28** (7) 615–622, doi:10.1134/1.1494061 (2002).
- ³⁹ P. R. Krehbiel, *An analysis of the electric field change produced by lightning*, Ph.D. thesis, University of Manchester Institute of Science and Technology, Manchester, UK (1981).
- ⁴⁰ P. R. Krehbiel, M. Brook, S. Khanna-Gupta, C. Lennon and R. Lhermitte, “Some results concerning VHF lightning radiation from the real-time LDAR system at KSC, Florida,” pp. 388–393, *Proc. VIIth Intn’l. Conf. Atmos. Elec.*, Albany, NY (1984).
- ⁴¹ X. M. Shao and P. R. Krehbiel, “The spatial and temporal development of intracloud lightning,” *J. Geophys. Res.*, **101** (D21) 26641–26668 (1996).

DEVELOPMENT OF DATA PROCESSING VI'S IN LABVIEW FOR REAL-TIME QUARTZ CRYSTAL RESONANCE FREQUENCY AND QUALITY FACTOR MONITORING

Nona Ebrahimi^{*}, Ping Kao⁺, Ashish Patwardhan⁺, Srinivas Tadigadapa[#]

Department of Electrical Engineering
The Pennsylvania State University, University Park, PA 16802

^{*}Undergraduate Student of
Department of Computer Engineering
University of Michigan
Ann Arbor, MI 48109

ABSTRACT

A LabVIEW program is needed to measure the frequency shift in quartz resonators in real time. These resonators respond to changes occurring on their surface, such as: addition of mass, viscoelastic loading, or temperature changes, by a change in the resonance frequency and the quality factor. This LabVIEW program calculates the Q-factor and frequency and plots them in real time on the computer. This allows the user to determine the frequency change arising from a given sample in real-time. The program will be incorporated into a data acquisition software previously written in LabVIEW. The objective of this research is to make it possible to process and interpret resonance data in real-time for graduate students to study the properties of such resonators.

INTRODUCTION

Quartz crystal resonators are piezoelectric devices¹. Piezoelectricity is the ability of these devices to create an electric potential in response to applied stress.

⁺ Graduate Student Mentor

[#] Faculty Mentor

Conversely, when an electric potential is applied, it may cause the device to have a mechanical distortion. The MEMS group has micro-machined these quartz resonators with a fundamental resonance frequency of 90MHz. These resonators

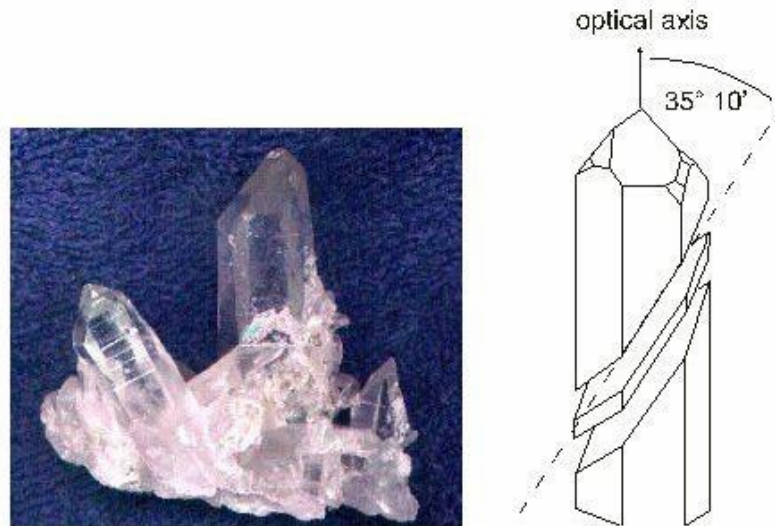


Figure 1. AT-cut quartz crystal – Google Images

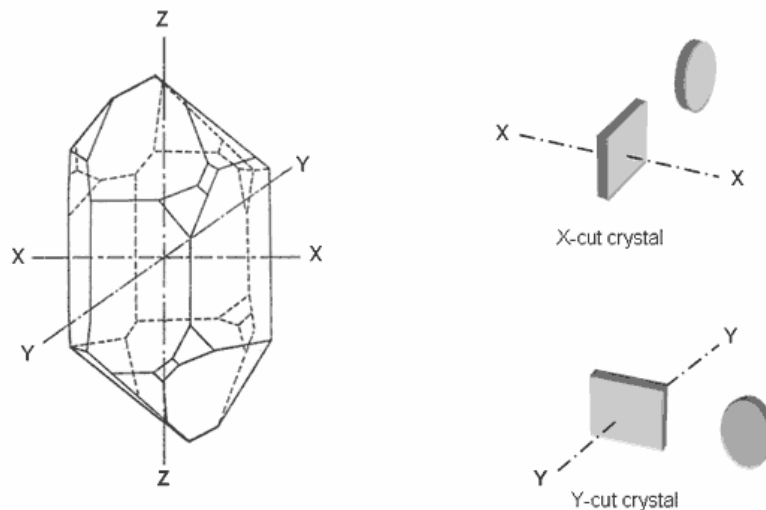


Figure 2. Y-cut quartz crystal – Google Images

are going to be used for gravimetric as well as thermal sensing such as IR-detection as well as other types of calorimetric sensing.

The electrodes on these devices are either attached to a thin disk of an AT-cut quartz or a Y-cut quartz. AT-cut quartz devices as seen in Figure 1 are cut at a 33-36 degree angle and are insensitive to temperature change from 20 to 60 °C.

Y-cut devices which can be seen in Figure 2 are cut along the y-axis with a temperature sensitivity of 90 ppm (parts per million)/°C.

The objective of this research is to develop a LabVIEW program that will facilitate the real time monitoring of these parameters to be used for further research. Currently, we are unable to calculate the resonance frequency in real time, as the current data acquisition and data processing software are not designed for such an application.

EXPERIMENTAL DESCRIPTION

RUNNING THE EXPERIMENT

The quartz resonator devices are created by the graduate students. These devices are created using y-cut quartz. The quartz resonators are coated with a nickel layer which acts as a hard mask and are then etched with various chemicals to fabricate the device². Connections within the device are made with gold lines that carry the electric signal across³. The impedance of the fabricated resonators (Figure 4) is measured as a function of frequency, and the frequency at which the quartz moves (resonates) is documented by the Agilent 4294A impedance analyzer in Figure 3. The impedance analyzer is then connected to the computer which through a LabVIEW program reads and documents the frequency, impedance, and angle about every two seconds. These tests are done in the lab and generally take a few hours to run through.

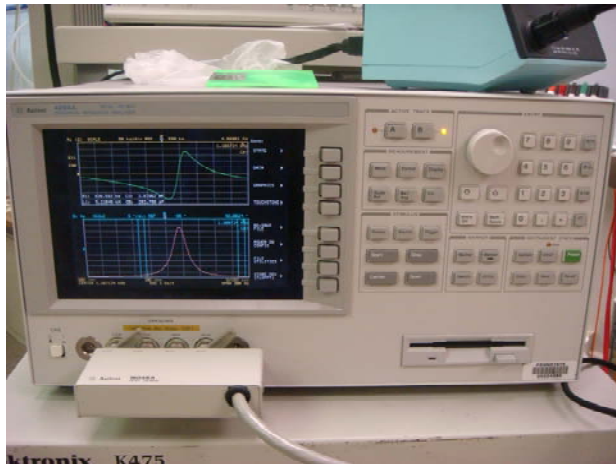


Figure 3. Agilent 4294A Impedance Analyzer

- The top graph represents an impedance vs. frequency graph.
- The bottom graph represents an angle vs. frequency graph.

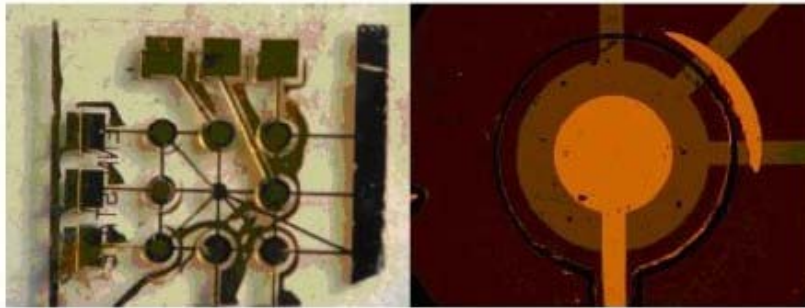


Figure 4. A fabricated device. ³

FITTING THE LORENTZIAN CURVE

One problem with running these experiments in the current form is that the frequency and phase data can only be obtained after the entire experiment is completed by performing a non-linear Lorentzian fit to the acquired data. A program was needed to take the results written from the original LabVIEW program in real-time and fit the angle vs. frequency graph to a Lorentzian curve using this equation:

$$a0 + \frac{A * \left(\frac{f * \cos(\phi)}{f0} + \left(1 - \frac{f^2}{f0^2} \right) * Q * \sin(\phi) \right)}{\frac{f^2}{f0^2} + \left(1 - \frac{f^2}{f0^2} \right)^2 * Q^2}$$

where,

- a0: minimum impedance
- A: maximum impedance – minimum impedance
- Q: quality factor
- phi: 1
- f0: the resonance frequency
- f: the frequency

Process.

Getting accustomed to LabVIEW was the first issue, although LabVIEW is considered a programming language, it is much different than other languages. Each program in LabVIEW is called a VI or a virtual instrument. LabVIEW contains graphical functions which have all been predefined and can be accessed just by right clicking on either the front panel or the block diagram. The front panel is similar to the controls panels of a machine. It is where the user can run the program and add any inputs needed as can be seen in Figure 5. Here, the user can also any graphs plotted. The front panel is basically the GUI (graphical user

interface) of the program. The block diagram is where the program is actually written. The functions on the block diagram have inputs and outputs which have to be wired together⁴. An issue with LabVIEW is that often it is difficult to find the function needed to do the task wanted, and it is also confusing to know exactly what data type needs to go into the slot. Many times, it takes a few hours just to figure out what kind of wires needs to be put into a function. Though LabVIEW does have its advantages, after a program has been written, it is easy to follow how the program works especially with its help button which shows a small excerpt of what a functions does when you hover over it, and each data type does have its own color which sometimes can help try to debug a problem.

Calculating the constant Lorentzian values was relatively easy once LabVIEW got easier to work with, a notepad file was created from a previous experiment. The file was read, and it extracted three columns, frequency, impedance, and angle, to calculate all the constant values. Then, a *for* loop was used that goes through the frequency array extracting the frequency variable which is the only altering variable in the equation and outputting another array which is the result of the Lorentzian equation.

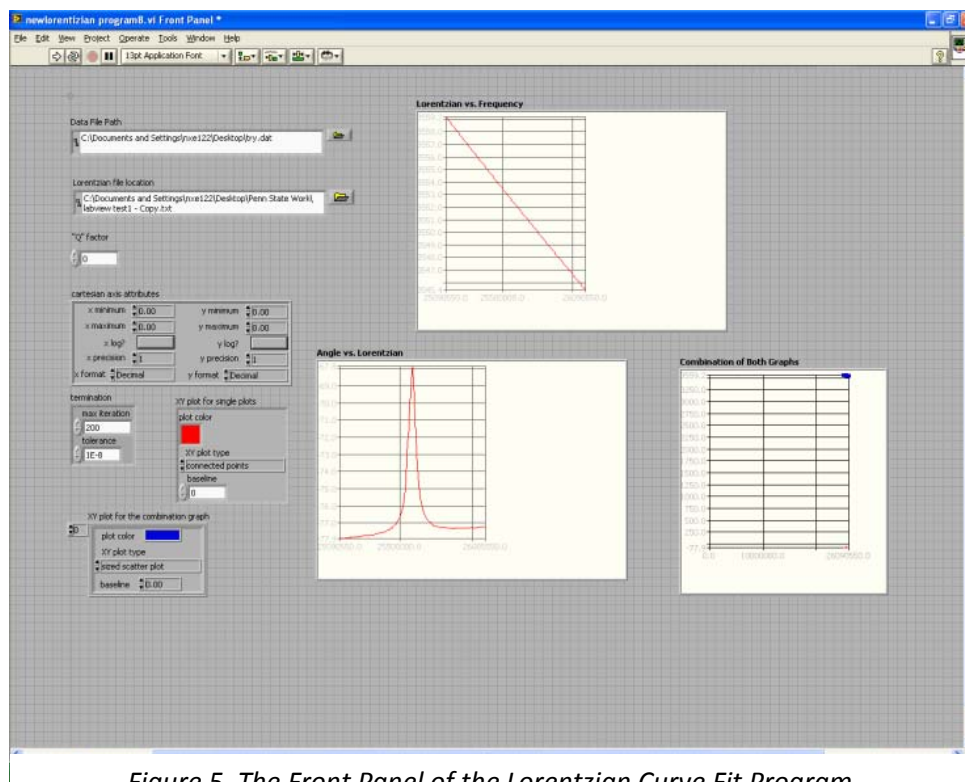


Figure 5. The Front Panel of the Lorentzian Curve Fit Program

Complications.

Not knowing exactly how the Lorentzian function worked initially, it was assumed that calculating the values through the equation would automatically output the values that were needed and all that needed to be done were to plot them.

The plot function alone was complicated enough. The plot xy function expects a cluster of arrays with (x, y) values. A problem with LabVIEW is that when the user does not know what something is such as the cluster, LabVIEW will not tell the user exactly what it is in the help file. So through much search, it was figured out how to convert an array to a cluster using the index then an array was built to make fit into the data slot in the plot xy function. It was subsequently realized that the multi-plot xy function should be used so that the actual curve and the fit curve could be put on top of one another. This too was very complicated. In the end, it was discovered that the Lorentzian values from the equation were not what was needed since when the graph was plotted, the location was much higher in the graph and much larger than the graph we had. Luckily though, it did have the shape wanted.

It was discovered that a Non-Linear Curve Fit function was needed, which had been the most complicated function the first author (NE) had seen yet, and the help poorly described how it worked. Using all the resources available to understand this function including using both the National Instruments discussion forms and calling National Instruments themselves, we were finally able to wire all the functions in after much complication.

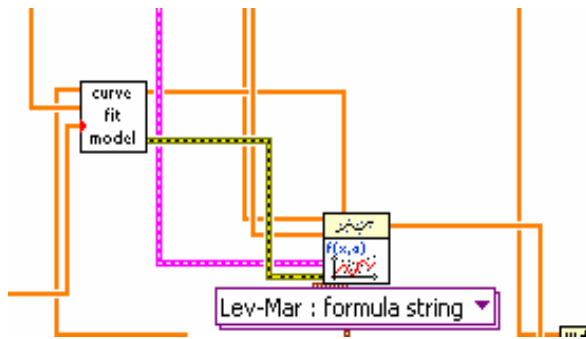


Figure 6. Non-Linear Curve Fit Function

function. It also takes in x, y, the initial coefficients, and data points needed in the reference VI to do the calculations which would be the constants in the Lorentzian equation. In the end, the representative from National Instruments said that this was not the best type to use for the program.

The Lev-Mar: formula string is a little easier to use. It still needs a separate VI, the curve fit model, to go through the equation and do the necessary

The Non-Linear Curve Fit function (Figure 6) is a complex function. There are actually two different types: the Lev-Mar: VI and the Lev-Mar: formula string, both of which we attempted to use in the Lorentzian fit program.

The Lev-Mar: VI requires a reference VI which a for loop that runs through the equation and outputs the $f(x,a)$

calculations. The curve fit model VI is run into the initial coefficients slot in the Non-Linear Curve Fit function. The model equation is written as a constant and wired into the model description slot. The model description contains the equation, the constant variables, and the changing variable. This is where the current error resides. The error 23028, “the wrong model equation,” keeps popping up, and currently, there is no way to remove/fix this error. A National Instrument representative has looked at the code, and he is keen on the idea that it is possibly a LabVIEW software error.

RESULTS AND DISCUSSION

The program currently runs through and calculates all the needed constants for the Lorentzian equation. It also can plot the functions on both the multi-plot xy function and the plot xy function which are relatively complicated functions that need to be put into a cluster rather than an array for the function to work. The Non-Linear Curve Fit function has a small error where it has a problem with the model description portion of the function that needs to be fixed, but other than that, the program works the way it should.

CONCLUSION AND FUTURE WORK

In the future, this program will be picked by someone who has worked with LabVIEW and once it is fixed, it will be integrated with the existing data logging program. Time was a constraint and hence this was not implemented.

Eventually, this program will help future graduate students do tests on quartz crystal resonators with the impedance analyzer and be able to watch as the test is happening on the LabVIEW Lorentzian fit program. This way the graduate students can not only be able to see the curve of the reaction in slow motion, but they can also be able to watch the reaction as it is happening to make sure there is no problem in their test allowing them to save time since some of these tests can go on for hours without anyone knowing the result until it is over. This program just needs to be integrated into the current LabVIEW program that has already been made to collaborate with the impedance analyzer, get the data containing the frequency, impedance, and angle, and write it into a notepad file and this will be done shortly.

ACKNOWLEDGEMENT

One of the authors (NE) would like to personally thank Ken Jenkins, Ruyan Guo, Don Natale, and Mary Ann Henderson for organizing everything in this program. She would especially like to thank Ping Kao, Ashish Patwardhan and Srinivas Tadigadapa for helping get through this project.

Nona Ebrahimi, Ping Kao, Ashish Patwardhan , and Srinivas Tadigadapa

85

This material is based upon work supported by the National Science Foundation under Grant No. EEC-0755081.

REFERENCES

- ¹Martin, Stephen, Granstaff, Victoria, and Frye, Gregory. "Characterization of a Quartz Crystal Microbalance with Simultaneous Mass and Liquid Loading." 2 August 1991: 1. Print.
- ²Kao, Ping, Patwardhan, Ashish, Allara, David, Tadigadapa, Srinivas. "Human Serum Albumin Adsorption Study on 62-MHz Miniaturized Quartz Gravimetric Sensors." 14 May 2008: 3. Print.
- ³Patwardhan, Ashish. "Thermal Sensing Using Micromachined Y-cut Quartz Resonators." July 2008. Pennsylvania State University Print.
- ⁴Johnson, Gary W. "LabVIEW Graphical Programming: Practical Applications in Instrumentation and Control." 1997: 55- 109.

SPATIAL AND TEMPORAL SHAPING OF FEMTOSECOND LASER PULSES

Jeremy Dwyer^{*}, Haifeng Li⁺, and Zhiwen Liu^{*}

Department of Electrical Engineering
The Pennsylvania State University
University Park, PA 16802

^{*}Undergraduate student of
Department of Electrical Engineering
Grove City College
Grove City, PA 16127

ABSTRACT

Two-dimensional shaping of femtosecond laser pulses will be examined. Depending on the system used and the applications, simultaneous time shaping and spatial shaping or two dimensional spatial shaping of femtosecond laser pulses can be achieved. A simulation has been performed for a simultaneous time shaping and spatial shaping system. A two-dimensional phase profile has been generated from this simulation, which can be converted to a phase mask for a pulse shaping system. With the phase mask, a pulse shaping system can be used shape a pulse in one spatial dimension and temporally. In generating the phase, the input to the pulse shaping system was assumed to be a spatially and temporally Gaussian-shaped femtosecond pulse, whose center stays in the same place throughout the duration of the pulse. The desired output pulse was also assumed to be Gaussian-shaped spatially, but with a spatial center that moves gradually with time. When the generated phase distribution is applied to the initial waveform, the final intensity profile generated differs from the ideal intensity profile by a mean-squared error of only 0.76 %. The final waveform

⁺ Graduate Mentor

^{*} Faculty Mentor

achieves movement in the spatial dimension, moving approximately 0.125 mm in the full-width half maximum (FWHM) time interval of the pulse, which lasts 1.665 ps.

INTRODUCTION

Beam (spatial) shaping and pulse (time) shaping have both been well documented in literature, and have a variety of uses. Beam shaping has been useful in such areas as lithography, laser printing, and medical applications.^[1] Pulse shaping has also had several uses. One use of pulse shaping is to compensate for phase distortion of pulses accumulated by traveling through long lengths of fiber. Another use for pulse shaping is in high speed information networks.^[2]

Simultaneous spatial and temporal shaping of ultrashort pulses is also possible. Spatiotemporal shaping of ultrashort pulses can be useful for multiplexing signals in optical processing applications.^[5] For this project, the simultaneous time and space shaping of femtosecond pulses will be explored. Specifically, simultaneous shaping in one spatial dimension and time will be presented. We will specifically look at the shaping of an input pulse which has a Gaussian profile spatially, and whose center remains stagnant throughout the duration of the pulse. This initial pulse can be shaped to a final waveform with a spatially-Gaussian profile, but with a center that moves throughout the duration of the pulse. In the space-time shaping system we used, a phase mask allows for the conversion from one waveform to another. The goal of our research was to find the phase for the phase mask which would generate the desired final waveform from the initial one. A final pulse such as this could have an application as an ultrafast scanner. We will describe the process used to find the necessary phase and discuss the results we generated.

DESCRIPTION OF SPATIOTEMPORAL PULSE SHAPING SYSTEM

Spatiotemporal shaping of pulses can be accomplished by using an apparatus used extensively in pulse shaping applications, with slight modifications.^[2,3,5] An illustration of this pulse shaping system is shown in Figure 1.

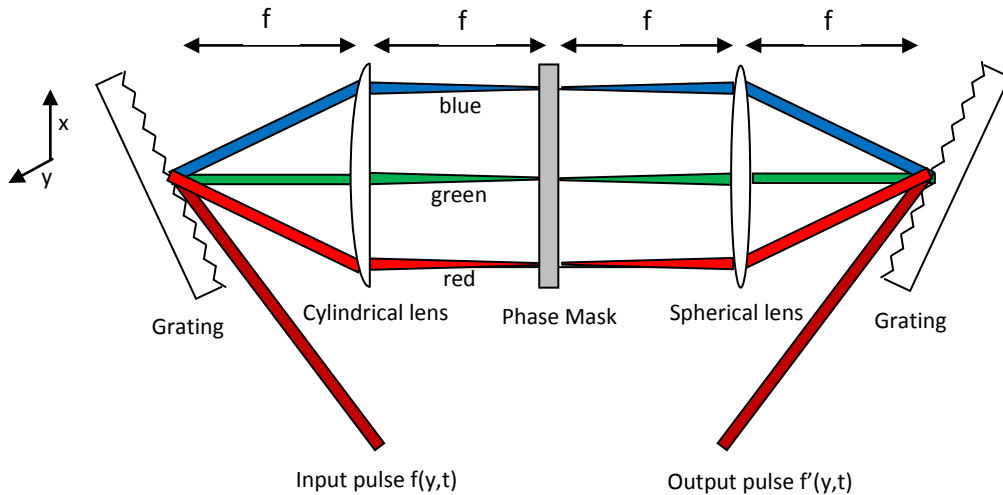


Figure 1. Illustration of spatiotemporal pulse-shaping system.

The pulse-shaping system allows us to shape the pulse in the time dimension and in the y -spatial dimension (pointing out of the page). The input pulse contains multiple wavelength components. When the input pulse hits the first grating of the system, the different wavelengths of light composing the input pulse will diffract off the grating at different angles. The first lens focuses the beam onto a phase mask in the x dimension, and allows the y dimension to pass through unchanged. (The first lens is a cylindrical one, so it only collimates in the x dimension where the frequency components are diffracted, and does not affect the y dimension.) The different wavelengths of the pulse are now separated spatially along the mask in horizontal lines (Figure 2). Along the spatial dimension x , the light distribution can be thought of as a time Fourier transform of the pulse. Along the y dimension, spatial information about the y dimension of the input beam is still present. The first grating and the first cylindrical lens do not affect the distribution of light along the y -axis. Therefore, each frequency line at the mask contains spatial information about the y dimension.

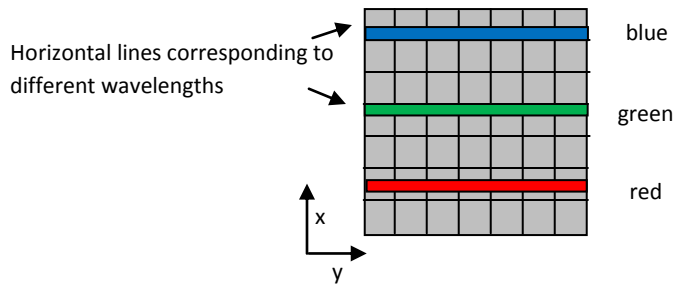


Figure 2. Close-up of phase mask from Figure 1. The frequency components at the phase mask appear in horizontal lines.

The pulse will then pass through a two-dimensional phase mask, which is able to add different phases to different frequency and y-spatial components. This will eventually be responsible for the shaping of the pulse. After this, the beam will pass through the spherical lens, which would focus all of the horizontal frequency lines onto the second grating. The second grating, which is placed symmetrically with respect to the mask, will recombine the frequency components. Like the first grating and lens can be thought to perform a Fourier transform with respect to time, the second lens and grating can be thought to perform an inverse Fourier transform with respect to time. From Fourier optics, it is known that a spherical lens can perform a Fourier transform of an image at one of its focal planes.^[4] This Fourier transform is found at the focal plane on the other side of the lens. This means that the y-spatial profile at the second grating will be a spatial Fourier transform of the y-spatial profile at the phase mask. The second grating does not affect the y-spatial components, so the pulse that comes off the second grating can be thought of as the inverse time Fourier transform and y-spatial Fourier transform of the waveform at the phase mask.^[5]

The fact that the pulse shaping system more or less inverse Fourier transforms the waveform at the phase mask with respect to time and Fourier transforms the waveform at the phase mask with respect to one spatial dimension allows us to shape the output waveform of the system. Placing a two-dimension phase mask in the center of the pulse shaping apparatus allows a phase to be added to the frequency components and the y-spatial components of the initial waveform. From Fourier transform theory, it is well known that the phase information carried by a function dramatically affects its Fourier transform or inverse Fourier transform.^[7] Therefore, by adding a phase to the waveform in the center of the pulse shaping apparatus, we are able to shape the waveform with respect to time and the y-spatial dimension.

With a two-dimensional phase mask, it is possible to do time shaping of the beam in the x direction and one dimensional spatial shaping in the y direction. The next section will describe the initial and final waveforms assumed in generating the phase, as well as the procedure for generating the phase. Generating the phase for a two-dimensional spatial shaping problem can be done in a similar manner.

SIMULATION

The object of the simulation is to generate the phase needed to go from a spatially-Gaussian shaped pulse with a static center to a Gaussian pulse with a center shifting linearly over time. For this simulation, a few assumptions are made about the waveforms. The initial waveform was assumed to be Gaussian in the spatial dimension and the temporally. Therefore, we assume the intensity profile of the waveform entering the system to be

$$I(y, t) = e^{-\left(\frac{y^2}{r_0^2} + \frac{t^2}{r_t^2}\right)} \quad (1)$$

where $r_0 = 2$ mm and $r_t = 500$ fs. From this assumption made on r_t , the full-width half maximum (FWHM) of the pulse temporally is 832.5 fs ($2r_t\sqrt{\ln(2)}$). Figure 3 contains an illustration of the

The phase mask actually sees a Fourier transform of this waveform with respect to the time dimension. This is not a problem, however. We may then take the Fourier transform of this waveform with respect to time to get $I(y, \omega)$ when generating our phase.

For the final waveform, we make the assumption that it follows the equation

$$I_F(y, t) = c * e^{-\left(\frac{(y-vt)^2}{r_f^2} + \frac{t^2}{r_{tf}^2}\right)} \quad (2)$$

where $r_f = 40$ μ m and $r_{tf} = 1000$ fs. The FWHM of the pulse in temporal dimension is 1.665 ps, and the FWHM of the pulse in the y-spatial dimension is 66.6 μ m. c is a constant chosen so that the output pulse of the system has the same energy as the input pulse. Choosing the constant this way is necessary in order to get the best convergence of the initial waveform to the final waveform. The variable v , which controls the extent of the pulse movement, was chosen to be a value which gave good spatial movement of the pulse, but also one that was realizable with little error.

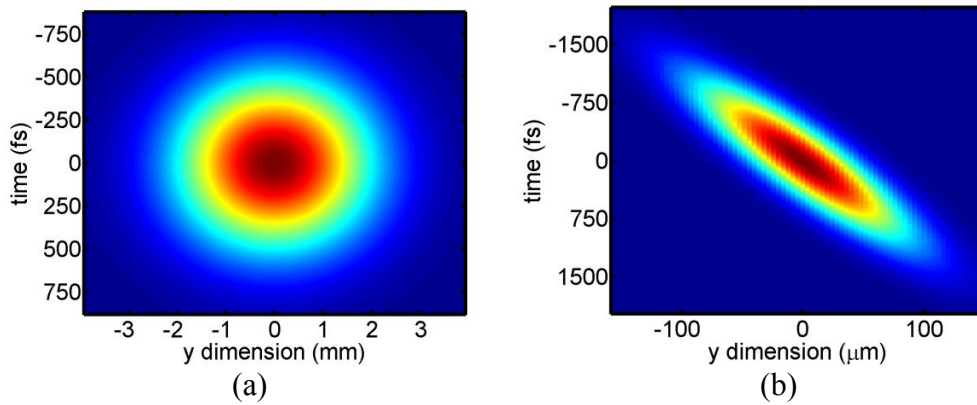


Figure 3. (a) Contour of initial intensity profile, (b) contour of ideal final intensity profile.

For both waveforms, we used a grid of 1024x1024 points. The spatial extent of the phase mask is 10 mm. The center wavelength of the initial waveform is 800 nm, which corresponds to near infrared. The focal length of the lens is 50 mm. The spatial extent of the mask (d), the center wavelength (λ), and the focal length (f) all determine the spatial resolution in the y dimension of the final waveform at the second grating. The spatial resolution is $\lambda f/d = 4 \mu\text{m}$. The spatial resolution is found from Fourier optics theory.^[4] The final waveform is a 1024x1024 grid, and the distance between the sampled amplitude points of the final waveform in the y dimension is the spatial resolution. The spatial resolution physically limits how small spatially the final waveform can be.

Once we implemented these assumptions, we needed to find the phase $\varphi(y,w)$. Once we find the right phase, Fourier transforming the initial Fourier modulus profile at the phase mask ($\sqrt{I(y, \omega)}$) multiplied by $e^{\varphi(y,w)}$ will result in the final Fourier modulus profile $\sqrt{I_F(y, t)}$. This will result in the beam shaping that we want if we apply the phase we find to the pulse at the phase mask.

There were a few algorithms available to find the necessary phase for the spatiotemporal shaping we desired. Eventually, we settled on the input-output algorithm, because it was a simple algorithm and it could be fine-tuned by using changing a parameter, β , for slightly better convergence. The equations for the input-output algorithm are shown below:^[6]

$$g_k(y, \omega) = \sqrt{I(y, \omega)} * \exp[i * \varphi[g_{k-1}'(y, \omega)]] \quad (3)$$

$$G_k(u, t) = F\{g_k(y, \omega)\} \quad (4)$$

$$G_k'(u, t) = (\sqrt{I_F(u, t)} + \beta|\sqrt{I_F(u, t)} - |G_k(u, t)||) * \exp\{i * \varphi[G_k(u, t)]\} \quad (5)$$

$$g_{k+1}'(y, \omega) = F^{-1}\{G_k'(u, t)\} \quad (6)$$

The starting phase distribution for the first iteration ($\varphi[g_0'(y, \omega)]$) was 0 for all the points. In Figure 4, the procedure and algorithm are illustrated in block diagram form.

Once we chose our algorithm, we needed to find the value for β which gave the best convergence results. Also, we needed to decide on a value for v in the equation for the final waveform given above.

RESULTS

First, we proceeded to determine a good value for v for our final waveform. We used the input-output algorithm with $\beta = 0$ on the final waveform with different values of v , ranging from 0.015 $\mu\text{m}/\text{fs}$ to 0.150 $\mu\text{m}/\text{fs}$. Table I gives the amplitude mse (mean squared error) and intensity mse for each v chosen after 100 iterations. The amplitude mse and intensity mse are defined as

$$\text{Amplitude MSE} = \frac{\sum_{y_i} \sum_{t_i} |\sqrt{I_G(y, t)} - \sqrt{I_F(y, t)}|^2}{\sum_{y_i} \sum_{t_i} |\sqrt{I_F(y, t)}|^2} \quad (7)$$

$$\text{Intensity MSE} = \frac{\sum_{y_i} \sum_{t_i} |I_G(y, t) - I_F(y, t)|^2}{\sum_{y_i} \sum_{t_i} |I_F(y, t)|^2} \quad (8)$$

where $I_G(y, t)$ is the intensity profile of the final generated waveform. One percent error was a good goal to set for the convergence of this waveform and we wanted to keep v somewhat less than the speed of light, so we decided that $v = 0.075 \mu\text{m}/\text{fs}$ (1/4 the speed of light) was a good choice for v . The center of the final waveform should therefore move approximately 124.9 μm ($0.075 \mu\text{m}/\text{fs} * 1665 \text{ fs}$) in the time FWHM region of the pulse. This is significant movement, considering that the FWHM of the pulse in the y spatial dimension is 66.6 μm

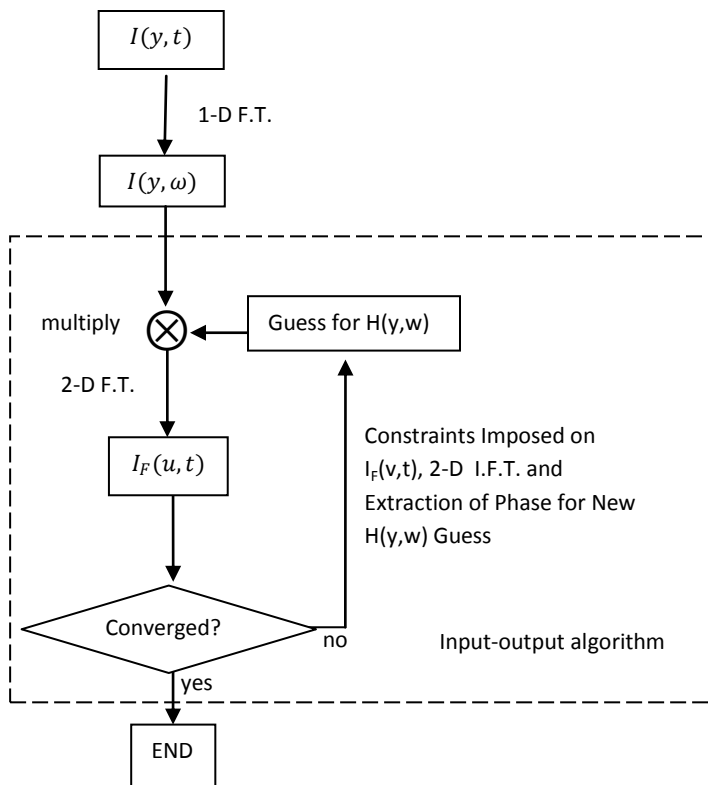


Figure 4. Block diagram of procedure for simulation.

In a similar manner, we decided the best choice for β . Using the value $v = 0.075 \mu\text{m}/\text{fs}$, we experimented with different values of β for the best convergence. From our results (Table II), the best choice was $\beta = 0.1$.

Table I. Amplitude and intensity mse after 100 iterations of input-output algorithm with $\beta = 0$, for the final waveform with varying v .

v ($\mu\text{m}/\text{fs}$)	Intensity mse	Amplitude mse
0.015	0.02892	0.01814
0.030	0.04900	0.02920
0.045	0.04050	0.02193
0.060	0.01499	0.01428
0.075	0.01485	0.01190
0.090	0.06151	0.04223
0.105	0.09193	0.07122
0.120	0.13181	0.11124
0.135	0.17572	0.15601
0.150	0.23022	0.20498

Table II. Amplitude and intensity mse after 100 iterations of input-output algorithm with varying β , for final waveform with $v = 0.075$ $\mu\text{m}/\text{fs}$.

β	Intensity mse	Amplitude mse
0	0.03690	0.02001
0.1	0.01060	0.00743
0.2	0.01855	0.01140
0.3	0.01896	0.01251
0.4	0.02162	0.01561
0.5	0.01934	0.01870
0.6	0.01377	0.01550
0.7	0.01417	0.01701
0.8	0.00741	0.01719
0.9	0.01370	0.03188
1.0	0.00823	0.03936

We used 5000 iterations of the input-output algorithm with $\beta = 0.1$ to achieve an amplitude mse (mean squared error) of 0.0063 and an intensity mse of 0.0076 for the final waveform.

The amplitude mse and the intensity mse are plotted in Figure 5. Notice that the mse goes down rather quickly at first, and then levels off as the number of iterations increases. Both mses are very low.

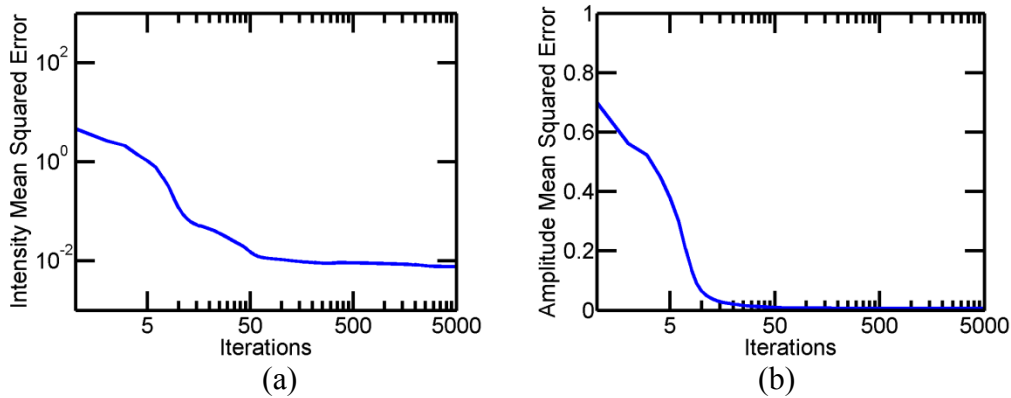


Figure 5. (a) Intensity mean squared error versus iterations, and (b) Amplitude mean squared error versus iterations.

A few spatial profiles of the final waveform generated at specific times are also displayed (Figure 6), as well as a contour plot of the generated final waveform (Figure 7). The waveform moves significantly throughout the pulse duration, which is very good. The intensities at $t = -834.96$ fs and 834.96 fs are smaller than the intensity at $t = 0$ fs by a factor of 2. Those who pursue future work in this area may wish to achieve to a final waveform with more spatial movement, or with a more constant intensity throughout the duration of the pulse, or both. Also, the final generated waveform is not very smooth, so further research may need to be done in order to achieve better convergence.

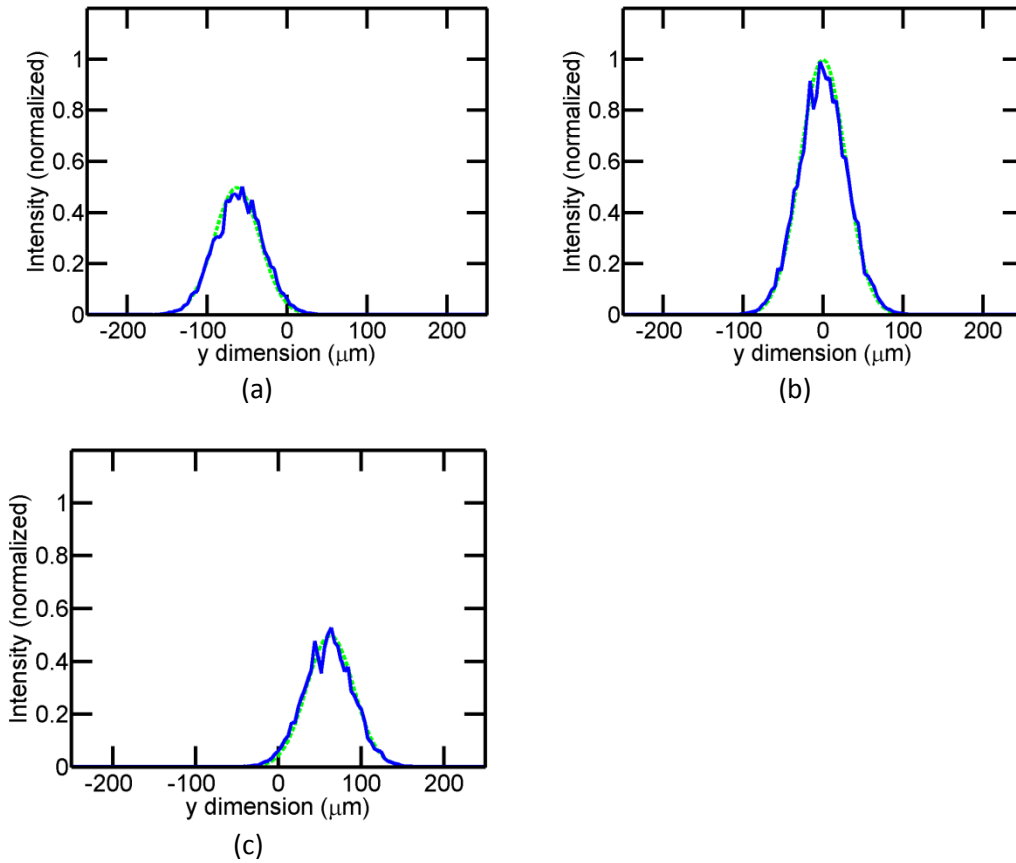


Figure 6. (a) Spatial intensity profile at $t = -834.96$ fs, (b) spatial intensity profile at $t = 0$ fs, (c) spatial intensity profile at $t = 834.96$ fs. The solid line represents the final waveform and the dashed line which represents the ideal waveform.

If this system like this is to be implemented, further research will need to be done about the pulse shaping system described in Figure 1. This research will need to look into the actual frequency distribution along the x dimension, and the spatial distribution along the y dimension, in order to place the phases generated from a simulation such as this in the proper positions in the phase mask.

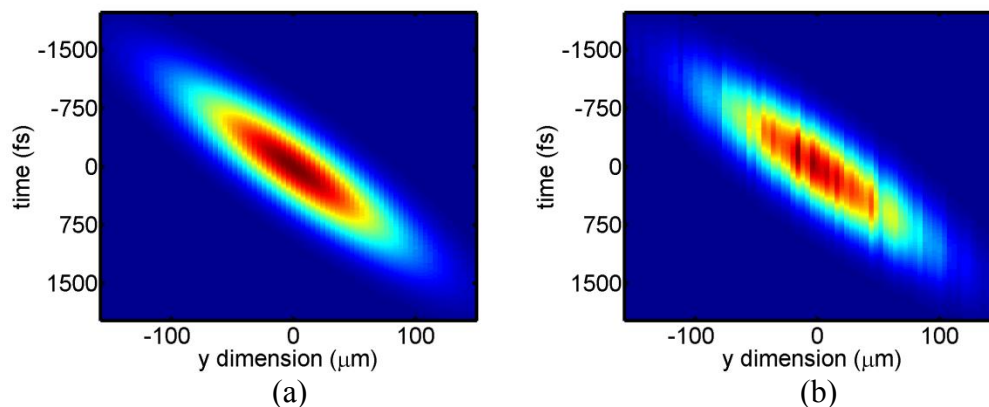


Figure 7. (a) Contour plot of ideal final waveform (b) contour plot of final generated waveform.

CONCLUSION

The spatiotemporal shaping of a spatially Gaussian pulse to a Gaussian pulse with a varying spatial center has been explored. Reasonable convergence has been achieved for a phase mask to implement this type of pulse shaping when placed in a pulse-shaping system. However, the amount of spatial movement achievable for the final pulse is limited. A possible use of the waveform such as the one we generated could be used as an ultrafast scanner.

ACKNOWLEDGEMENTS

One of the authors (JD) would like to thank Dr. Liu and Peng Li for aiding him in this project, especially in helping to generate good results for this paper and correcting some mistakes in the simulation. Thanks to Haifeng Li for providing good guidance to JD throughout the REU. Also, thanks to Kebin Shi and Qian Xu for answering many questions JD had throughout the REU program and for proofreading this paper. JD also thanks Jason Okerman, an REU participant last year, for his thoughtful input and discussion on this project. Also, thank you to JD's family and past teachers who have helped him in his career thusfar. Lastly, thanks to the National Science Foundation, who supported this report. This material is based on work supported by the National Science Foundation under Grant No. EEC-0755081.

REFERENCES

- 1 F.M. Dickey, "Laser Beam Shaping," *Optics and Photonics News*, pp. 31-35, April 2003.

- ² A.M. Weiner and A.M. Kan'an, "Femtosecond Pulse Shaping for Synthesis, Processing, and Time-to-Space Conversion of Ultrafast Optical Waveforms," *IEEE Journal of Selected Topics in Quantum Electronics* 4(2), pp. 317-329, 1998.
- ³ M.M. Wefers and K.A. Nelson, "Space-Time Profiles of Shaped Ultrafast Optical Waveforms," *IEEE Journal of Quantum Electronics* 32(1), pp. 161-172, 1996.
- ⁴ O.K. Ersoy, *Diffraction, Fourier Optics and Imaging*, Hoboken, New Jersey: John Wiley & Sons, 2007.
- ⁵ R.M. Koehl, T. Hattori, and K.A. Nelson, "Automated spatial and temporal shaping of femtosecond pulses," *Optics Communications* 157, pp. 57-61, 1998.
- ⁶ R. Wu et. al, "Extended algorithm for the design of diffractive optical elements around the focal plane," *Applied Optics* 46(23), pp. 5779-2783, 2007.
- ⁷ A.V. Oppenheim and A.S. Willsky, *Signals and Systems*, 2nd ed, Upper Saddle River, New Jersey: Prentice-Hall, 1996.

INVESTIGATION OF DYNAMIC CHARACTERISTICS OF PIEZOELECTRIC T-BEAM ACTUATORS

Siddharth Sonti^{*}, Andrew Hirsh⁺, and Srinivas Tadigadapa[#]

⁺Department of Mechanical Engineering

[#]Department of Electrical Engineering

The Pennsylvania State University, University Park 16802

*Undergraduate student of

Department of Electrical and Electronics Engineering

Manipal Institute of Technology

Manipal University

India

ABSTRACT

This research involves the study of novel monolithic PZT beam actuators with a T-shaped cross section. The cantilevered T-beam structure exhibits both in-plane and out of plane bending motion by the application of electric field in selective parts of the structure. The devices have been optimized for tip deflection. The theoretical resonant frequencies were calculated and experimentally verified using a precision impedance analyzer. Experiments were performed in vacuum and in variable pressure conditions and the various dynamic parameters were extracted. A considerable increase in the Quality-factor (Q -factor) of the beams was observed when the testing was performed in vacuum. The experimental values of the resonant frequency were found to deviate from the theoretical value by minimum of 0.57% to a maximum of 21%. The measured Q -factor ranges from 33 to 116.

⁺ Graduate Mentor, Department of Mechanical Engineering

[#] Faculty Mentor

INTRODUCTION

Piezoelectricity is the ability of some materials (notably crystals and certain ceramics) to generate an electric potential in response to applied mechanical stress. The piezoelectric effect is reversible in that materials exhibiting the direct piezoelectric effect (the production of electricity when stress is applied) also exhibit the converse piezoelectric effect (the production of stress and/or strain when an electric field is applied). This study involves the use of the converse piezoelectric effect. Piezoelectric actuators are used for many applications, including micro positioning systems, camera auto-focus lenses, structural vibration control, and control surfaces, and control surfaces. Most piezoelectric actuators use Lead Zirconate Titanate (PZT) because it provides large piezoelectric and electromechanical coupling factors. Typically, the strain produced in PZT is $\sim 0.1\%$ and therefore must be amplified to produce reasonable motion.

Figure 1 schematically illustrates the novel monolithic PZT beam actuators. Cantilevered T-shaped cross-section PZT actuators with bottom and top (web) electrodes, and right, and left flange electrodes, can bend in-plane and out of plane. Bimorph actuation in both axes is achieved by selectively actuating parts of the structure i.e., by applying voltages to either the left or right flange electrodes (for in-plane motion) or by applying voltages to the web electrode (for out-of-plane motion). Figure 2 shows an optical image of such a cantilevered PZT T-shaped actuator.

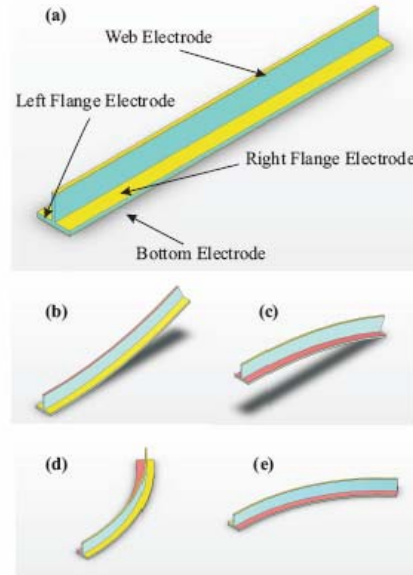


Figure 1. T Beam Actuator concept (a)As fabricated, and deflected shapes when voltage is applied between (b)flanges and bottom electrode(c)web and bottom electrodes, d)left flange and bottom electrodes and (e)right flange and bottom electrodes.¹

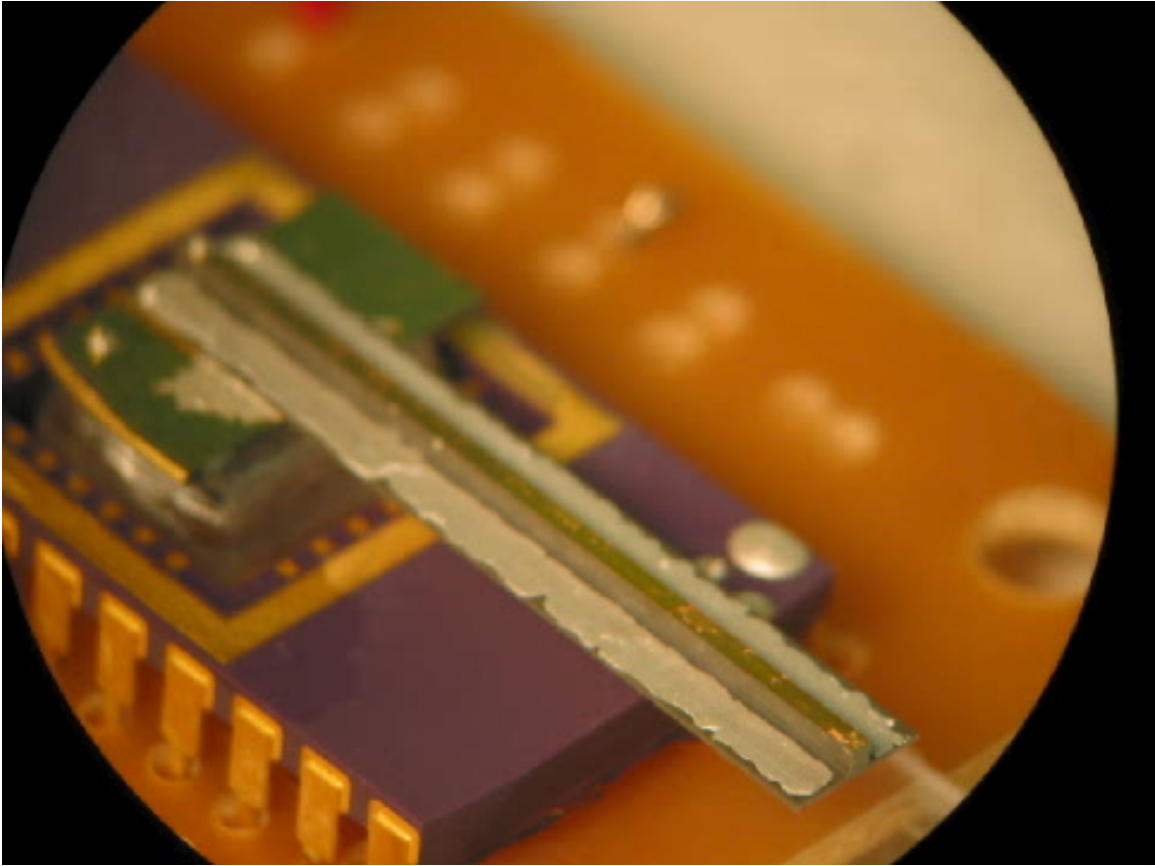


Figure 2. Fabricated and packages PZT T beam actuator

These high performance T-beam actuators are currently being designed for nano air-vehicles application. By maximizing the tip deflection and blocking force, these T-beams could be used as wings for nano air-vehicles. Nano air-vehicles (NAV), defined as weighing less than 10 grams with wingspans less than 7.5 cm, have yet to be flown. Currently, NAV scale actuators and wings with requisite range of motion, power, and efficiency do not exist. The focus of this research is the study of the dynamic characteristics of these T-beam actuators. For maximum displacement the piezoelectric structure must be excited with the required voltage at its resonant frequency. Under forced oscillation conditions, any structural system [oscillates](#) with large (maximum) [amplitude](#) at certain [frequencies](#), known as the system's resonant frequencies. At these frequencies, even small [periodic](#) driving forces can produce large amplitude vibrations, because the system stores vibrational energy. This study involves experimentally verifying the resonant frequencies which have been theoretically calculated. This is done with the help of a precision impedance analyzer. The ultimate goal is to make a micro scale device to act as the actuators of the wings of NAV. This project is a proof of concept and the testing is performed at a mesoscale. The

devices were initially tested in normal atmospheric pressure conditions and then later tested in vacuum and variable pressure conditions.

MANUFACTURING PROCESS

A 1 inch by 1 inch by 1 mm block of Navy 1 type 4 PZT obtained from Boston Piezooptics Inc. was used. A stair stepped structure was cut out using a precision dicing saw as shown in Fig. 3 below. The top and the bottom gold electrodes were vacuum evaporated onto it. The left flange and right flange electrodes were deposited by painting conductive epoxy in these areas. The T-beams were then packaged and wire bonded on to a chip carrier capable of being placed into a breadboard for testing purposes.

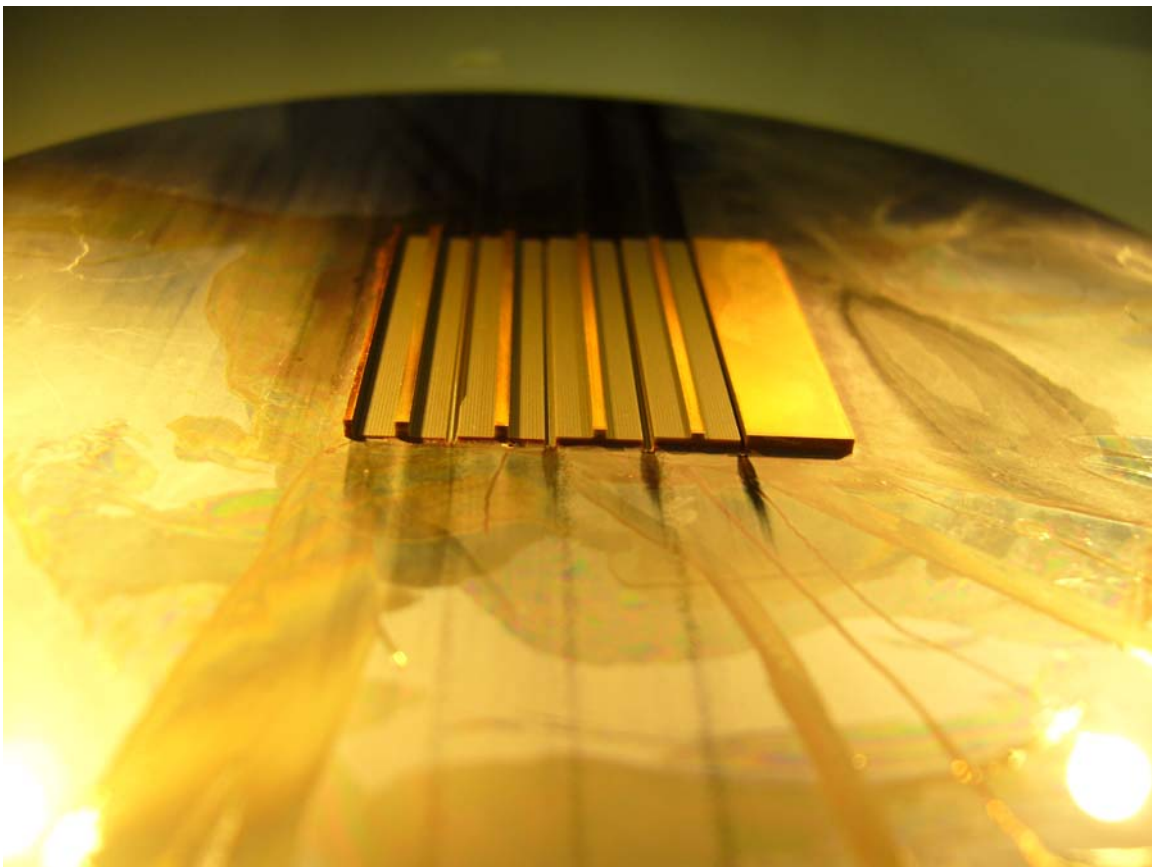


Figure 3. Manufacturing process on the precision dicing saw

Table. Physical Properties of PZT²

Property	Boston piezo-optics Navy Type I (PZT-4)
d_{33} ($\times 10^{-12}$ m/V)	295
d_{31}	-122
Density (Kg/m ³)	7600
Young's Modulus ($\times 10^{10}$ M/m ²)	7.8
Curie Point (°C)	325

MATHEMATICAL MODELING

A theoretical model has been developed to optimize the performance of the T-beam actuator. The T-beam actuator with web and flange electrodes is modeled as a cantilever beam using Euler-Bernoulli theory. A uniaxial electric field is assumed throughout the thickness of the actuator. The longitudinal and transverse direction displacements are denoted by u , w respectively. Figure 4 shows the various geometric and deflection parameters used in the model.

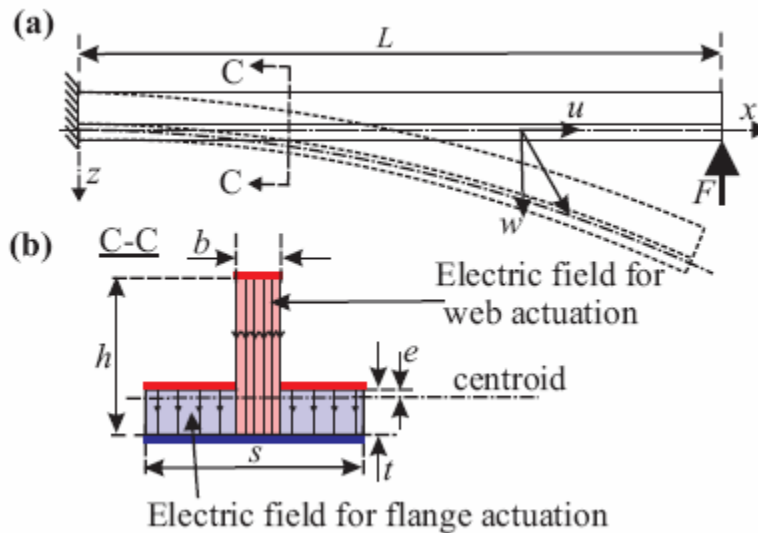


Figure 4. T-beam model: (a) the initial and deflected shape and (b) cross section¹

An expression for the electric enthalpy of the cantilever beam system is written and solved using the appropriate boundary conditions to obtain the deflections as a function of the various beam parameters¹. This model allows for the fabrication of actuators with optimized structural dimensions.

Dynamic Testing

The resonance frequency of the cantilevered T-beam structures was measured using an impedance analyzer as discussed earlier. The impedance analyzer was set-up to measure the impedance and the phase as a function of frequency. Four beams were tested for their resonance behavior in air and in vacuum. Scan ranges were appropriately chosen to span the resonance frequency for each resonator.

Figures 5 and 6 show the typical impedance and phase variations for the cantilever beams at resonance.

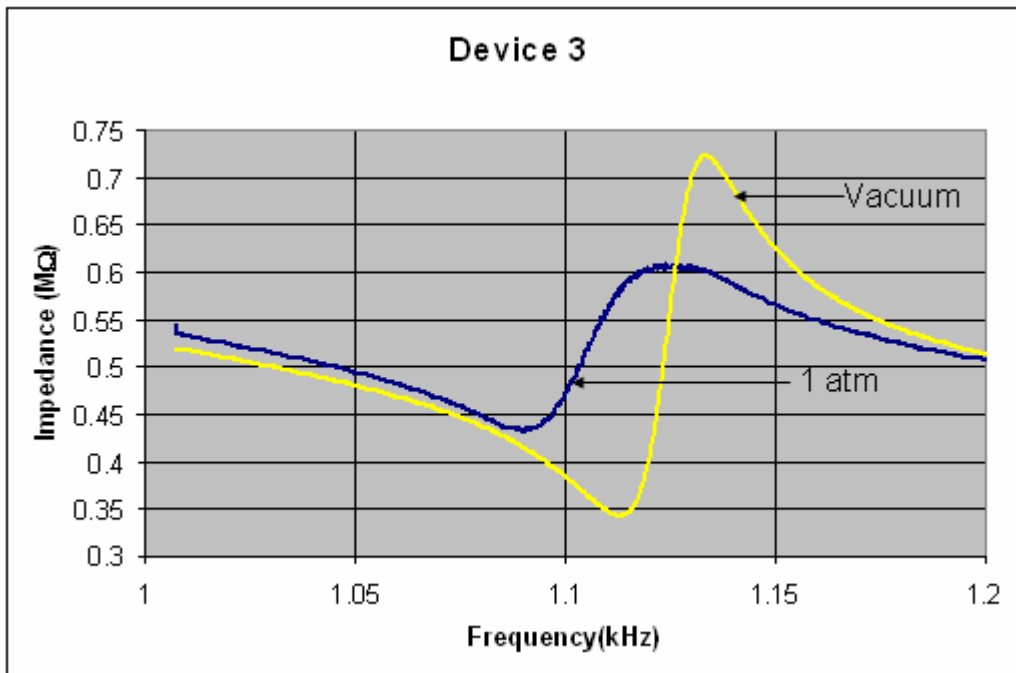


Figure 5. Graph of Impedance vs. Frequency. Measurements have been taken in Vacuum(10^{-6} Torr) and at 1 atm.

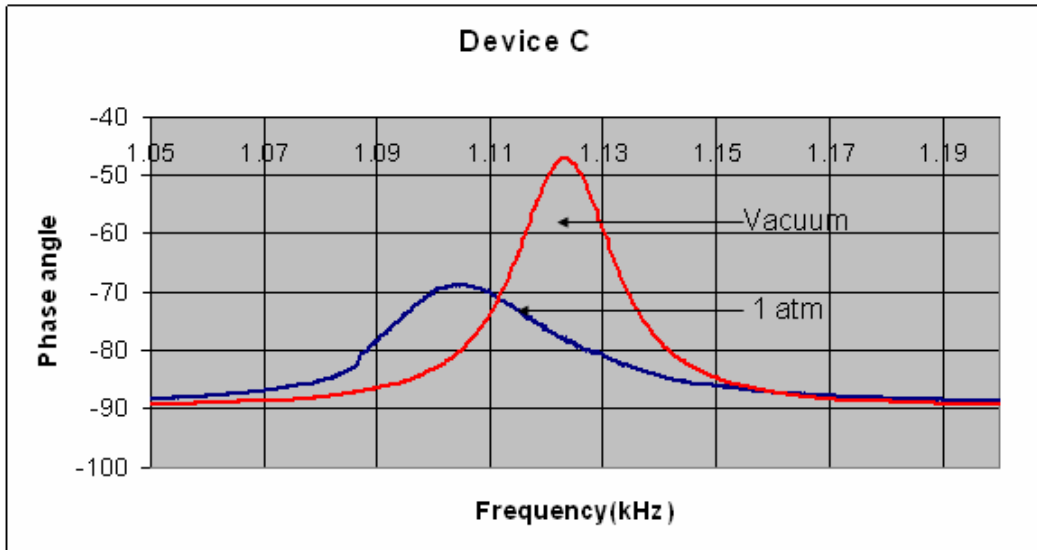


Figure 6. Graph of Phase angle vs. Frequency. Measurements have been taken in Vacuum(10^{-6} Torr) and at 1 atm.

The behavior of the cantilever beam at resonance can be approximated using the well known Butterworth van Dyke model. In this system, the electro-mechanical system is represented by the equivalent lumped electrical circuit parameters and in the configuration shown in Fig. 10.

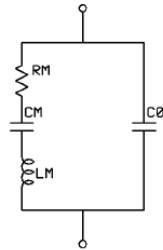


Figure 7. Butterworth van Dyke equivalent model of the cantilever resonator.

In this circuit R_M , C_M and L_M in series represents the motional arm of the resonator and C_0 is the parasitic capacitance. From the resonance curve, the motional and parasitic equivalent circuit parameters were obtained. This was done by using the Agilent 4294A impedance analyzer parameter extraction function.

The quality factor Q which determines the loss in the system can be computed using the following expression³:

$$Q = \frac{\omega L_m}{R_m}$$

where ω is the angular resonance frequency. The resonance frequency f_0 can be theoretically computed using the formula⁴

$$f_0 = \frac{4.71}{2\pi} \sqrt{\frac{EI}{\rho A}} \text{ (Hz)}$$

where the moment of inertia $I = I_{be} + I_{pe}$ and the area $A = A_b + A_p$. The expressions for I_{be} , I_{pe} , A_b , and A_p are listed in the Table below.

Region	Area	Moment of Inertia
Flange	$A_b = (s-b)t$	$I_{be} = \frac{1}{3}t(t^2 + 3e^2 - 3et)(s-b)$
Web	$A_p = bh$	$I_{pe} = \frac{bh^3}{12} + bh\left(\frac{h}{2} - t + e\right)^2$
where $e = \frac{1}{2} \frac{t^2s - t^2b + 2tbh - bh^2}{ts - tb + bh}$		

Tables 1 and 2 list the various resonance parameters extracted for the four resonators tested and are compared to the experimental results. A fairly good agreement between the experimentally observed and predicted resonance frequency is obtained. As expected the beams show a higher Q -factor in vacuum as compared to in atmosphere. This is mainly due to the reduction in dissipation arising due to the ambient air molecules.

Table 1. Device dimensions and calculated and measured resonance frequency in air.

Device	s μm	h μm	b μm	t μm	L mm	Resonance Frequency (Calc.) kHz	Resonance Frequency (Expt) kHz	Error %
1.	1012.8	1000	533.9	306.87	20.4	1.2733	1.266	0.57
2.	1028.0	1000	496.1	566.4	23.19	.90066	.782556	13.11
3.	4456.0	1000	709.5	523.5	19.34	1.0715	1.097	-2.37
4.	4462.0	1000	734.6	167.8	18.98	1.4854	1.177	20.76

Table 2 . Calculated and measured resonance frequency in Vacuum (10^{-6} Torr)

Device	Resonance Frequency f (kHz)	$\omega=2\pi f$	R_m ($M\Omega$)	C_m (pF)	L_m (kH)	C_0 (pF)	Q -Factor
1.	1.264	7942	0.52	3.10	5.14	252.5	79
2.	0.765	4807	1.82	1.01	44.0	70.0	116
3.	1.130	7100	0.64	3.87	5.21	283.7	58
4.	1.060	6660	1.20	3.76	6.01	243.5	33

CONCLUSION

The results of this investigation namely the dynamic characteristics of the PZT T-beam actuator and the results from static deflection measurements provides important information relating to the overall performance and optimization of these actuators and will be the basis for the eventual realization of NAV wings actuators.

ACKNOWLEDGMENTS

As the first author, I would like to thank my faculty mentor Dr. Srinivas Tadigadapa for his guidance and support. I would like to thank Andrew Hirsh for providing me with machined and packaged devices and for all his guidance. I would also like to thank Kiron Mateti, Prasoon Joshi and Ashish Patwardhan for training me on various instruments utilized in the MEMS laboratory. This material is based on work supported by the National Science Foundation under Grant No. EEC-0755081.

REFERENCES

¹Hareesh K.R Kommepalli, Andrew Hirsh, Christopher D. Rahn, and Srinivas Tadigadapa “PIEZOELECRIC T-BEAM MICROACTUATORS’ ASME 2008 International Design Engineering Technical Conferences and Computers and Information in Engineering Conference 2008,Brooklyn,New York,USA DETC2008-49986

² www.bostonpiezooptics.com/?D=25

³Joel F. Rosenbaum, Resonator 1:basic Theory,pg-1,pg-393,“Bulk Acoustic Wave Theory and Devices” ARTECH HOUSE,INC 1988

⁴Robert D.Blevins, Straight Beams,pg-108 ”Formulas For Natural Frequency and Mode Shapes” KRIEGER Publishing Company 1984 edition

MEASUREMENT AND SIMULATION OF INTERDIGITAL CAPACITOR STRUCTURES WITH HIGH-PERMITTIVITY THIN FILMS

Clinton P. Scarborough*, Steve Perini[†], and Michael Lanagan[‡]

Department of Engineering Science and Mechanics
The Pennsylvania State University, University Park, PA 16802

*Undergraduate student of
Department of Electrical Engineering
Grove City College
Grove City, PA 16127

ABSTRACT

Electromagnetic simulation was found to show promise as a method to find the properties of a thin film with an interdigital capacitor (IDC) constructed on it. Given a film permittivity as measured by the fairly trusted split-cavity technique, IDC simulations were adjusted until the simulated results approached those measured from the physical sample. The simulation model was not fully perfected, as the capacitance showed a significant dependence on frequency, but it is hoped that future work will correct this. With the knowledge of the effects of different simulation parameters, the properties of the simulated film can be adjusted until the simulation results match the measured results, and the properties of the measured film can be inferred to match the design parameters of the simulated film.

INTRODUCTION

With the proliferation of wireless communication devices, each using a plethora of protocols and frequencies, the need for tunable components has increased. Barium strontium titanate (BST) thin films are undergoing much research due to their permittivity-field relationship. The permittivity of a BST film changes with the

[†]Technical Staff Mentor

[‡]Faculty Mentor

electric field through it, which makes it a candidate for use in components of electrically tunable circuits for radios in devices such as cell phones. Few techniques exist for measuring the properties of a thin film, and there is not much confidence in the existing characterization methods, especially for very thin films (less than $1\mu\text{m}$).

The most trusted method for characterizing the dielectric properties of thin films is the split-cavity method, which can be used for a sample consisting of nothing more than a substrate and film without electrodes. This requires a relatively large sample, however, and does not account for inconsistencies in film thickness or consistency over the entire film area. Another promising technique^[1] is the interdigital capacitor (IDC) method, which requires IDCs to be constructed on the sample by metallization and photolithography. The IDC is attached mounted in a controlled temperature stage and the S_{11} reflection parameter is measured with a network analyzer. The capacitance and loss can be calculated from the S_{11} data. Gevorgian *et al.*^[2] developed an analytical method relating IDC capacitance to the geometry and permittivity of the device, but this method has significant error for very thin films^[3] and does not account for dielectric loss. Simulations can be made by specifying the geometry of the device and the properties of the substrate and film, such as film permittivity. By adjusting the film properties until the simulated capacitance matches the measured capacitance, the properties of the film on the physical sample can be inferred to match those of the simulated film. This research aimed to validate the use of electromagnetic simulation for this purpose.

EXPERIMENTAL DESCRIPTION

INTERDIGITAL CAPACITORS (IDC)

An IDC is a coplanar structure consisting of two sets of interlocking fingers, as shown in Figure 1. The IDCs in this experiment were constructed on a magnesium oxide (MgO) substrate with a barium strontium titanate (BST) thin film. Much of the capacitance is due to the electric field in the film, because the permittivity of the BST is an order of magnitude or more larger than that of the substrate or the surrounding air. A method for specifying the geometry of an IDC was presented by^[2] and used by^[4] and^[1].

PHYSICAL MEASUREMENTS

The IDCs were measured using a network analyzer and probe station. Figure 2 shows a typical setup with a $250\mu\text{m}$ ground-signal probe contacting an IDC. A method outlined by Turpin^[4] was used to calculate capacitance from the S_{11} data returned by the network analyzer. The capacitance measurements were imperfect, however: the capacitance could change by a few percent depending on the point of probe contact. For example, in Figure 2, moving the probes horizontally would change the measured capacitance. Future work could investigate this phenomenon.

CST MICROWAVE STUDIO SIMULATION

CST Microwave Studio 2008 was used to construct and simulate a model of

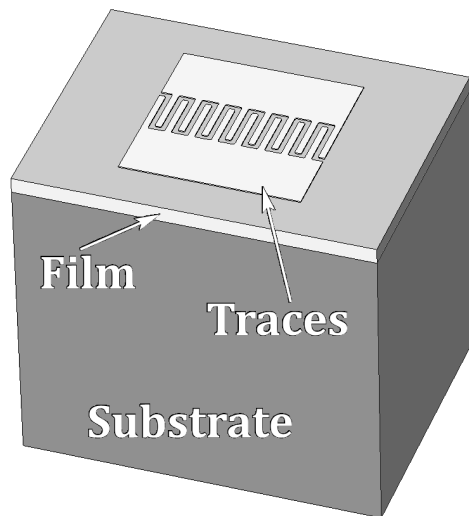


Figure 1: IDC Layout

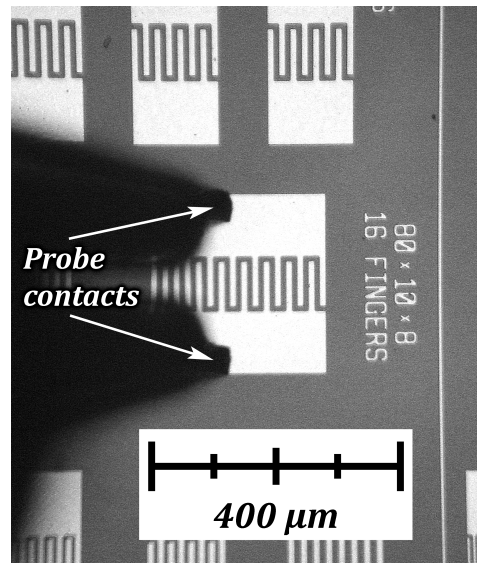


Figure 2: Typical Probe Setup

the IDC structure. All physical dimensions were defined to match the known geometry of the physical capacitors. The substrate was defined as a lossless dielectric, the film as a lossy dielectric, and the traces as a lossy metal. Because the simulation requires all material properties as inputs, the film permittivity was specified to be approximately the same as the results of Booth's split-cavity measurement of the sample under consideration. To apply test signals to the IDC, a discrete port was specified as shown by the line in the middle of Figure 3. The surrounding material was specified as a vacuum, and the electric field was assumed to be zero at the boundaries. The simulation ran over frequencies from 1GHz to 15GHz, but calculations and comparisons to physically measured values were made at 10GHz.

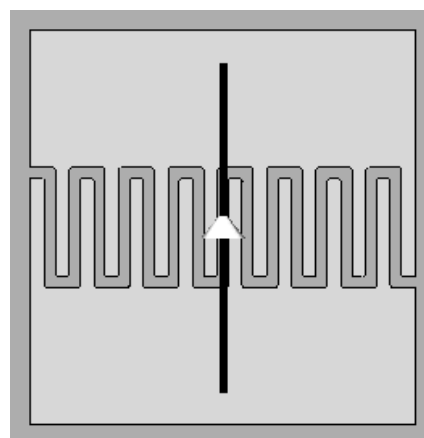


Figure 3: Port Setup

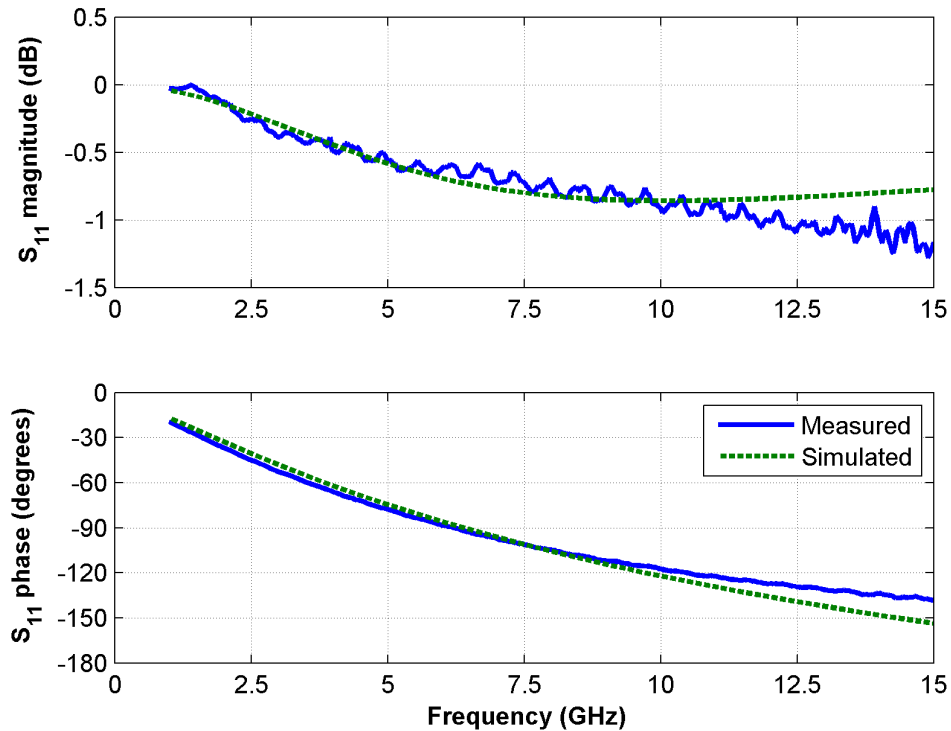


Figure 4: S_{11} Reflection Parameter Plot

One of the most significant simulation parameters was the mesh definition. The mesh determines the resolution of the results, so mesh blocks that were comparable or smaller than the feature sizes of the model were necessary, or else those parts of the structure would be ignored. The transient solver was used to obtain the S_{11} reflection parameter. The method that was used to calculate capacitance from the physically measured S_{11} data was used with the simulated S_{11} data.

RESULTS

MEASURED AND SIMULATED IDC RESULTS

Figure 4 shows both the measured and simulated S_{11} reflection parameter for an IDC on an MgO substrate with a 450nm BST film. These S_{11} data correspond to the capacitances shown in Figure 5. The measured capacitance is relatively independent of frequency, but the simulation still suffers from stray impedances that make the capacitance vary significantly with frequency, as shown in Figure 5. This phenomenon needs to be investigated in future work.

SUMMARY OF RESULTS AT 10GHZ

Table I compares the film permittivity results from the analytical model used by [1] and [4], the simulation, and the split-cavity measurement methods, and Table II

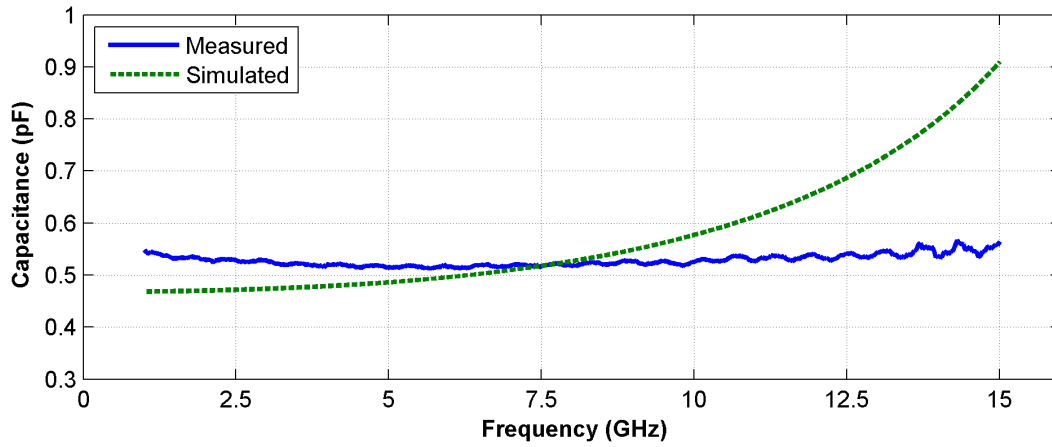


Figure 5: Measured and Simulated Capacitance versus Frequency

Table I: Permittivity Comparison at 10GHz

	$\epsilon_r(film)$	$\tan(\delta)$
Analytical	990	-
Simulated	472	0.100
Split Cavity	471	0.056

Table II: Measured and Simulated S_{11} at 10GHz

	$ S_{11} $	$\angle(S_{11})$	C
Measured IDC	-0.95 dB	-118°	0.53 pF
Simulated IDC	-0.86 dB	-122°	0.58 pF
Percent Difference	9.5%	-3.4%	-9.4%

compares S_{11} at 10GHz from the simulation and IDC measurements. From Table I, the approximate film permittivity found by the split-cavity technique was used for the simulations. As Table II shows, this resulted in less than a 10% difference between measured and simulated capacitances at 10GHz. With further tweaking of the simulation method, an IDC on a sample with unknown film permittivity could be measured, the film permittivity of a simulation could be adjusted until the capacitances matched, and the unknown permittivity could be inferred to be equal to that which was input to the simulation.

CONCLUSION

Although the simulation is not yet perfect, it shows promise as a method for characterizing the dielectric permittivity and loss of thin films. With more testing of the permittivity and loss parameters, the simulation could be tuned to yield S_{11} data that better match the measured data, and capacitances that are relatively independent of frequency. Matching measured and simulated data would give more confidence in simulation as a method of finding the permittivity of a thin film, and the method could be systematically used for characterizing thin films.

ACKNOWLEDGMENT

This material is based upon work supported by the National Science Foundation under Grant No. EEC-

REFERENCES

- ¹ R. Haney, Microwave Characterization of Oxide Thin Films, Master's thesis, The Pennsylvania State University, University Park, PA (2006).
- ² S. Gevorgian, T. Martinsson, P. Linner and E. Kollberg, "CAD models for multilayered substrate interdigital capacitors," vol. 44, pp. 896–904, 1996, doi: 10.1109/22.506449.
- ³ B. M. Booth, Interdigital Capacitor Method for the Characterization of Dielectric Thin Films, Bachelor's thesis, The Pennsylvania State University, University Park, PA (2007).
- ⁴ J. P. Turpin, O. Maksimov, M. Fanton, V. D. Heydemann, J. Robinson, S. Perini and M. Lanagan, "Tunable Interdigital Capacitors at Microwave Frequency," CI-CMT 2008, pp. 148–154 (2008).

EVALUATION OF CIRCUIT-BLOCKS FOR A ROBINSON MARGINAL OSCILLATOR

Michael Murphy* and Jeffrey L. Schiano#

Department of Electrical Engineering
The Pennsylvania State University, University Park, PA 16802

*Undergraduate student of
Department of Physics and Engineering
West Virginia Wesleyan College
Buckhannon, WV 26201

ABSTRACT

A Robinson marginal oscillator (RMO) is a low-cost instrument for observing nuclear quadrupole resonance (QR) transitions using continuous-wave (CW) excitation. A RMO consists of three circuit blocks: a voltage follower, a limiter, and an envelope detector. This paper describes the selection criteria and evaluation of circuits that implement these blocks.

INTRODUCTION

QR Spectroscopy

QR spectroscopy applications include explosive detection^[1], nondestructive evaluation of materials^[2], and characterization of pharmaceuticals.^[3] The physical basis for QR spectroscopy is the electrostatic interaction between the electric quadrupole moment of nuclei and the electric field gradient (EFG) generated by the surrounding electronic charge^[4]. Nuclei with an electric quadrupole moment possess intrinsic angular momentum and a magnetic moment. Because the intrinsic angular momentum is quantum number, the electrostatic interaction energy is quantized and the nuclei have preferred orientations with respect to the principal axis of the EFG tensor. The energy level associated with each preferred orientation is not sharp owing to strains and impurities within a sample. As a result, the energy difference between preferred orientations is described by a

Faculty Mentor

Lorentzian distribution. For nitrogen-14 nuclei, the center of the Lorentzian distribution, or transition frequency, can range from 500 kHz to 5 MHz, depending on the nature of the chemical bonds formed by nitrogen within a molecule. The full-width half-maximum of the Lorentzian distribution for nitrogen-14 QR transitions is on the order of 1 kHz.

The electric quadrupole interaction can be observed using either pulsed or CW excitation.^[5] In both methods the sample is placed near a probe coil that produces a time varying magnetic field at a QR transition frequency. In pulsed spectroscopy, the RF magnetic field is gated to produce a series of pulses that perturb the orientation of the nuclei. In the interval between RF pulses, the rotation of the nuclear magnet moments induces a voltage across the probe coil that reveals the presence of the quadrupole interaction. In a CW experiment, the probe coil is part of a tuned circuit that forms an oscillator. As the frequency of the oscillator is swept through a quadrupole transition frequency, the amplitude of oscillation decreases as the nuclei absorb energy from the circuit.

In pulse spectroscopy the bandwidth of the RF pulse is typically larger than the Lorentzian distribution of the QR transition, and so all the nuclei are excited. In contrast, CW spectroscopy uses a nearly monochromatic excitation source that excites only a small fraction of the nuclei within the Lorentzian distribution. As a result, the signal-to-noise ratio per unit time for pulsed experiments is significantly greater than that for CW experiments. On the other hand, CW spectroscopy requires significantly lower excitation power and correspondingly less expensive instrumentation. Furthermore, the small amplitude RF magnetic fields in CW spectrometers are desirable in certain applications such as contraband detection where large fields are undesirable for safety reasons.

Robinson Marginal Oscillator

Figure 1 shows a block diagram of a Robinson marginal oscillator.^[6] A cylindrical sample is placed within a solenoidal coil of self-inductance L and self-resistance R . When the frequency of the RF magnetic field generated by the coil approaches a QR transition frequency, the nuclei absorb energy and increase the resistance looking into the probe coil by δR . The variable capacitance C allows the experimenter to sweep the frequency of oscillation through a QR transition. The voltage $v_T(t)$ across the tank circuit is observed using a voltage follower whose input impedance is much greater than that of the tank circuit so that it does not affect either the frequency or amplitude of oscillation. Changes in the amplitude of oscillation are observed using the envelope detector. As these changes are small, they are measured using a lock-in amplifier that is not shown in Figure 1. The limiter is a memoryless nonlinear function that supplies a feedback current through the resistance R_f to sustain a steady-state oscillation. The input-output characteristics of the limiter determine the sensitivity of the envelope output voltage with respect to changes in δR , as well as the amplitude and frequency of oscillation.^[7] The circuit is called a Robinson oscillator because separate circuit blocks are used to implement the voltage follower and limiter.

The term marginal refers to the fact that the characteristics of the limiter are chosen so that small changes δR yield large changes in the envelope voltage.

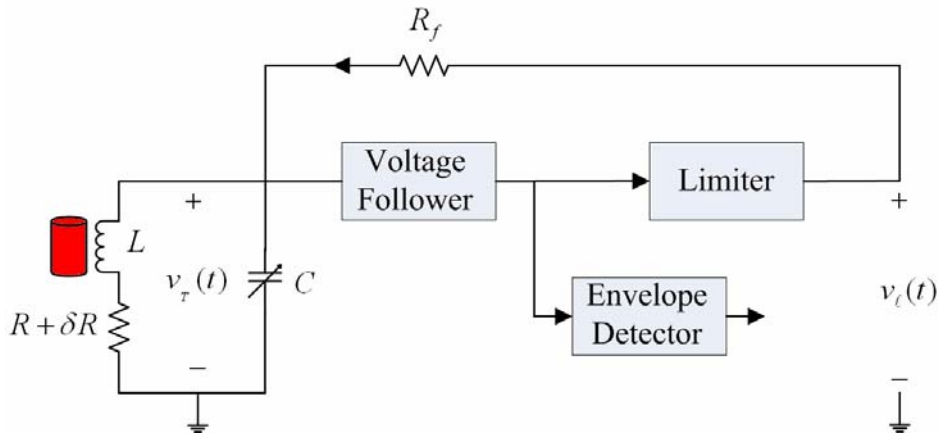


Figure 1: Robinson marginal oscillator

Voltage Follower

The purpose of the voltage follower is to obtain a measurement of the voltage across the tank circuit without disturbing either the frequency or amplitude of oscillation. The frequency of oscillation is approximately

$$\omega_* = \frac{1}{\sqrt{LC}}. \quad (1)$$

At the frequency of oscillation ω_* , the impedance looking into the tank circuit from the voltage follower is approximately

$$Z_{in}(\omega_*) = \frac{L}{RC}. \quad (2)$$

For a nitrogen-14 CW spectrometer operating at the 3.308 MHz transition frequency of hexamethylenetetramine (HMT)^[8], typical values for R , L , and C yield an input-impedance Z_{in} of approximately 35 k Ω . Ideally, the voltage follower presents an input-impedance that is an order of magnitude larger than 35 k Ω at 3.308 MHz.

In order to assess the effect of the voltage follower on the tank circuit, it is convenient to measure the Quality factor (Q-factor) of the tank circuit with, and without, the voltage follower connected. The Q-factor is defined as^[9]

$$Q = \frac{\omega_* (\text{time-average energy stored in tank circuit})}{(\text{energy loss per second in tank circuit})}. \quad (3)$$

When the tank circuit in Figure 1 is disconnected from the voltage follower, the Q-factor is

$$Q = \frac{\omega_* L}{R} = \frac{\omega_*}{3 \text{ dB bandwidth}}, \quad (4)$$

where the 3 dB bandwidth is that of the transfer function between the current in the feedback resistance R_f and the tank voltage $v_T(t)$.

When connected across the tank circuit, the voltage follower input appears as a resistance R_i in parallel with a capacitance C_i . From equations (3) and (4), the effect of R_i is to decrease the Q-factor by increasing the energy loss per second. From equation (1), the effect of C_i is to reduce the frequency of oscillation by increasing the overall capacitance connected in parallel with the probe coil.

Envelope Detector

The envelope detector reveals changes in the oscillation amplitude. The tank circuit voltage is represented as

$$v_T(t) = v_{\text{env}}(t) \cos \omega_* t, \quad (5)$$

where $v_{\text{env}}(t) > 0$ represents the envelope of the oscillation that varies in time with changes in δR caused by sweeping the oscillator frequency across a QR transition frequency. Two methods are explored for recovering the envelope voltage $v_{\text{env}}(t)$.^[10] The first method rectifies the tank voltage $v_T(t)$ and passes the resulting half-wave signal through a lowpass filter with a cutoff frequency well below ω_* . The output of the lowpass filter is a good approximation to $v_{\text{env}}(t)$. As the envelope voltage may be on the order of 100 mV or less, the rectifier is implemented using a precision diode constructed from a current-feedback operational amplifier.

The second method recovers the envelope using a much simpler circuit based on a square-law detector. The voltage across the tank circuit is applied to the gate of a junction field effect transistor (JFET). The resulting drain current is proportional to the square of the gate current. Lowpass filtering the drain voltage provides a measure of the square of the envelope voltage.

Limiter

In order to sustain a steady-state oscillation, the gain provided by the limiter circuit must exactly match the losses present in the circuit. The limiter implements a memoryless nonlinearity whose gain at the frequency of oscillation is a function of the amplitude of the sinusoid driving the limiter. The shape of the

nonlinearity determines the sensitivity of the envelope voltage $v_{env}(t)$ to changes δR in the resistance of the inductor caused by nuclei absorbing energy^[7]

$$S_R^{env} = \frac{\frac{\Delta v_{env}}{v_{env}} \times 100}{\frac{\delta R}{R} \times 100} = \frac{\partial v_{env}}{\partial R} \frac{R}{v_{env}}. \quad (6)$$

The relationship between the limiter input voltage $v_T(t)$ and output voltage $v_\ell(t)$ is shown in Figure 2 for two different limiter characteristics. Figure 2(A) shows a hard limiter characterized by a single parameter $v_{\ell o}$ that determines the amplitude of oscillation. The hard limiter yields a sensitivity $S_R^{env} = -1$. In other words, a 1 % increase in tank resistance produces a 1% decrease in envelope voltage. Figure 2(B) shows a soft limiter characterized by two slopes, g_a and $g_b < g_a$, and a threshold voltage v_t at which the slope of the limiter transfer characteristic changes as a function of the limiter input voltage. By appropriately choosing the parameters g_a , g_b , and v_t , it is possible to achieve a desired amplitude of oscillation with a sensitivity $|S_R^{env}|$ in excess of 10.^[7]

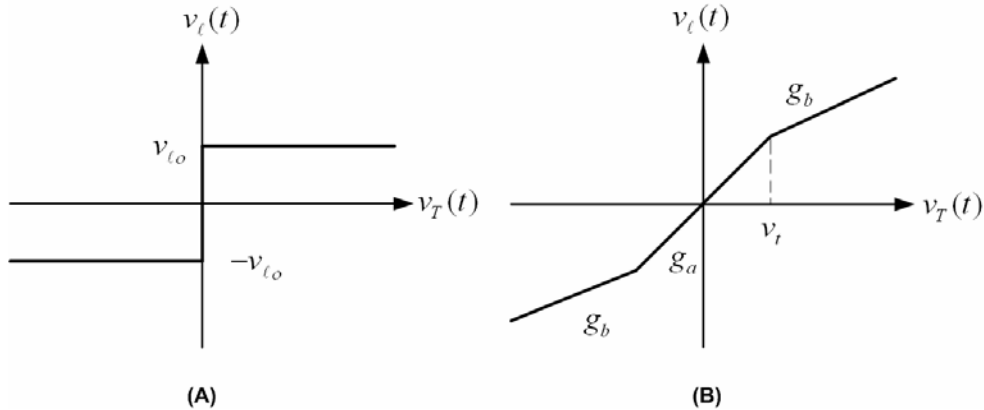


Figure 2: (A) Hard and (B) soft limiter characteristic curves

EXPERIMENTAL DESCRIPTION

Voltage Follower Circuits

This paper considers two different circuits for implementing a voltage follower. Figure 3 shows the first circuit that uses an operational amplifier configured as a unity-gain voltage follower. As the circuit must operate at frequencies up to 5 MHz, a current feedback amplifier is used to obtain a wide operating bandwidth. The current feedback amplifier requires a resistance in the feedback loop to achieve a stable circuit, and the value of this resistance is specified by the manufacturer. Two operational amplifiers are considered, and

differ by their unity gain bandwidth and input impedance at the non-inverting input. Table I summarizes these parameters for the two operational amplifiers used in the experiment.

Table I. Comparison of operational amplifier specifications

DEVICE	Unity Gain Bandwidth	R_i	C_i
AD8001	880 MHz	10 M Ω	1.5 pF
AD811	140 MHz	1.5 M Ω	7.4 pF

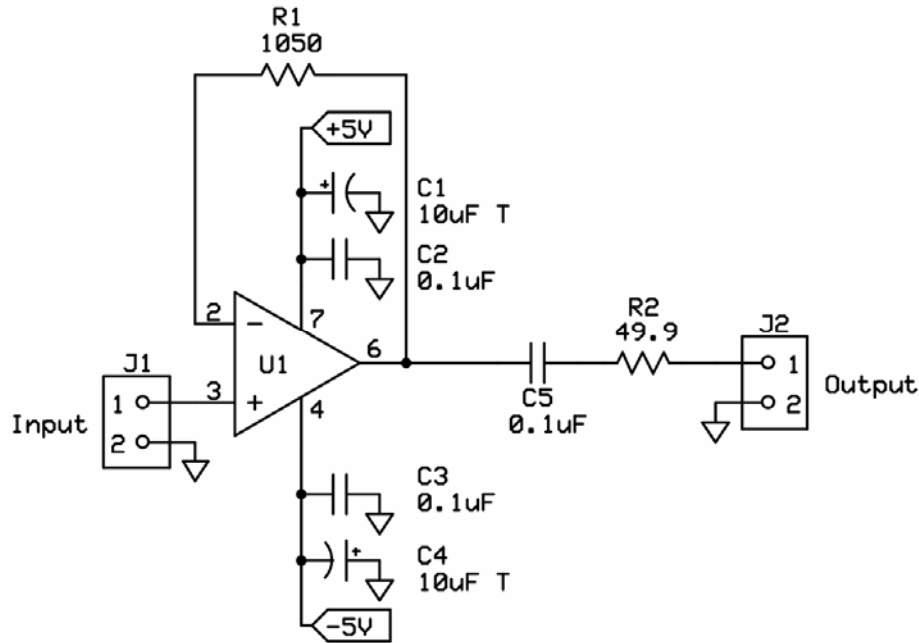


Figure 3: Voltage follower using a current feedback operational amplifier

Figure 4 shows a voltage follower that uses a cascode JFET amplifier. The JFET Q1 is a common source amplifier that presents a large input impedance to the tank circuit. The upper JFET Q2 presents a low input impedance to Q1 and provides a wide bandwidth gain. The overall gain of the circuit is set by R1 and is approximately 10 dB.

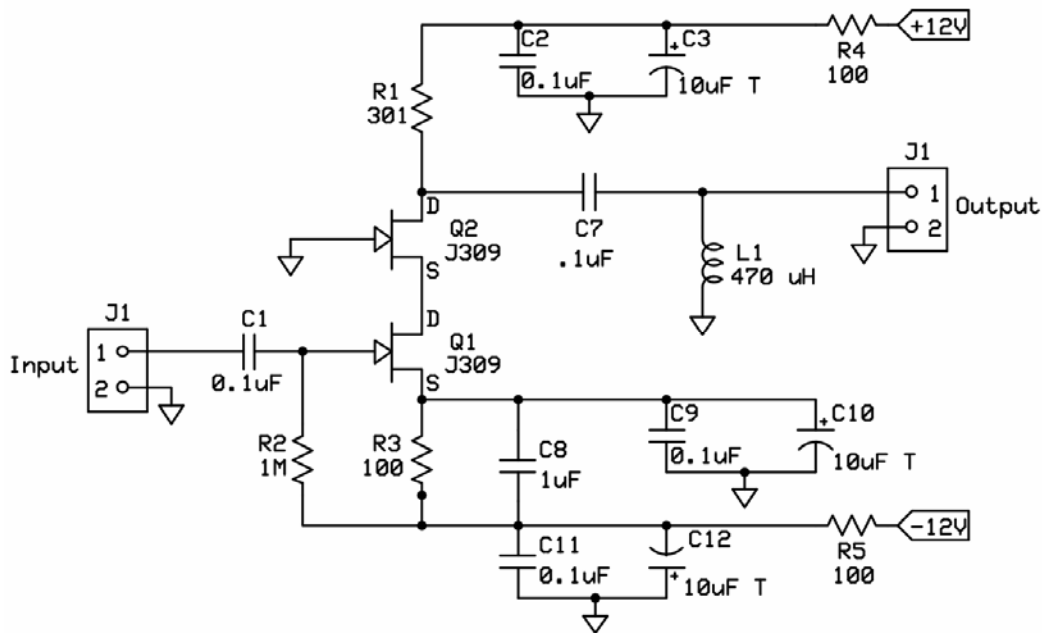


Figure 4: Voltage follower using a cascode JFET amplifier

The three voltage follower circuits are assessed by studying their effect on the center frequency and Q-factor of a tuned tank circuit. Figure 5 shows a block diagram of the measurement setup, while Figure 6 shows a photograph of the actual system. Placing a silver mica capacitor with capacitance C in parallel with a QR probe with self-inductance L and self-resistance R forms a tank circuit with center frequency ω^* . The center frequency ω^* and the maximum Q-factor of the tank circuit are calculated using equations (1) and (3). The component values L , R , and C are measured using a vector network analyzer (NA).

The tank circuit is then connected to the voltage follower under test. In Figure 6, the QR probe is the gray colored coil located at one end of the printed circuit board that contains the voltage follower circuit as well as the tuning capacitor C . The tank circuit is excited by weakly coupling the output from port 1 of the NA to the QR probe coil using a two turn loop as shown in Figure 6, while the output of the voltage follower is connected to port 2 of the NA. The network analyzer displays the magnitude of the S_{21} scattering parameter which represents the frequency response of the tuned probe and voltage follower. The NA calculates the Q-factor and center frequency of the entire system. By comparing these values against those of just the tank circuit calculated using equations (1) and (3), the NA measurement reveals the effect of the voltage follower on the Q-factor and center frequency of the tuned tank circuit.

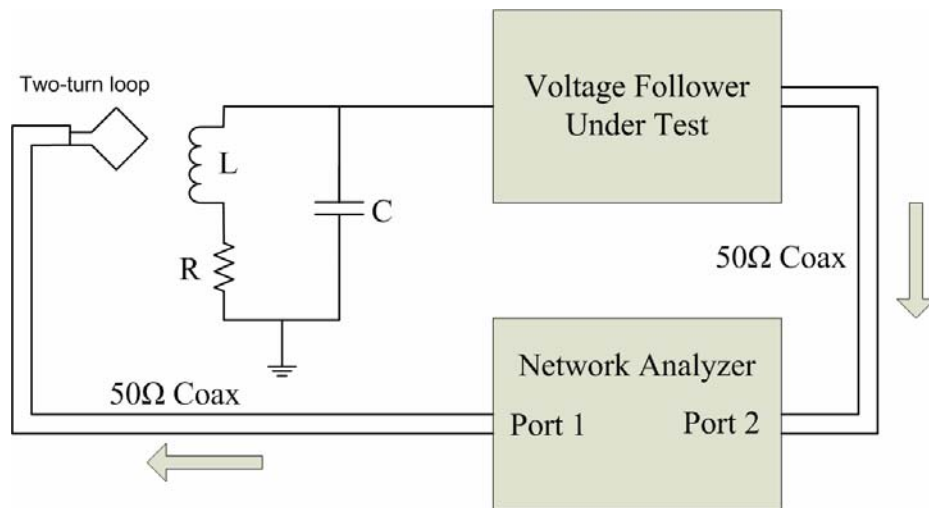


Figure 5: Block diagram of the system for testing the voltage follower circuits

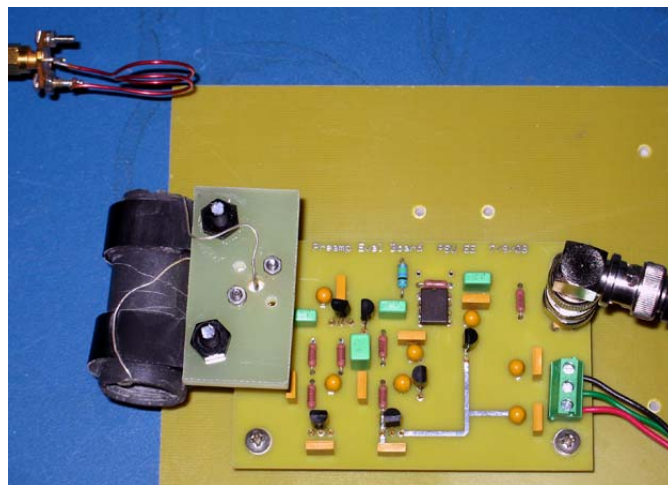


Figure 6: Photograph of the system for testing the voltage follower circuits

Envelope Detector Circuits

This paper considers two circuits for recovering the envelope of the RMO. Figure 7 shows an envelope detector that uses a precision diode to rectify the signal from the oscillator. The envelope signal is recovered by passing the output of the precision rectifier through a lowpass filter comprised of R_3 and C_3 . Figure 8

shows a square-law detector implemented with a single JFET. This circuit exploits the fact that the drain current is proportional to the square of the gate-source voltage.

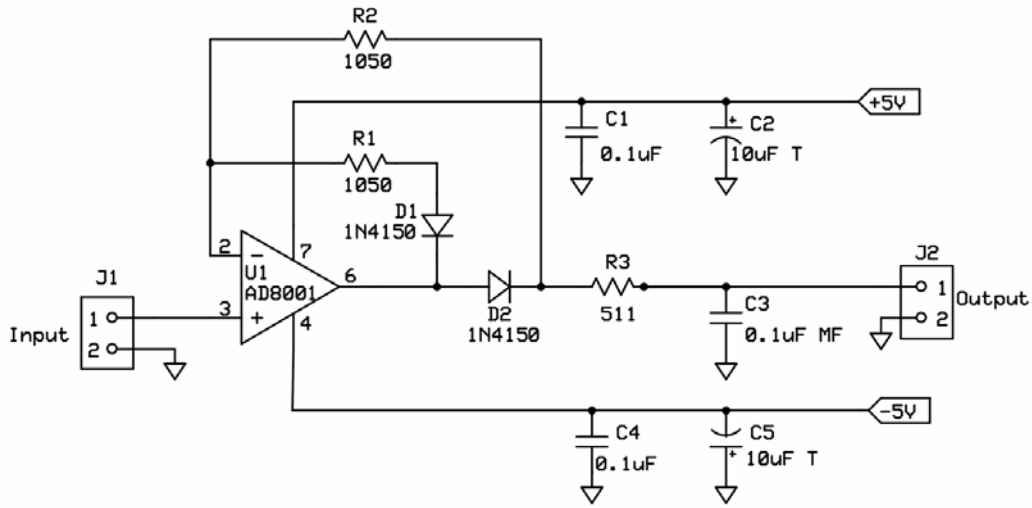


Figure 7: Envelope detection using a precision rectifier

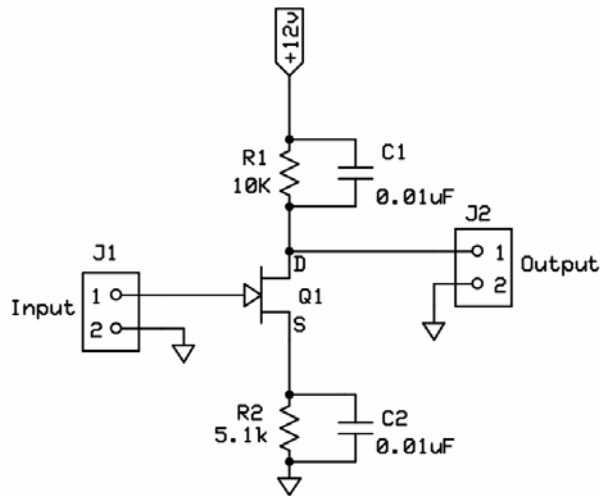


Figure 8: Envelope detection using a JFET

The envelope detectors are evaluated by observing their response to a known AM waveform. A signal generator produces a 5 MHz carrier that is modulated by a

RESULTS

Voltage Follower Circuits

The self-inductance L and self-resistance R of the probe coil were measured to be $8 \mu\text{H}$ and $800 \text{ m}\Omega$, respectively, at 3.25 MHz . The tuning capacitance is approximately 294 pF . The corresponding resonant frequency and Q-factor calculated using equations (1) and (3) are 3.367 MHz and 212 , respectively.

Using the NA and the test set up in Figure 5, the Q-factor and center frequency of the system consisting of the tank circuit and voltage follower were measured and are reported in Table II. Figure 10 shows the magnitude of the S_{21} scattering parameter. The solid, dashed, and dotted curves show the S_{21} magnitude for the voltage follower circuits using the AD811, AD8001, and JFET design, respectively. The origin of the frequency axis corresponds to the 3.308 MHz transition frequency of hexamethylenetetramine, while the magnitude of the S_{21} parameter is specified in decibels.

Table II. Effect of the voltage follower circuits on the Q-factor and center frequency of the tank circuit

Circuit	Q-Factor	Center Frequency [MHz]	3dB bandwidth [kHz]
AD811	145	3.2347	22.20
AD8001	156	3.2859	21.06
JFET	147	3.2493	22.07

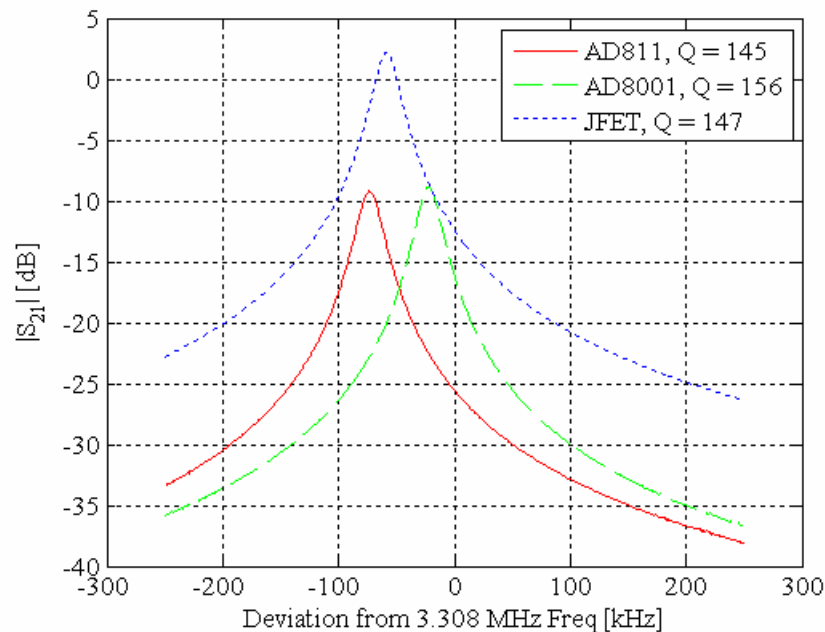


Figure 10: S_{21} measurements for the three voltage follower circuits

Envelope Detector Circuits

Figure 13 shows the input AM waveform and the response of each of the envelope detector circuits. The upper trace shows AM waveform applied to the envelop detector circuits. The middle waveform is the output of the JFET square-law detector, while the bottom trace is the output of the precision rectifier circuit.

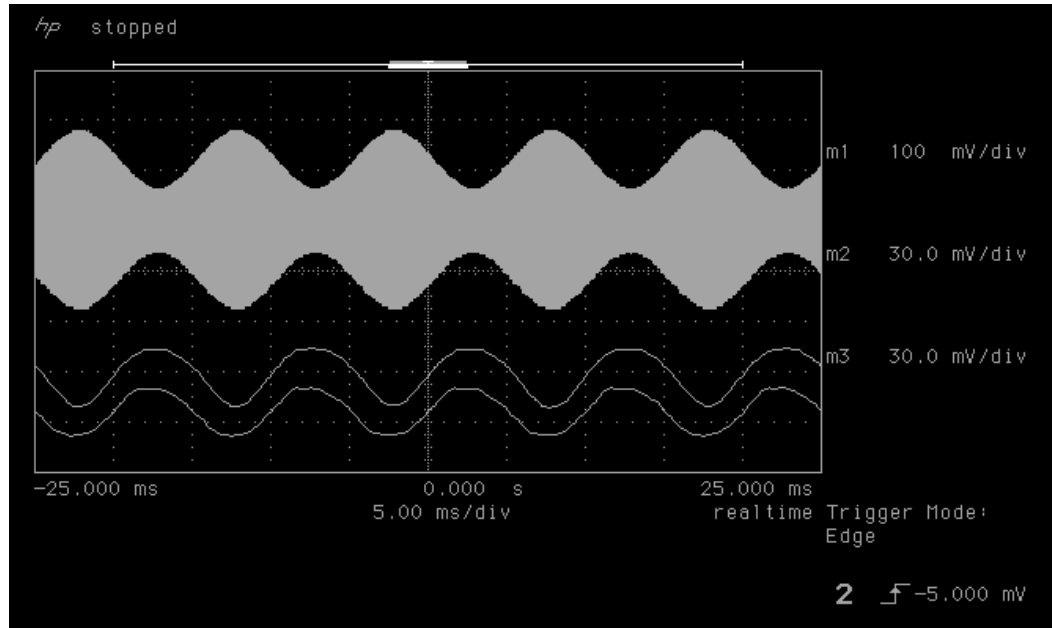


Figure 11: Envelope detection using a precision diode (middle trace) and JFET (lower trace)

The Limiter Circuit

Figure 12 shows the input-output characteristics for the limiter using the parameter set $(g_a, g_b/g_a, v_t) = (1, 0.9, 0.5)$. The horizontal axis shows the peak amplitude of the 5 MHz input sinusoid, while the vertical axis shows the peak value of the limiter output voltage. The solid curve shows the desired transfer characteristic. As the ratio g_b/g_a is close to one, a dashed curve showing the transfer function for a pure gain g_a is also included to show the effect of the limiter for input voltages greater than the desired 500 mV threshold voltage. The open circles show the experimentally measured output voltage. Figure 13 shows the results for the parameter set $(g_a, g_b/g_a, v_t) = (2, 0.9, 0.1)$ using the same presentation format.

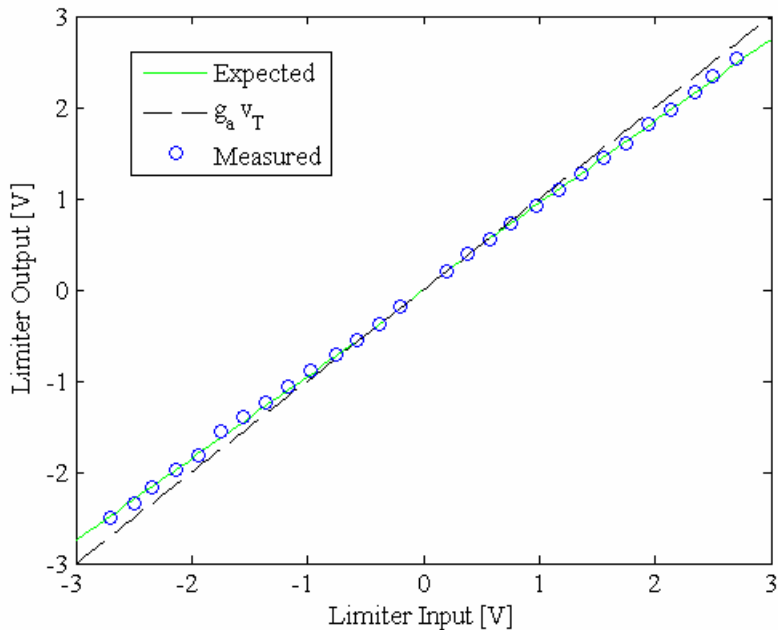


Figure 12: Limiter characteristics using the parameters $(g_a, g_b/g_a, v_t) = (1, 0.9, 0.5)$

DISCUSSION

Data from the voltage follower measurements indicate that the AD8001 circuit has the smallest effect on the Q-factor and resonant frequency of the tank circuit. As a reference point, the maximum Q-factor of the tank circuit, predicted from equation (3) and measurements of the component values, is 212. When the tank circuit is connected to the AD8001 voltage follower circuit the Q-factor is reduced to 156. The voltage followers using the AD811 current-feedback operational amplifier and the JFET cascode amplifier have slightly smaller Q-factors of 145 and 147, respectively. The latter designs also produced a larger reduction in resonant frequency of the tuned circuit in comparison to the AD8001. The effect is mostly likely due to a larger input capacitance for the AD811 and JFET cascode designs. The only potential advantage of the cascode design is that it can handle higher input voltages than either operational amplifier design. The maximum output voltage of both the AD811 and AD8001 before clipping occurs is approximately 2.7V. These observations, and the fact that the AD8001 circuit requires substantially less components than the JFET cascode design, motivate the selection of the AD8001 in the voltage follower circuit.

Figure 11 shows that both envelop detector circuits produce an output voltage that tracks the envelope of the AM input waveform. The asymmetry in the shape of the peaks and troughs of the output of the JFET detector reveals that this circuit recovers the square of the envelope voltage. In comparison, there is less distortion in the envelope recovered by the precision rectifier. Further improvement in the

fidelity of the recovered envelop may be achieved by replacing the diodes with high speed Schottky diodes.

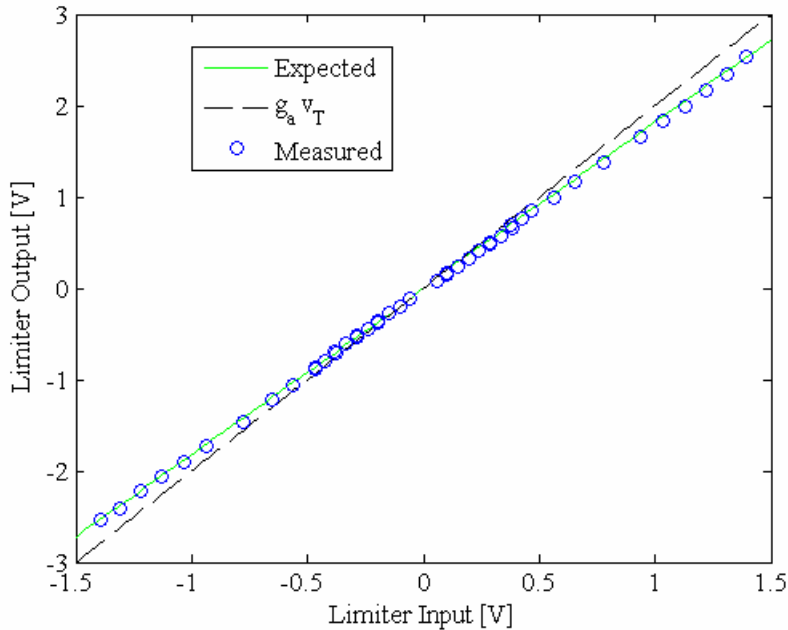


Figure 13: Limiter characteristics using the parameters $(g_a, g_b/g_a, v_t) = (2, 0.9, 0.1)$

The measured limiter transfer characteristics in Figures 12 and 13 show that the limiter circuit in Figure 9 provides a good approximation of the desired two-slope soft limiter characteristic in Figure 2(B). Using an oscilloscope to measure the phase difference between the limiter input and output voltages reveals a phase shift that is smaller than one degree at 5 MHz. This is a desirable attribute as a phase shift larger than several degrees will distort the shape of the QR transition.^[11]

CONCLUSION

The goal of this study was to evaluate candidate circuits for realizing the voltage follower, envelop detector, and limiter circuit blocks for a RMO. Based on experimental measurements, it was determined that the AD8001 current-feedback operational amplifier provides an adequate voltage follower, while the precision rectifier recovers the oscillator envelop with great fidelity. A circuit for implementing a two-slope limiter was also implemented and verified.

ACKNOWLEDGEMENTS

One of the authors (MM) would like to thank Dr. Jeffrey Schiano for his extensive knowledge and help on this project. MM would also like to thank Penn State for the opportunity to be a part of the EE REU program. This material is

based upon work supported by the National Science Foundation under Grant No. EEC-0755081.

REFERENCES

- ¹ A.N. Garroway, M.L. Buess, J.B. Miller, B.H. Suits, A.D. Hibbs, G.A. Barrall, R. Matthews, and L.J. Burnett, "Remote Sensing by Nuclear Quadrupole Resonance," *IEEE Transactions on Geoscience and Remote Sensing*, **39** (6) 1108-1118 (2001).
- ² A.S. Azheganov, V.P. Begishev, D.A. Gorinov, S.N. Lysenko, I.N. Shardakov, and N.K. Shestakova, "A Nuclear Quadrupole Resonance Study of the Elastic and Thermal Properties of Solid Composite Materials," *Polymer Science, Series B*, **46** (9-10) 288-296 (2004).
- ³ J.N. Latosińska, "Nuclear Quadrupole Resonance Spectroscopy in Studies of Biologically Active Molecular Systems- A Review," *Journal of Pharmaceutical and Biomedical Analysis*, **38** (4) 577-587 (2005).
- ⁴ J.A. Smith, "Nuclear Quadrupole Resonance Spectroscopy," *Journal of Chemical Education*, **48** (1) 39-49 (1971).
- ⁵ T.P. Das and E.L. Hahn, "Nuclear Quadrupole Resonance Spectroscopy"; pp. 83-93, Academic Press, New York, 1958.
- ⁶ F.N.H. Robinson, "Nuclear Resonance Absorption Circuit," *Journal of Scientific Instruments*, **36** (12) 481-487 (1959).
- ⁷ T.L. Viswanathan, T.R. Viswanathan, Sane K.V, "Study of Marginal Oscillator Behavior," *IEEE Transactions on Instrumentation and Measurement*, **IM24** (1) 55-61 (1975).
- ⁸ G.D. Watkins and R.V. Pound, "The Pure Nuclear Electric Quadrupole Resonance of N¹⁴ in Three Molecular Solids," **85** (6) 1062-1062 (1952)
- ⁹ H.L. Krauss, C.W. Bostian, and F.H. Raab, "*Solid State Engineering*"; pp. 38-71, John Wiley & Sons, New York, 1980.
- ¹⁰ K.K. Clarke and D.T. Hess, "*Communication Circuits: Analysis and Design*"; pp. 457-503, 3rd ed., Krieger Publishing Company, Florida, 2002.
- ¹¹ D.G. Hughes and M.R. Smith, "On the Nuclear Magnetic Resonance Detection Characteristics of Marginal and Robinson Oscillators," *Journal of Physics E: Scientific Instruments*, **4** (1) 13-20 (1971).

FINITE ELEMENT METHOD SIMULATION OF VOLTAGE DRIVEN SOLID ROTOR SYNCHRONOUS MACHINES WITH LC FILTERS

Michael W. Lengel* and Heath Hofmann#

Department of Electrical Engineering
The Pennsylvania State University, University Park, PA 16802

*Undergraduate student of
Department of Electrical Engineering
Bucknell University
Lewisburg, PA 17837

ABSTRACT

It is rare for three-phase voltage-driven synchronous machines to be driven by pure sinusoidal inputs in variable-speed drive applications. Instead, it is common to use pulse-width modulated (PWM) voltages generated by an inverter. Unfortunately, PWM voltages introduce many high frequency harmonics to the system, which increase the heat loss in the rotor of solid-rotor machine designs. To mitigate the effects of these harmonics, the inverter voltage can be passed through a low-pass LC filter before entering the machine. This paper analyzes the effectiveness of the LC filter in reducing heat loss within the machine under steady-state conditions. The machine is modeled in MATLAB using the finite element method.

INTRODUCTION

As demand for power continues to increase, engineers are faced with increasing demands of efficiency from electromagnetic machines. This requires increasing accuracy in the simulation methods associated with these machines. One method which has proven an effective tool for simulating electric machines involves the finite element method. This allows for a two dimensional cross-section of a machine to be eventually broken down into a system of differential algebraic equations which can be easily solved by programs such as MATLAB.

Faculty Mentor

An algorithm for MATLAB simulating one mechanical period of a three-phase, 4 pole solid rotor synchronous machine with 36 stator teeth and 3 rotor segments has already been developed using the shooting-Newton/GMRES ODE method.^[1] Since it is difficult to generate a pure sinusoidal voltage efficiently with power electronic circuitry, all input voltages have a certain amount of higher harmonics in them which can cause unintended heat loss inside of rotors. To combat the loss from these higher harmonics, a low-pass filter can be placed between the source of the signal and the machine.

The purpose of this study is to determine the effectiveness of an ungrounded-ye configured LC filter in significantly reducing the heat loss inside of a solid rotor through a MATLAB simulation. The goal was to have a comparison between filtered and non-filtered PWM voltages as inputs, but time constraints prevented the full implementation of the PWM code.

SIMULATION DESCRIPTION

This simulation was modified from a simulation performed as a master's thesis by a former student of the mentor of this paper.^[1] Most of the procedure remains the same; however, the MATLAB code and the simulation were modified to incorporate an ungrounded wye configured LC filter.^[2] In order for the system of equations to be independent, the three-phase machine was converted to its equivalent two-phase form by the Clarke transform.^[2]

The independent two-phase form of the LC filter is configured as shown in Figure 1.

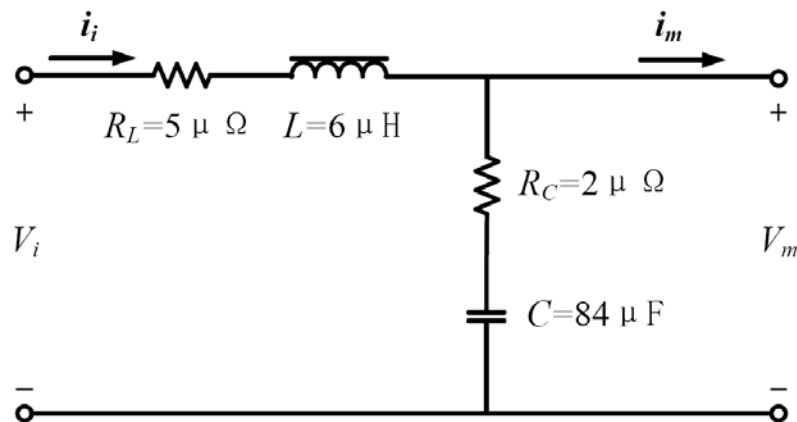


Figure 1: Schematic of the independent LC filter with values used in the simulation.

The simulation integrates the following system of differential algebraic equations:

$$S \frac{d}{dt} \vec{x} + K\vec{x} = \vec{u}(x, t) \quad (1)$$

where S, K, \mathbf{x} , and $\mathbf{u}(\mathbf{x}, \mathbf{t})$ were adjusted from the previous simulation to incorporate the LC filter. Please see [1] for the original equations. The new equations are incorporated below.

$$S_a \frac{d}{dt} \vec{a} + K_a \vec{a} - T_n \vec{l}_m = \vec{I}_m(\vec{a}) \quad (2)$$

$$S_\varphi^T \frac{d}{dt} \vec{a} + G \vec{\nabla} \varphi + T_c \vec{l}_m = 0 \quad (3)$$

Eqns. (2) and (3) are exactly as they appeared in [1]. The third equation appeared as follows in [1].

$$L_{leak} \frac{d}{dt} \vec{l}_m + T_v \vec{\nabla} \varphi + R_{leak} \vec{l}_m = \vec{v}_m \quad (4)$$

However, the motor voltage \mathbf{v}_m is affected by the LC filter and can no longer be considered an input into the system. Instead, by Kirchoff's voltage law, it can be shown that

$$\vec{v}_m = \vec{v}_c + R_c \vec{l}_i - R_c \vec{l}_m \quad (5)$$

By combining eqns. (4) and (5), the third equation of the system is

$$L_{leak} \frac{d}{dt} \vec{l}_m + T_v \vec{\nabla} \varphi + (R_{leak} + R_c) \vec{l}_m - R_c \vec{l}_i - \vec{v}_c = 0 \quad (6)$$

By applying Kirchoff's voltage law to the other side of the LC filter, the fourth equation of the system presents itself.

$$L_{filter} \frac{d}{dt} \vec{l}_i - R_c \vec{l}_m + (R_L + R_c) \vec{l}_i + \vec{v}_c = \vec{v}_i \quad (7)$$

The final equation for the system comes from applying Kirchoff's current law to the filter.

$$C_{filter} \frac{d}{dt} \vec{v}_c + \vec{l}_m - \vec{l}_i = 0 \quad (8)$$

These new equations form a system of the form of eqn. (1); however, the values of all of the vectors and coefficients now reflect the LC filter system as well.

$$\vec{x} = \begin{bmatrix} \vec{a} \\ \vec{\nabla} \varphi \\ \vec{l}_m \\ \vec{l}_i \\ \vec{v}_c \end{bmatrix}$$

$$\vec{u}(t) = \begin{bmatrix} \vec{I}_m(\vec{a}) \\ 0 \\ 0 \\ \vec{v}_i \\ 0 \end{bmatrix}$$

$$S = \begin{bmatrix} S_a & 0 & 0 & 0 & 0 \\ S_\phi^T & 0 & 0 & 0 & 0 \\ 0 & 0 & L_{leak}I_2 & 0 & 0 \\ 0 & 0 & 0 & L_{filter}I_2 & 0 \\ 0 & 0 & 0 & 0 & C_{filter}I_2 \end{bmatrix}$$

$$K = \begin{bmatrix} K_a & 0 & -T_n & 0 & 0 \\ 0 & G & T_c & 0 & 0 \\ 0 & T_v & (R_{leak} + R_c)I_2 & -R_cI_2 & -I_2 \\ 0 & 0 & -R_cI_2 & (R_L + R_c)I_2 & I_2 \\ 0 & 0 & I_2 & -I_2 & 0 \end{bmatrix}$$

As a basis for comparison, the simulation was run with an ideal, sinusoidal input voltage on the system without the filter. Then the simulation was run again with the filter in place.

RESULTS

A preliminary look at the heat loss for both systems shows that a system without a filter loses 14.82 kW as heat each mechanical period while a system with an LC filter loses only 12.91 kW each mechanical period. The total reduction in rotor losses is 12.92% due to the LC filter.

By breaking the heat loss into its harmonics for both systems, a trend in significant harmonics emerges in Figure 2.

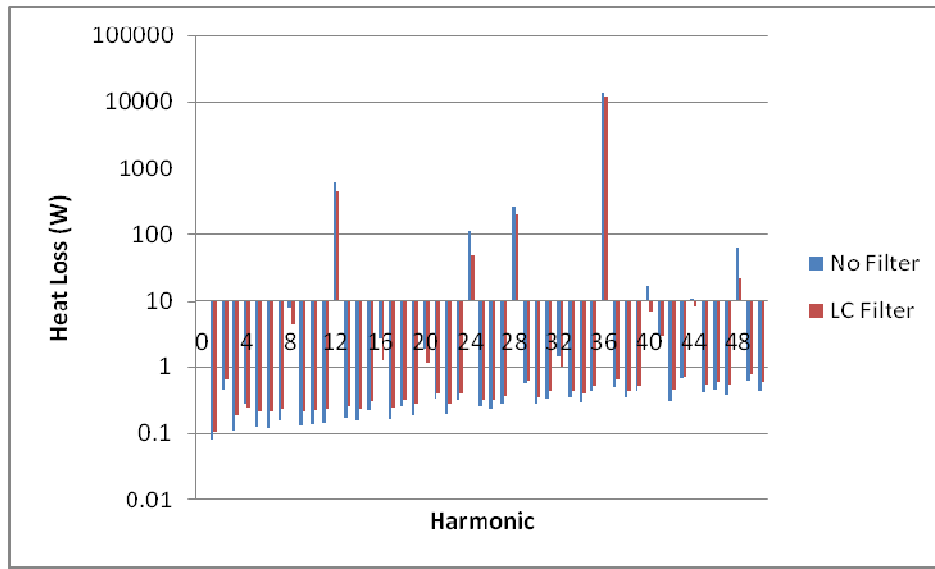


Figure 2: Heat loss by harmonic on logarithmic scale.

Note that using a logarithmic scale allows all harmonics to be observed. It also creates a convenient threshold for significance of the heat loss of a given harmonic. In this case, only harmonics generating more than 10 W of heat loss are considered significant to the overall system. A quick glance shows that the only harmonics which have significant heat losses are all multiples of 4.

A comparison of the marginal differences in heat loss for each significant harmonic is now in order. Figure 3 contains the marginal differences of all multiples of 4 with significant harmonics highlighted.

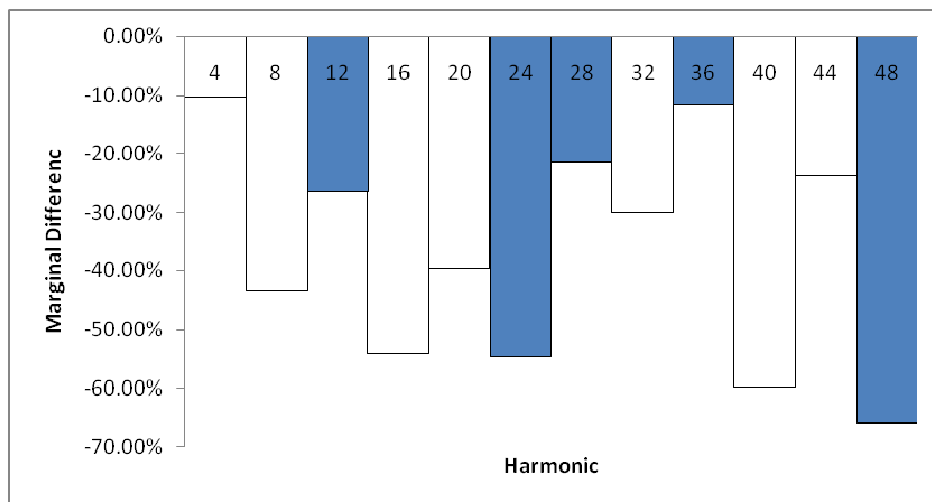


Figure 3: Marginal differences in heat loss by harmonic. Significant harmonics are highlighted.

By observing the actual differences in heat loss between the filtered and non-filtered systems, the significance of the highlighted harmonics is reinforced as shown in Figure 4.

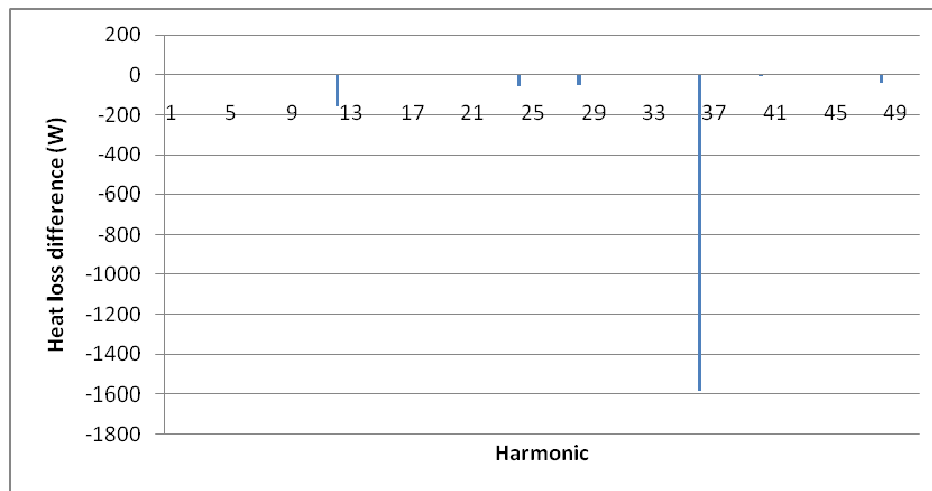


Figure 4: Measured differences in heat loss by harmonic.

The change in heat loss in the 36th harmonic overwhelms all other considerations in this case. Even if all of the other harmonics increased their heat loss, it is likely the heat loss change from the 36th harmonic would still dominate and lead to a net reduction of heat loss.

DISCUSSION

One of the most obvious trends in this simulation is the fact that only harmonics which were multiples of 4 had significant heat losses. This is likely due to the physical nature of the machine simulated. Theory suggests that the 4 pole nature of the solid rotor is responsible for the significant heat losses on harmonics divisible by 4.^[3] The reason the 36th harmonic is so dominant is likely due to the 36 stator teeth. Past observations suggest the teeth generate massive heat loss in the harmonic equal to their number.^[3] If the simulation were changed to incorporate a different number of stator teeth, say 37, it is likely the dominant harmonic would then be the 37th harmonic to correspond with the number of stator teeth.

One uncertainty in this simulation is the optimization of the LC filter. The values of the capacitor, inductor, and their related resistances were somewhat arbitrary and were not optimized for this application. The values used were typical values, but not optimal values. Different steady state responses could result from an optimized LC filter.

One of the most common realistic driving signals found in industry is a pulse-width modulated signal generated by an inverter. If the simulation were to be run with a PWM signal, further analysis to the effectiveness of the LC filter could be completed.

CONCLUSION

This simulation supports the effectiveness of the LC filter reducing the heat loss inside the rotor resulting from the higher harmonics of a signal. For the specific machine and filter simulated, the heat loss was significantly reduced by 12.92% compared to a non-filtered machine of the same specification. Since the design had 36 stator teeth, the dominant harmonic for heat loss was the 36th harmonic. Much more can be done to improve this simulation technique, but it provides a starting point for a tool to help optimize synchronous drive designs.

ACKNOWLEDGEMENT

This material is a direct continuation of the work presented in the Master Thesis of Pasha S. Petite from The Pennsylvania State University. This material is based upon work supported by the National Science Foundation under Grant No. EEC-0755081.

REFERENCES

1. P.S. Petite, "Numerically Efficient Finite Element Method Simulation of Voltage Driven Solid Rotor Synchronous Machines," The Pennsylvania State University Master Thesis in Electrical Engineering, 2008.
2. H. Hofmann, Lecture notes and unpublished book, June 2008.
3. H. Hofmann, "High-Speed Synchronous Reluctance Machine for Flywheel Applications," The University of California at Berkley Doctor of Philosophy Thesis in Electrical-Engineering and Computer Sciences, 1998.

